GeoForschungsZentrum Potsdam GFZ

Sektion 2.6 „Erdbebengefährdung und Spannungsfeld“

The 3D In-Situ Stress Field and Its Changes in Geothermal Reservoirs

kumulative Dissertation

zur Erlangung des akademischen Grades

„doctor rerum naturalium“ (Dr. rer. nat.)

in der Wissenschaftsdisziplin Geowissenschaften

eingereicht an der

Mathematisch-Naturwissenschaftlichen Fakultät

der Universität Potsdam

vorgelegt von

M.Sc. Moritz Ziegler

Potsdam, den 11. Mai 2017

Gutachter: apl. Prof. Dr. Arno Zang

Prof. Dr. Andreas Henk

Prof. Dr. Benoît Valley

Published online at the
Institutional Repository of the University of Potsdam:
URN urn:nbn:de:kobv:517-opus4-403838
http://nbn-resolving.de/urn:nbn:de:kobv:517-opus4-403838

for Karoline & Leander

„Marmor, Stein und Eisen bricht…“

German pop song about the stability
of rocks and other things.

Abstract

Information on the contemporary in-situ stress state of the earth's crust is essential for geotechnical applications and physics-based seismic hazard assessment. Yet, stress data records for a data point are incomplete and their availability is usually not dense enough to allow conclusive statements. This demands a thorough examination of the in-situ stress field which is achieved by 3D geomechanical-numerical models. However, the models spatial resolution is limited and the resulting local stress state is subject to large uncertainties that confine the significance of the findings. In addition, temporal variations of the in-situ stress field are naturally or anthropogenically induced. In my thesis I address these challenges in three manuscripts that investigate (1) the current crustal stress field orientation, (2) the 3D geomechanical-numerical modelling of the in-situ stress state, and (3) the phenomenon of injection induced temporal stress tensor rotations. In the first manuscript I present the first comprehensive stress data compilation of Iceland with 495 data records. Therefore, I analysed image logs from 57 boreholes in Iceland for indicators of the orientation of the maximum horizontal stress component. The study is the first stress survey from different kinds of stress indicators in a geologically very young and tectonically active area of an onshore spreading ridge. It reveals a distinct stress field with a depth independent stress orientation even very close to the spreading centre. In the second manuscript I present a calibrated 3D geomechanical-numerical modelling approach of the in-situ stress state of the Bavarian Molasse Basin that investigates the regional ($70 \times 70 \times 10\,\mathrm{km}^3$) and local ($10 \times 10 \times 10\,\mathrm{km}^3$) stress state. To link these two models I develop a multi-stage modelling approach that provides a reliable and efficient method to derive from the larger scale model initial and boundary conditions for the smaller scale model. Furthermore, I quantify the uncertainties in the models results which are inherent to geomechanical-numerical modelling in general and the multi-stage approach in particular. I show that the significance of the models results is mainly reduced due to the uncertainties in the material properties and the low number of available stress magnitude data records for calibration. In the third manuscript I investigate the phenomenon of injection induced temporal stress tensor rotation and its controlling factors. I conduct a sensitivity study with a 3D generic thermo-hydro-mechanical model. I show that the key control factors for the stress tensor rotation are the permeability as the decisive factor, the injection rate, and the initial differential stress. In particular for enhanced geothermal systems with a low permeability large rotations of the stress tensor are indicated. According to these findings the estimation of the initial differential stress in a reservoir is possible provided the permeability is known and the angle of stress rotation is observed. I propose that the stress tensor rotations can be a key factor in terms of the potential for induced seismicity on pre-existing faults due to the reorientation of the stress field that changes the optimal orientation of faults.

Zusammenfassung

Kenntnis des derzeitigen in-situ Spannungszustandes der Erdkruste ist essenziell für geotechnische Anwendungen und seismische Gefährdungsabschätzungen, welche auf physikalischen Beobachtungen basieren. Jedoch sind die Spannungsinformationen jedes Datenpunktes unvollständig und die Menge an vorhandenen Datenpunkten ist normalerweise nicht groß genug, um schlüssige Ergebnisse zu erzielen. Daher ist eine eingehende Untersuchung des in-situ Spannungsfeldes, welche durch 3D geomechanisch-numerische Modellierung geleistet wird, erforderlich. Jedoch ist die räumliche Auflösung der Modelle begrenzt und der resultierende Spannungszustand ist großen Unsicherheiten unterworfen, welche die Aussagekraft der Ergebnisse beschränken. Zusätzlich gibt es zeitliche Änderungen des Spannungsfeldes, welche durch natürliche Prozesse bedingt oder menschengemacht sind. In meiner Dissertation behandle ich diese Herausforderungen in drei Manuskripten, welche (1) die Orientierung des derzeitigen Spannungszustandes, (2) die 3D geomechanisch-numerische Modellierung des in-situ Spannungszustandes und (3) das Phänomen injektionsinduzierter zeitlicher Rotationen des Spannungstensors zum Thema haben. In dem ersten Manuskript präsentiere ich die erste umfassende Spannungsdatensammlung von Island mit insgesamt 495 Einträgen. Dafür habe ich Bilddatenlogs aus 57 Bohrlöchern in Island auf Indikatoren der maximalen horizontalen Spannungsorientierung hin untersucht. Diese Studie ist die erste ganzheitliche Spannungsuntersuchung, welche sich auf verschiedene Indikatoren der Spannungsorientierung stützt und in einem geologisch sehr jungen und tektonisch aktiven Gebiet auf einem Mittelozeanischen Rücken an Land liegt. Es zeigt sich, dass selbst sehr nahe an der Plattengrenze eine tiefenunabhängige, eindeutige Spannungsorientierung existiert. In dem zweiten Manuskript präsentiere ich einen kalibrierten 3D geomechanisch-numerischen Modellierungsansatz des in-situ Spannungszustandes des bayrischen Molassebeckens welches den regionalen ($70 \times 70 \times 10\,\mathrm{km}^3$) und den lokalen ($10 \times 10 \times 10\,\mathrm{km}^3$) Spannungszustand untersucht. Um diese zwei Modelle zu verbinden, habe ich ein mehrstufigen Modellansatz entworfen, welcher eine zuverlässige und effiziente Methode darstellt um Randbedingungen und Initialbedingungen für das kleinere Modell aus dem größeren Modell abzuleiten. Des Weiteren quantifiziere ich die Unsicherheiten in den Modellergebnissen, welche im Allgemeinen durch geomechanisch-numerische Modellierung und im Speziellen durch den Mehrstufenansatz entstehen. Ich zeige, dass die Signifikanz der Modellergebnisse hauptsächlich durch die Unsicherheiten in den Materialeigenschaften sowie der geringen Anzahl vorhandener Spannungsmagnitudendaten zur Kalibrierung reduziert wird. In dem dritten Manuskript untersuche ich das Phänomen injektionsinduzierter zeitlicher Rotationen des Spannungstensors und deren kontrollierende Parameter. Ich führe eine Sensitivitätsanalyse mit einem generischen 3D thermo-hydro-mechanischen Modell durch. Darin zeige ich, dass die Schlüsselparameter, welche die Rotationen des Spannungstensors kontrollieren, die Permeabilität des Reservoirgesteins als der entscheidende Faktor, die Injektionsrate und die initiale Differenzspannung sind. Insbesondere für geothermische Systeme nach dem Hot-Dry-Rock-Verfahren mit einer geringen Permeabilität weisen die Ergebnisse auf große Rotationen des Spannungstensors hin. Gemäß diesen Ergebnissen kann die initiale Differenzspannung in einem Reservoir abgeschätzt werden, sollte die Permeabilität bekannt sein und der Winkel der Spannungsrotation beobachtet werden. Ich schlage vor, dass Spannungsrotationen ein Schlüsselfaktor in Bezug auf das Potenzial für induzierte Seismizität sind, welche auf prä-existierenden Störungen entsteht, die durch die Reorientierung des Spannungsfeldes optimal orientiert werden.

Notation (List of Symbols)

σ_{ij}	Stress tensor, $i, j = 1, 2, 3$
$\mathrm{S_{Hmax}}$	Maximum horizontal stress
$\mathrm{S_{hmin}}$	Minimum horizontal stress
$\mathrm{S_v}$	Vertical stress
$S1 = \sigma_1$	Largest principal stress
$S2 = \sigma_2$	Intermediate principal stress
$S3 = \sigma_3$	Smallest principal stress
τ	Shear stress
σ_n	Normal stress

α_B	Biot-Willis coefficient
ζ	Boltzmann variable
x, y, z	Cartesian coordinates
C	Cohesion
c_{ijkl}	Elasticity tensor
ρ	Density
d	Diffusivity
μ_{dyn}	Dynamic viscosity
q	Fluid flow rate
Φ	Friction angle
μ	Friction coefficient
g	Gravitational acceleration
K	Hydraulic Conductivity
λ	Lamé's first parameter
G	Lamé's second parameter
k_f	Permeability
ν	Poisson ratio
P_p	Pore pressure
ϵ_{ij}	Strain tensor
α_T	Thermal expansion coefficient
E	Young's module

Contents

1 Introduction

Our society largely depends on the underground as a source for raw materials and energy, a host for short to long-term storage of energy carriers and waste, as well as for subsurface infrastructure installations. Many of these applications such as hydrocarbon exploitation, high level nuclear waste storage, or fluid waste disposal are highly sensitive since a failure has the potential to cause disastrous results. Hence, the stability of the rock is of substantial importance for safety and sustainability. In order to assess the stability knowledge of the in-situ stress state, as well as the properties and constitutive laws of the affected subsurface rock are required (Hoek and Brown, 1980; Fuchs and Müller, 2001; Zoback, 2010). The local stress state is a result of the stresses generated by plate boundary forces, regional features such as topography, local perturbations such as active faults and material contrasts, as well as remnant stresses (Zoback, 1992; Müller et al., 1997; Coblentz et al., 1998; Heidbach et al., 2007; Zoback, 2010). Furthermore, permanent and transient stress changes are induced by man-made processes (McGarr et al., 1975; Segall and Fitzgerald, 1998; Evans et al., 2012; Zang et al., 2014; Schoenball et al., 2014; Gaucher et al., 2015). The three key points of rock stability investigations in this thesis address the available stress data records, the criticality of the in-situ stress state, and transient stress changes (Fig. 1.1). That information is displayed in the Mohr-Coulomb diagram which allows assessing the mechanical criticality of the subsurface (Fig. 1.2). In the diagram it is indicated whether the rock material in the prevalent stress state is stable or fails (Zang and Stephansson, 2010). Figure 1.2 indicates the large dependence of the rock stability on the stress state. Both, the individual stress magnitudes and the differential stress between the maximum and minimum principal stress are decisive factors for the stability of the rock.

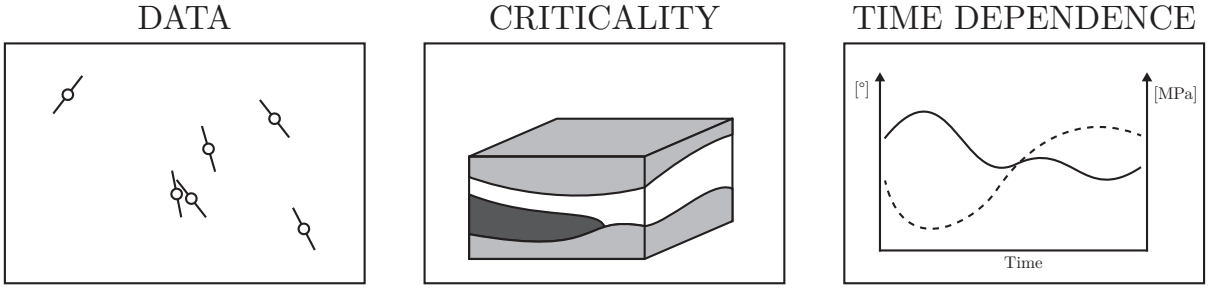

Figure 1.1: The three key parts of this thesis concern (from left to right) the compilation of point-wise data records, the estimation of fault criticality and rock stability in a volume by means of a 3D geomechanical-numerical model, and the characterisation and cause of transient changes in the stress state.

A safe and sustainable exploration and reservoir engineering takes into account the influence of the stress state on the rock stability in order to prevent structural failures such as borehole breakouts or cave-

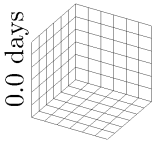

ins (Tingay et al., 2015; Rajabi et al., 2016a; Orlecka-Sikora, 2010; Zoback et al., 1985; Bell and Gough, 1979). Furthermore, the possibility of failure in the rock mass surrounding the reservoir manifested in induced seismicity needs to be considered (Majer et al., 2007; Schoenball et al., 2010; Grünthal, 2014; Zang et al., 2014; Ellsworth, 2013; Ogasawara et al., 2002). Most subsurface applications show a strong time dependency concerning their influence on the stress field, such as the continuous excavation work in mines which results in ongoing changes in the stress field (Orlecka-Sikora, 2010; Brady and Brown, 2004; Ziegler et al., 2015). Hydrocarbon (Santarelli et al., 1998) or geothermal (Jeanne et al., 2014) fluid production and (re)injection, disposal of waste water (Hornbach et al., 2015), carbon capture and storage (CCS) (Kempka et al., 2014), and gas storage (Teatini et al., 2011) imply continuous or oscillating changes in the pore pressure which have a significant effect on the stress field (Zang et al., 2013; Zimmermann et al., 2010; Yoon et al., 2015b). In the same contexts the (re)injection of comparably cold fluid into reservoirs can induce thermal stresses (Bruel, 2002; Segall and Fitzgerald, 1998; Stephens and Voight, 1982). Thermal stresses in the near field also occur in relation with nuclear waste disposal in underground repositories (Rutqvist et al., 2008; Hodgkinson and Bourke, 1980; Yoon et al., 2014b). In addition natural processes such as earthquakes alter the stress state (Ickrath et al., 2015; Hardebeck, 2012; Hardebeck et al., 1998; Bohnhoff et al., 2006; King et al., 1994; Hensch et al., 2015).

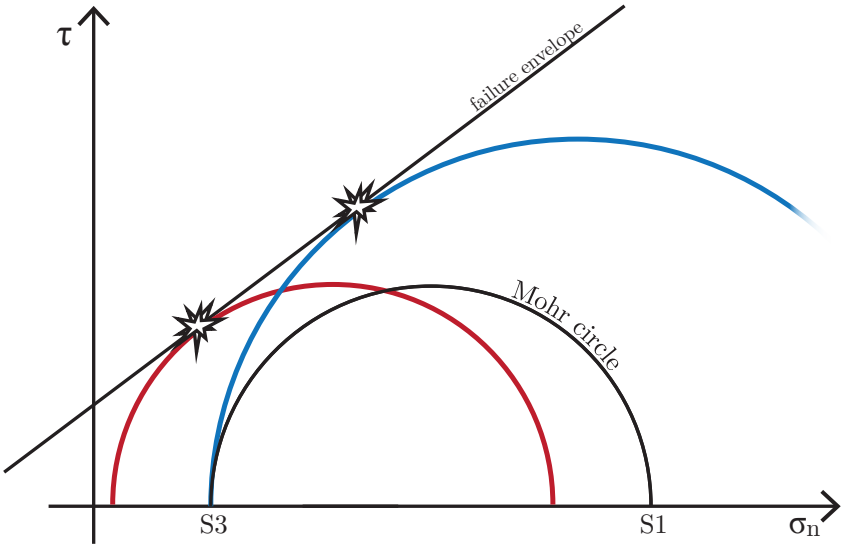

Figure 1.2: The Mohr-Coulomb diagram displays the stress state and a failure criterion for the rock mass (Zang and Stephansson, 2010). The normal stress σ_n is plotted on the x-axis and the shear stress τ on the y-axis. The Mohr circle connects the maximum and minimum effective principal stress $S1$ and $S3$. If the Mohr circle touches the envelope that is defined by the failure criterion the rock fails. A stable stress state (black Mohr circle) and two unstable stress states (red and blue) are shown in this example. The unstable stress states indicate that both the individual magnitudes of $S1$ and $S3$ (red, $S1 - S3$ has the same magnitude as the black circle) as well as the differential stress $S1 - S3$ (blue, the magnitude of $S3$ is equal to the black circle but the magnitude of $S1$ is larger) are decisive factors for the stability of the rock.

These changes in the in-situ stress state alter the stability of the rock, i.e. the potential for creation of new faults or reactivation of pre-existing faults (Majer et al., 2007; Moeck and Backers, 2011; Hornbach et al., 2015; Morris et al., 1996; Connolly and Cosgrove, 1999). Thus, stress changes due to engineered pore pressure changes (Van Wees et al., 2014), thermal stresses (Kwiatek et al., 2015), or the removing of rock mass (Kwiatek et al., 2010) potentially induce or trigger seismic events (Dahm et al., 2010, 2012;

Grünthal, 2014; Zang et al., 2017; Evans et al., 2012; McGarr, 2014). In order to mitigate the potential for failure and induced seismicity a profound knowledge of the engineering processes influence on the stress field and the response of the rock is needed. The magnitude of those stress changes is investigated by means of thermo-hydro-mechanical (THM) models and indicate relative changes in the rock stability (Cornet et al., 1997; Yoon et al., 2014a; Jeanne et al., 2014; McClure and Horne, 2014b; Chang and Segall, 2016). However, the in-situ stress magnitudes are required for an authoritative indication of the absolute stability of the rock (Morris et al., 1996; Connolly and Cosgrove, 1999; Zang et al., 2012). Therefore, an investigation of the initial in-situ stress state as well as its changes is necessary (Hergert et al., 2015; Morris et al., 1996; Häring et al., 2008). However, the available orientation and magnitude data on the stress tensor are sparse and incomplete (Heidbach et al., 2016a; Zang et al., 2012).

In this thesis the in-situ stress state and its anthropogenic changes as controlling factors for rock stability are investigated. The compilation of stress data records, the 3D geomechanical-numerical modelling of the in-situ stress state, and transient stress changes are addressed (Fig. 1.1). Information on the stress state is available and compiled by the World Stress Map (WSM) that indicates the orientation of the maximum horizontal stress S_{Hmax} (Heidbach et al., 2016a, 2010; Sperner et al., 2003; Zoback et al., 1989). However, the overall data density is small so that on reservoir scale ($10 \times 10 \times 10\,km^3$) usually no data is available at all and the information is too sparse in order to derive conclusive information (Reinecker et al., 2010; Tingay et al., 2010; Reiter et al., 2015; Rajabi et al., 2016c; Snee and Zoback, 2016). Yet, a conclusive regional stress pattern can be derived by an integrated compilation and analysis of regional stress data records (Müller et al., 1992; Reiter et al., 2014; Rajabi et al., 2016a). Such a stress pattern analysis provides a first order assessment of the criticality of faults with a known orientation. Information on the stress magnitudes are required (Morris et al., 1996; Zang et al., 2012; Reiter and Heidbach, 2014; Hergert et al., 2015) but the data availability for stress magnitudes is even more limited than that for the orientations (Zang et al., 2012; Heidbach et al., 2016a).

Even if more magnitude data is available from a database such as the Quantitative World Stress Map (Q-WSM) (Zang et al., 2012), 3D geomechanical-numerical modelling is essential in order to derive the in-situ stress state. The rare magnitude data records are used for calibration of 3D geomechanical-numerical models that estimate the stress state in a volume of interest (Reiter and Heidbach, 2014; Fischer and Henk, 2013; Hergert et al., 2015). However, usually the models are large in order to encompass the widely scattered data records required for calibration. The large size of such a model, however, limits the resolution due to the time required for computation. Thus, the resolution in the target area is not sufficiently fine for a detailed investigation of rock stability in a reservoir. In order to mitigate this trade-off the application of multi-stage modelling is proposed (Reiter, 2014; Fischer and Henk, 2013).

However, observations indicate that the in-situ stress state is not static but subject to transient changes induced by natural (Hensch et al., 2015; Hardebeck, 2012) and anthropogenic processes (Santarelli et al., 1998; Gaucher et al., 2015; Kozłowska et al., 2015). The changes of the in-situ stress state are a physical response of the rock to external processes such as large natural seismic events (King et al., 1994; Hardebeck, 2014) or reservoir engineering (Zang et al., 2014; McGarr, 2014; McClure and Horne, 2014b). Knowledge of the responsible process and a detailed observation of the transient stress changes hence allow to conclude on the physical properties of the rock. Martínez-Garzón et al. (2013) observed injection induced rotations of the principal stress axes in The Geysers geothermal reservoir, California. Due to the detailed knowledge of injection rate and the possibility for a detailed observation this stress rotation can be used to derive information on the reservoir.

In this thesis the estimation of regional stress orientation pattern is demonstrated in the tectonically highly active setting of Iceland. The compilation of stress data records from various indicators according

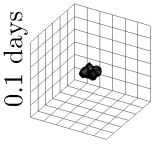

to the WSM quality ranking includes the analysis of 57 borehole image logs and a comprehensive literature study. This first integrated stress mapping at a spreading ridge reveals a distinct stress pattern with four provinces close to the plate boundary.

A 3D multi-stage approach presented in this work which uses differently sized models consolidates the benefits of a high resolution local model, a calibrated in-situ stress state, and a short computation time. The multi-stage approach is exemplified in the Bavarian Molasse Basin. A regional model ($70 \times 70 \times 10\,\mathrm{km}^3$) is calibrated on available stress data records and the simulated stress state is then used to calibrate a high resolution local model which provides a detailed stress field for a reservoir scale volume ($10 \times 10 \times 10\,\mathrm{km}^3$). An analysis of the modelled in-situ stress state provides information on the rock stability and fault criticality. Furthermore, the modelled stress state can be used as initial condition for process modelling.

The interaction of the stress field with fluid injection is investigated by means of a generic 3D THM reservoir model. The relationship between reservoir properties and treatment, the stress state, and the phenomenon of stress rotation is discussed and the sensitivity of different parameters that control the angle of stress rotation is indicated. An approach to estimate reservoir parameters such as the initial differential stress or the permeability from observed stress rotations is presented. This can be used for reservoir characterisation and helps to identify reservoir types which are prone to stress rotations. Since the criticality of pre-existing faults depends on the orientation of the fault in the stress field a rotation of the stress field alters the criticality of faults. Thereby, faults that were previously not optimally oriented for reactivation potentially increase their criticality.

In summary, the investigation and mapping of stresses, the modelling of the 3D in-situ stress field, and the simulation of injection induced transient stress rotations with a generic THM model are demonstrated in this thesis. The entire broad concept but also each single segment are applicable approaches in order to improve the safe and sustainable underground usage by the estimation of rock stability and fault criticality.

1.1 Structure of this Thesis

This thesis is *publication-based* and features the three key manuscripts which concern the estimation of the initial stress state in the earth's crust (Ziegler et al., 2016a,c) as well as anthropogenically induced changes (Ziegler et al., 2017). Each study focusses on a subtopic of geomechanics such as stress data derivation and compilation, 3D geomechanical in-situ stress modelling, and 3D THM reservoir modelling (Fig. 1.1). Furthermore, an account of the applied methods and scientific principles is given in Chapter 2. Eventually, each single manuscript is discussed individually and in synthesis with the other manuscripts (Chap. 6) and a final conclusion is drawn (Chap. 7).

Chapter 3 describes the pattern of S_{Hmax} orientation prevalent in Iceland. It involves the analysis of borehole image logs for stress indicators and the compilation of published stress data records according to the World Stress Map (WSM) quality criteria. The increase in data records from 38 in the WSM 2008 (Heidbach et al., 2008) to 495 in this work is also documented in a published stress map of Iceland (Ziegler et al., 2016b).

Chapter 4 presents the first application of a multi-stage approach of stress modelling in which the stress field in a local reservoir scale model is calibrated on a regional model. That regional model itself is calibrated on available stress data records. The associated uncertainties as well as optimisation strategies for the estimation of the initial in-situ stress state in a reservoir scale model are quantified.

In Chapter 5 a generic 3D THM model is used to investigate the phenomenon of injection induced stress

rotation. A sensitivity study indicates the reservoir permeability, injection rate, and initial differential stress as the key driving factors for stress rotation. If the reservoir properties and treatment are known the observed stress rotation can be used to estimate the initial differential stress. This information can be used to verify the local stress state as provided by calibrated local models such as in Chapter 4 or is used to estimate additional reservoir characteristics.

In addition to these three manuscripts as a lead author (see section 1.2) I contributed to several additional publications (see section 1.3). A full publication list is enclosed in my curriculum vitae on page XIII.

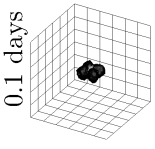

1.2 Description of Manuscripts

In the following my lead-author manuscripts that comprise this thesis are listed.

Number	1 – Chapter 3, page 21ff
Title	The stress pattern of Iceland
Status	published
Journal	Tectonophysics, 2016, Vol. 674, p. 101-113, doi: 10.1016/j.tecto.2016.02.008
Authors	**Moritz Ziegler**, Mojtaba Rajabi, Oliver Heidbach, Gylfi Páll Hersir, Kristján Ágústsson, Sigurveig Árnadóttir, Arno Zang
Contribution	I wrote the manuscript, analysed the borehole data in close collaboration with M. Rajabi, and compiled the stress data. Furthermore, I analysed the results and prepared the figures.
Number	2 – Chapter 4, page 39ff
Title	A multi-stage 3D stress field modelling approach exemplified in the Bavarian Molasse Basin
Status	published
Journal	Solid Earth, 2016, Vol. 7, p. 1365-1382, doi: 10.5194/se-7-1365-2016
Authors	**Moritz Ziegler**, Oliver Heidbach, John Reinecker, Anna M. Przybycin, Magdalena Scheck-Wenderoth
Contribution	I prepared, populated, and analysed the geomechanical models. I adapted and applied the multi-stage approach to geomechanical models. Furthermore, I wrote the manuscript and prepared the figures.
Number	3 – Chapter 5, page 61ff
Title	Estimation of the differential stress from the stress rotation angle in low permeable rock
Status	published
Journal	Geophysical Research Letters, 2017, 44 (13), 6761-6770, doi: 10.1002/2017GL073598
Authors	**Moritz Ziegler**, Oliver Heidbach, Arno Zang, Patricia Martínez-Garzón, Marco Bohnhoff
Contribution	I developed the sensitivity analysis as well as prepared and analysed the thermo-hydro-mechanical model. Furthermore, I wrote the manuscript and prepared the figures.

1.3 Additional Manuscripts

In the following, manuscripts are listed that originate from collaborations during my work as a PhD-candidate and on which I am named as co-author.

Title	Contemporary tectonic stress pattern of the Taranaki Basin, New Zealand
Status	published
Journal	Journal of Geophysical Research: Solid Earth, 2016, Vol. 121, p. 6053-6070, doi: 10.1002/2016JB013178
Authors	Mojtaba Rajabi, **Moritz Ziegler**, Mark Tingay, Oliver Heidbach, Scott Reynolds
Contribution	I compiled and analysed the stress data records and contributed to the generation of figures.
Title	Crustal stress pattern across scales revealed in the new World Stress Map database 2016
Status	in review
Journal	Nature Geosciences
Authors	Oliver Heidbach, Mojtaba Rajabi, X. Cui, Karl Fuchs, Birgit Müller, John Reinecker, Karsten Reiter, Mark Tingay, Furen Xie, Friedeman Wenzel, **Moritz Ziegler**, Mary-Lou Zoback, Mark D. Zoback
Contribution	I compiled stress data records and assisted in the generation of figures.
Title	Crustal stress and strain pattern of New Zealand
Status	in prep.
Journal	Earth and Planetary Science Letters
Authors	Mojtaba Rajabi, **Moritz Ziegler**, Oliver Heidbach, Mark Tingay
Contribution	I compiled and analysed the stress data records and contributed to the generation of figures.
Title	Influence of fluid flow on the temperature field of the central Upper Rhine Graben
Status	in prep.
Journal	–
Authors	Jessica Freymark, Mauro Cacace, **Moritz Ziegler**, Judith Sippel, Kristian Bär, Rüdiger Schellschmidt, Magdalena Scheck-Wenderoth
Contribution	I helped with the discretization of the model.

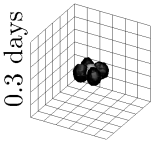

2 Scientific Principles

This thesis investigates the in-situ stress state in the earth's upper crust and anthropogenic stress changes. In parts of the work numerical modelling is used in order to simulate the stress state and its changes. In this chapter the fundamental description of the stress state by the stress tensor, the estimation of the in-situ stress state, and the basics of numerical modelling are presented.

2.1 The Stress Tensor

Stress is a physical quantity that is described by a tensor proposed by Cauchy (1827). This provides a way to define the stress state in any desired point without the necessity to refer to auxiliary geometric features such as planes or directions (Cauchy, 1827; Jaeger et al., 2007; Zang and Stephansson, 2010). The stress tensor σ_{ij} is defined as

$$\sigma_{ij} = \begin{bmatrix} \sigma_{11} & \sigma_{12} & \sigma_{13} \\ \sigma_{21} & \sigma_{22} & \sigma_{23} \\ \sigma_{31} & \sigma_{32} & \sigma_{33} \end{bmatrix} = \begin{bmatrix} \sigma_{11} & \tau_{12} & \tau_{13} \\ \tau_{21} & \sigma_{22} & \tau_{23} \\ \tau_{31} & \tau_{32} & \sigma_{33} \end{bmatrix}. \tag{2.1}$$

The nine components of the stress tensor are subdivided into the three normal stresses σ_{11}, σ_{22}, and σ_{33} that act normal to the planes spanned by the axes of a Cartesian coordinate system and the six shear stresses that act parallel to these planes (Fig. 2.1). In agreement with Newton's *actio = reactio* a stress in a certain direction is counterbalanced by an equally large stress in the opposite direction. Under this assumption that is also known as *Cauchy's first law* the symmetry of the stress tensor becomes evident and thus it holds for the shear stresses that

$$\begin{aligned} \sigma_{12} &= \sigma_{21} \\ \sigma_{13} &= \sigma_{31} \\ \sigma_{23} &= \sigma_{32} \end{aligned} \tag{2.2}$$

which implies that

$$\sigma_{\mathbf{ij}} = \sigma_{\mathbf{ij}}{}^{T} \tag{2.3}$$

reducing the number of independent components to six (Fig. 2.1). Still, a further simplification is achieved by the principal axis transformation that rotates the stress tensor in a way that the shear stresses dissipate. The stress tensor in the principal axes system

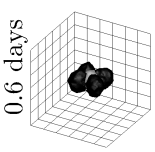

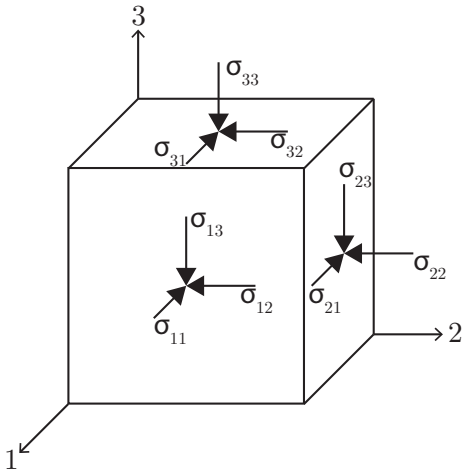

Figure 2.1: The three-dimensional Cauchy stress tensor in the geomechanical definition of the stress state (compression positive).

$$\sigma_{ij} = \begin{bmatrix} \sigma_1 & 0 & 0 \\ 0 & \sigma_2 & 0 \\ 0 & 0 & \sigma_3 \end{bmatrix} \tag{2.4}$$

consist of the principal stresses σ_1, σ_2, and σ_3 that are perpendicular to each other. They are arranged in a way that σ_1 has the largest and σ_3 the smallest magnitude. Mathematically the eigenvalues and eigenvectors of the stress tensor are sought and represent the magnitude and orientation of principal stresses respectively (Zang and Stephansson, 2010).

With the basic assumption in geomechanics that the vertical stress S_v which is generated by the overburden is one of the principal stresses in the upper crust the remaining two principal stresses are horizontal. Thus, only four unknowns are required to define the so called reduced stress tensor: The magnitudes of (1) the maximum horizontal stress S_{Hmax}, (2) the minimum horizontal stress S_{hmin}, and (3) S_v as well as (4) the orientation of S_{Hmax} or S_{hmin} (Zoback, 2010).

Dependent on the relative magnitudes of the three principal stresses (Anderson, 1905) defines three different generic types of faults that are created in different stress regimes (Fig. 2.2). If the S_v is the

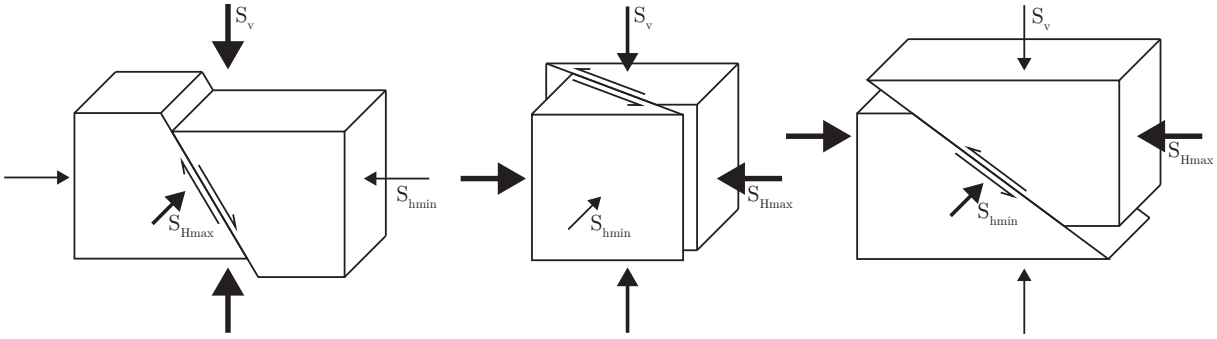

Figure 2.2: The stress regimes according to Anderson (1905) from left to right: Normal faulting ($S_v > S_{Hmax} > S_{hmin}$), strike slip faulting ($S_{Hmax} > S_v > S_{hmin}$), and thrust or reverse faulting ($S_{Hmax} > S_{hmin} > S_v$).

largest stress component a normal faulting regime prevails with faults striking in orientation of the S_{Hmax} and dipping 60 °. A strike slip regime is indicated by S_v as the intermediate stress magnitude; faults strike in an orientation of S_{Hmax} + 30 ° and dip vertically. A thrust or reverse faulting regime exists if S_v is the smallest stress component. Faults that are generated in a thrust faulting regime have a strike in the orientation of S_{hmin} and a dip of 30 °. Exact representations of these faults are seldom and usually the fault mechanism is a combination of two of the generic fault types. Therefore, a quantification by the Regime Stress Ratio (RSR) is often used that assigns numerical values between 0 (pure extension) and 3 (pure compression) to the prevalent stress regime (Simpson, 1997).

2.2 Stress Measurements

The estimation of the reduced stress tensor is required in order to authoritatively address stress related issues. In this section methods are presented which are used to estimate the orientation of the stress tensor (orientation of S_{Hmax}) and to derive the magnitudes of S_{Hmax}, S_{hmin}, and S_v.

2.2.1 Stress Orientation

The S_{Hmax} orientation is globally compiled in the World Stress Map (WSM) with currently 42,870 quality ranked data records (Heidbach et al., 2016b, 2010; Sperner et al., 2003; Zoback et al., 1989). The S_{Hmax} orientation is indicated by a variety of methods such as from focal mechanism solutions, stress inversions of focal mechanism solutions, geological fault slip data, borehole observations, stress relief measurements, or volcanic vent or dyke alignments (Heidbach et al., 2010; Heidbach, 2016). In order to allow comparability between the orientations from a variety of different indicators each data records is assigned a quality between A (S_{Hmax} believed to be within ±15 °), B (S_{Hmax} ±15–20 °), C (S_{Hmax} ±20–25 °), D (S_{Hmax} ±25–40 °), and E (no reliable information, S_{Hmax} > ±40 °) (Heidbach et al., 2010; Sperner et al., 2003; Zoback, 1992). Usually A–C data records are used for interpretation. The WSM quality ranking chart provides individual guidelines for the assessment of the quality according to the inherent reliabilities of each type of indicator (Heidbach et al., 2010). In addition to the orientation of S_{Hmax}, the quality, the coordinates of the data records location, and the type of indicator the WSM database also lists further information on the stress data records such as an identifier, the depth of the data record, a location name, country, the stress regime, and references (Heidbach, 2016). Furthermore, indicator specific information such as trend and plunge of the PBT axes of seismic events, the length of borehole breakouts, or the properties of geologic rock samples can be included (Heidbach, 2016). The database also includes information on the stress magnitudes often available for data records obtained from hydraulic fracturing (Heidbach et al., 2010; Zang et al., 2012).

Focal mechanism solutions of seismic events are used to estimate the stress orientation from the orientations of the principal strain axes. Even though the stress axes and strain axes are not the same (McKenzie, 1969) the latter are a good proxy for the orientations of the principal stress axes (Célérier, 2010). Still, the only reliable assertion is that the maximum principal stress axes lie within the dilatational quadrant of the focal mechanism (McKenzie, 1969). Therefore, the WSM quality of a single focal mechanism solution cannot be better than C (Heidbach, 2016). The formal stress inversion of several focal mechanism solutions of several seismic events which occurred in a uniform stress field provides the orientations of the principal stress axes (Gephart and Forsyth, 1984; Michael, 1987; Rivera and Cisternas, 1991). Thus, the reliability is clearly improved compared to single focal mechanism solutions and hence a better quality than C can be assigned. Furthermore, an averaging of several focal mechanism solutions

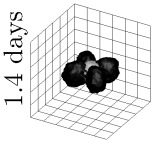

or the construction of composite solutions provides basic indications on the stress field.

Analogously to recent seismic events fault slip observed by seismometers, geological observations of palaeo fault slip data sets or the inversion of several such mechanisms provide the orientation of the stress field (Angelier, 1979; Michael, 1984; Angelier, 1984). Geologically observed fault slip data are usually a manifestation of seismic events that occurred in the past. Since the stress field changes with time, such fault slip data may indicate a palaeo stress field rather than the current stress field. In order to prevent such a misinterpretation the observed fault slip has to have occurred during the Quaternary according to the WSM guidelines (Sperner et al., 2003; Zoback, 1992).

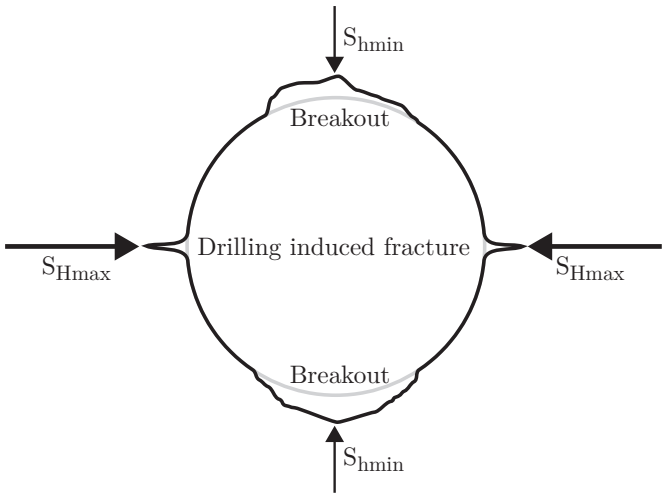

Figure 2.3: Borehole features that are used as indicators of the current stress field orientation in a downhole view with the initial borehole radius (grey circle) and the borehole wall that is deformed and altered due to the current stress state (black line). The orientation of the minimum circumferential stress and the orientation of S_{Hmax} is indicated by drilling induced fractures. The orientation of the maximum circumferential stress and S_{hmin} is indicated by borehole breakouts (Zang and Stephansson, 2010).

The effects of the stress field on engineered structures such as boreholes are used as indicators of the stress orientation (Bell and Gough, 1979; Aadnoy, 1990). The orientation and characteristics of borehole wall failure indicate the orientation of the maximum and minimum circumferential stress around the borehole which in turn depends on the stress field (Kirsch, 1898; Scheidegger, 1962). Borehole breakouts are broad zones where compressive failure causes the borehole wall to spall off due to the prevailing stress field (Zoback et al., 1985; Bell, 1990). They occur on both opposing sides of the borehole wall and indicate the orientation of S_{hmin} (Fig. 2.3). Drilling induced (tensile) fractures are slim vertical fractures that occur in the orientation of S_{Hmax} on both sides of the borehole wall (Fig. 2.3). Borehole breakouts or drilling induced tensile fractures can be observed by methods such as borehole image logs or caliper logs (Bell, 1996; Plumb and Hickman, 1985; Zang and Stephansson, 2010). Borehole images provide up to 360 ° visual information of the borehole wall (Ellis and Singer, 2010; Rider and Kennedy, 2011). They are either videos recorded by a camera but more often they are processed and colour coded representations of resistivity logs or acoustic travel-time logs (Rider and Kennedy, 2011). They enable a highly detailed assessment of the borehole wall (Fig. 3.3 on page 27 in Chapter 3). Caliper logs indicate the borehole diameter by a measurement in two or three orientations (four arm or six arm caliper) that are constantly rotating around the borehole axis (Ellis and Singer, 2010). Thereby the orientation of vertical ruptures in the borehole wall is indicated (Plumb and Hickman, 1985; Bell, 1996).

The orientation of intentional failures of borehole walls during hydraulic fracturing is also an indicator

of the stress orientation and is observed by borehole images or caliper logs (Haimson and Fairhurst, 1969; Haimson and Rummel, 1982). Stress relief measurement methods such as overcoring indicate the orientation of S_{Hmax} by the orientation of maximum extension of a rock specimen after it is extracted (Zang and Stephansson, 2010; Hast, 1973; Walsh, 1965; Leeman, 1964). However, a high number of single overcoring experiments are required in order to obtain reliable results. These methods also provide information on the stress magnitudes (Sec. 2.2.2).

In addition, the orientation of Quaternary intrusions and the alignment of volcanic vents are used as stress indicators (Nakamura, 1977; Nakamura et al., 1977). Further methods that can provide information on the orientation of S_{Hmax} are strain recovery methods (Teufel, 1983), core disking (Funato et al., 2012), borehole slotter (Corthésy et al., 1999), petal centreline fractures (Plumb and Cox, 1987), or shear wave splitting (Crampin and Peacock, 2005).

2.2.2 Stress Magnitudes

Even though the orientation of the reduced stress tensor is often available and possible to estimate to a certain extent the knowledge of stress magnitudes is essential. However, the measurement of all three principal stress magnitudes remains a challenge. A database that compiles magnitude data records from different measurement methods is the Quantitative World Stress Map (Q-WSM) (Zang et al., 2012). The Q-WSM applies a quality ranking to the stress magnitude data records according to the reliability and uncertainties of the applied measurement technique (Zang et al., 2012). Thereby an analysis and comparison of stress magnitude data records from different types of indicators is feasible.

The magnitude of the vertical stress S_v is the easiest stress magnitude to estimate by

$$S_v = \int_0^z \rho(z) g dz \tag{2.5}$$

with the density ρ dependent on the depth z and the gravitational acceleration g. The density is estimated from the average density of the rock. Alternatively, ρ is provided by borehole data such as a density log or the analysis of drill cores. Estimations of the magnitude of S_{hmin} which is often the least principal stress magnitude, and the magnitude of S_{Hmax} require more advanced techniques.

Hydraulic fracturing is a method that allows the determination of the least principal stress (Scheidegger, 1962; Haimson and Fairhurst, 1969). Therefore a designated part of a borehole is separated by packers and the fluid pressure is increased until the borehole wall fails and a fracture opens normal to the orientation of the least principal stress (Hubbert and Willis, 1972; Ljunggren et al., 2003). From the temporal evolution of fluid pressure during stimulation the shut-in pressure can be derived which is equivalent to the magnitude of the least principal stress (Hubbert and Willis, 1972). Furthermore, leak-off tests (LOTs) provide the break-down pressure of the formation which can used as an approximation of the least principal stress magnitude that is often S_{hmin} (Zang and Stephansson, 2010). Formation integrity tests (FITs) provide a lower boundary for the magnitude of the least principal stress by testing the borehole without a leak-off (Zang et al., 2012). The difference between the measured pressure at which the rock is still stable and the actual minimum principal stress magnitude is not known for FITs.

Overcoring or stress relief techniques are the only methods that can actually measure the magnitude of S_{Hmax} in addition to the magnitude of S_{hmin} (Hast, 1969; Sjöberg et al., 2003; Ljunggren et al., 2003). These methods rely on the recovery of elastic strain relaxation after the extraction of cores from boreholes that allows determination of the S_{Hmax} and S_{hmin} magnitudes (Ljunggren et al., 2003; Amadei and Stephansson, 1997). However, for a significant result a large amount of expensive measurements and a detailed knowledge of the rock properties are required (Sjöberg et al., 2003). Still, the uncertainties

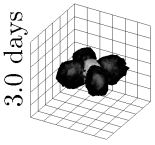

of this method remain high especially when compared to S_{hmin} magnitudes obtained from hydraulic fracturing (Martin, 2007).

Borehole breakouts can provide information on the magnitude of the least principal stress given a detailed knowledge of the rock properties (Wiprut et al., 1997; Zoback et al., 2003). This is achieved by an investigation of the width of the breakout zones. In addition, the frictional limit theory uses information on the rock strength, the stress regime, and the other two magnitudes in order to define a feasible range for the S_{Hmax} magnitude (Zoback et al., 2003). Even though in some circumstances significant results can be obtained by a limitation of the possible range of stress states and magnitudes in general the uncertainties remain very high.

2.2.3 Rock Failure

In order to assess the stability of rock a definition is required for the condition for which the rock fails. Such a failure criterion depends on the stress state and the rock properties. Various failure criteria valid for different failure modes and different applications exist (Zang and Stephansson, 2010). The Coulomb criterion is one of the most often applied criteria to indicate shear failure (mode II). It is defined by

$$\tau = \mu\sigma + C \tag{2.6}$$

with the shear stress τ, the coefficient of internal friction μ, the normal stress σ_n, and the cohesion C. The coefficient of internal friction in the upper crust is usually between 0.5 and 0.85 and is expressed as

$$\mu = tan\Phi \tag{2.7}$$

in terms of Φ the angle of internal friction (Zang and Stephansson, 2010; Byerlee, 1978).

The failure criterion is visualised in the Mohr-Coulomb diagram with the stress state indicated by the Mohr circle (Figs. 2.4a and 1.2). If the Mohr circle touches the failure envelope defined by the failure criterion the rock fails. The angle α of a newly created fracture to the orientation of $S1$ is theoretically defined by

$$\alpha = \pm(45^\circ \mp 0.5\Phi) \tag{2.8}$$

Alternatively it is simply indicated by the angle α in the Mohr-Coulomb diagram (Fig. 2.4a).

If the rock mass is already fractured and so called pre-existing faults are present Equation 2.6 is altered. The angle of internal friction may decrease and the cohesion C is significantly reduced or set to zero. Therefore, a second failure envelope that is only valid for pre-existing fractures is added to the Mohr-Coulomb diagram (Fig. 2.4b). If a pre-existing fault oriented with an according angle in the range between β_1 to β_2 to the orientation of $S1$ exists failure occurs on this fault (Fig. 2.4b). However, no failure will occur for faults oriented with an angle outside that range (e.g. γ in Fig. 2.4b) or in the intact rock.

Various measures exist for the derivation of potential for rock stability and fault criticality (Zang and Stephansson, 2010; Jaeger et al., 2007; Brady and Brown, 2004). Simple ways of estimation are achieved by the derivation of scalar values such as slip tendency for pre-existing fractures or the creation of optimally oriented faults (Morris et al., 1996). Slip tendency provides an estimate of the criticality of faults in terms of the relative distance of the fault from failure in the Mohr circle (Fig. 2.4c); ST = 0 indicates an entirely stable situation and ST = 1 indicates the moment of fracture (re)activation (Fig. 2.4c). Slip tendency is defined as

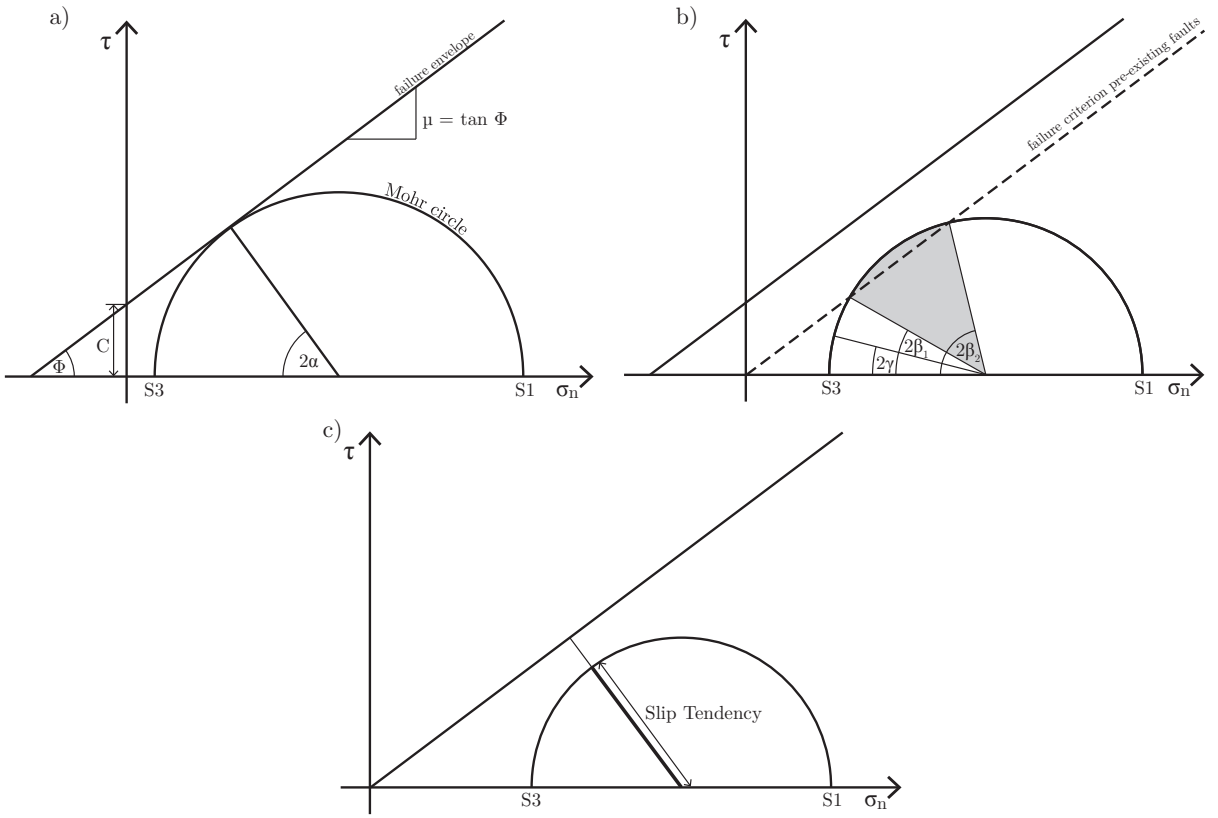

Figure 2.4: The Mohr-Coulomb failure criterion; normal stress σ_n on the x-axis, shear stress τ on the y-axis. If the Mohr circle touches a failure envelope the rock fails. (a) The maximum principal stress $S1$ and the minimum principal stress $S3$ are connected by the Mohr circle. The failure envelope is defined by Equation 2.6. The angle α is between the orientation of $S1$ and the orientation of the new fracture. (b) If pre-existing fractures are present failure may occur earlier if the fractures have an orientation in the range between β_1 and β_2 (grey area). In this example no failure occurs for faults oriented outside this range (e.g. with an angle of γ) or in the intact rock mass. (c) Slip tendency is the current mean stress $\sigma_m = 0.5(S1 - S3)$ in relation to the mean stress when failure occurs on a plane with a certain orientation. It is a measure of the criticality of faults in terms of their distance from failure and for rock stability in term of the creation of a new optimally oriented fault (Morris et al., 1996).

$$\mathrm{ST} = \frac{\tau_{max} - C}{\sigma_n} \mu^{-1} \tag{2.9}$$

with the maximum shear stress τ_{max}. For the estimation of slip tendency on pre-existing faults C is set to zero. Thus, slip tendency is used to assess both the stability of the rock and the criticality of pre-existing faults. Temporal changes of slip tendency during reservoir treatment indicate whether the engineering increases or decreases rock stability and fault criticality.

2.3 Numerical Methods

In this thesis a numerical method is used in order to solve the partial differential equation of motion to estimate the in-situ stress state in a volume (Chap. 4) and to solve the fully coupled partial differential equation that describes thermo-hydro-mechanical (THM) processes (Chap. 5). In geoscientific context numerical modelling methods such as the finite element method, the discrete element method (Yoon et al., 2014a), the finite volume method (Rutqvist, 2011; Jeanne et al., 2015), or other methods are

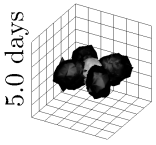

applied (Jing and Stephansson, 2007). The finite element method that is applied here is often used in order to simulate the contemporary in-situ stress state (e.g. Fischer and Henk, 2013; Hergert et al., 2015), kinematic behaviour (e.g. Buchmann and Connolly, 2007; Hergert et al., 2011), or steady-state processes (e.g. Stephenson et al., 2009; Freymark et al., 2017). Furthermore, for problems related to subsurface processes which are often anthropogenically induced by the engineering of fluid or gas reservoirs the finite element method is used (e.g. Blöcher et al., 2010; Van Wees et al., 2003; Westerhaus et al., 2008; Wassing et al., 2014; Jeanne et al., 2014). A key advantage of the finite element method is that irregular and complex geometries such as in geoscientific problems are easily adapted and solved. A simulation of fracture propagation with a finite element method is possible but requires large computational power compared to other methods such as the discrete element method.

2.3.1 The Finite Element Method (FEM)

The finite element method originates from the need to solve partial differential equations in complex geometries. Instead of solving the partial differential equation for an entire volume it is solved several times for several fractions of the volume (Zienkiewicz, 1987). These fractions of the volume are defined by nodes which are connected by edges. For a linear ansatz function the field variables change linearly on the edge from one node to the next (Fig. 2.5). The solution of the entire volume is computed by solving the equation of each single fraction. Thereby it is piecewise linearly approximated.

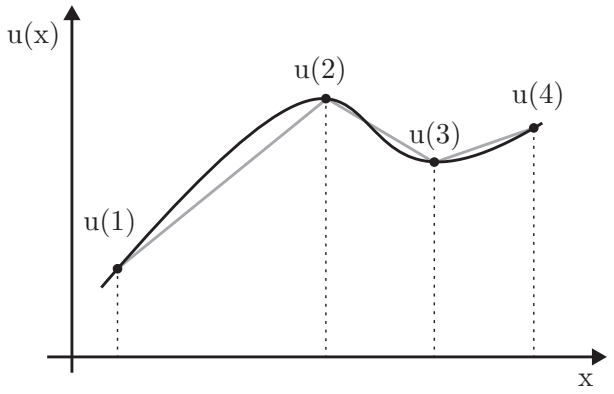

Figure 2.5: The solution of a deformation problem $u(x)$ (y-axis) and the distance x (x-axis). The analytical solution with a continuous first derivative (black line) in comparison to the approximated piecewise linear solution computed by the finite element method (grey line) are indicated.

The nodes and edges define the so called *finite elements* (Fig. 2.6a). In 2D mostly triangles and quadrilaterals are used. In 3D tetrahedrons and brick elements are used by default with the occasional use of pyramid and wedge elements. The variability of the element geometries is limited by certain quality criteria such as the minimum and maximum size of interior angles and Jacobian matrix determinate. Each finite element represents a discretized part of the volume with individual material properties and a known ansatz function. If the discretization, i.e. the size of elements, is reasonably chosen with respect to the size and variability of the geometry a result is provided that includes all major structures and material inhomogeneities and is a good approximation of a continuous analytical solution. Thus, the finite element method requires the discretization of the model volume into a mesh that consists of single elements (Fig. 2.6b). The discretization is achieved with pre-processor software that is focussed on the fast generation of a high quality mesh. The necessary differences of the mesh from the input geometry should be handled with care and kept to a minimum (Fig. 2.6b).

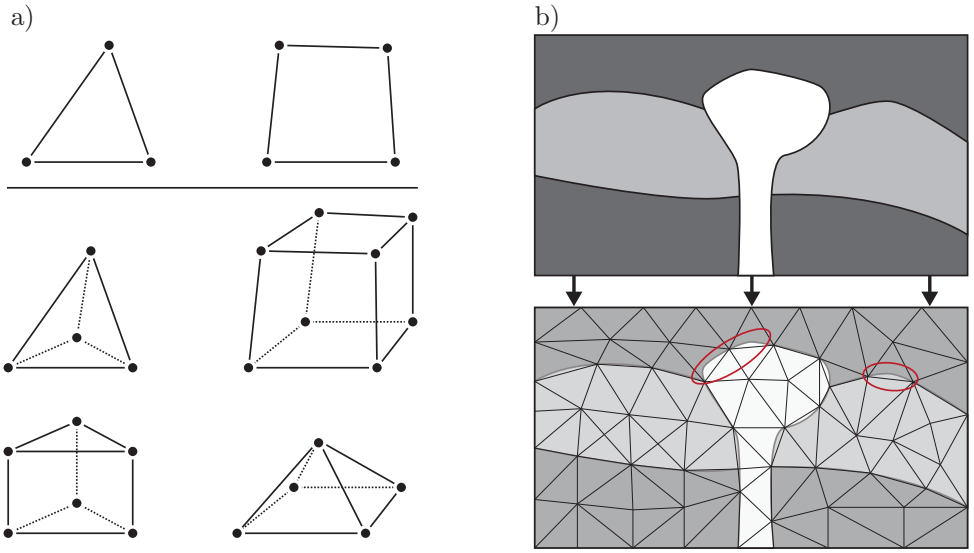

Figure 2.6: Basics of geometry meshing for finite element models. (a) Commonly used element types in this work. Top left to right: 2D triangle and quadrilateral. Bottom clockwise: 3D Tetrahedron, brick element, pyramid, and wedge element. (b) An exemplified 2D subsurface geometry (top) and a very coarse discretization of the same geometry (bottom). Some areas that are challenging for discretization in terms of distance between geometry and mesh are indicated in red.

2.3.2 Geomechanical Models

In order to estimate the contemporary in-situ stress state which is the result of the geologic history and tectonic evolution a calibrated 3D geomechanical-numerical model is applied. The problem is described by the partial differential equation of the equilibrium of forces that has the form of

$$\frac{\partial \sigma_{ij}}{\partial x_j} + f_i = 0 \tag{2.10}$$

with the stress tensor σ_{ij}, the body forces f_i such as gravity which is computed from the density of the rock, and the gravitational acceleration g.

The underlying assumption is that the material in the upper crust behaves elastically. In contrast to other studies (e.g. Maury et al., 2014; Yoon et al., 2014a; Sobolev and Babeyko, 2005), plasticity, failure of the rock, pore pressure changes, thermal effects and viscous behaviour can be neglected to answer the questions addressed here. Hence the behaviour of the rock within the volume can be described by Hooke's law

$$\sigma_{ij} = \sum_{k=1}^{3} \sum_{l=1}^{3} c_{ijkl} \epsilon_{kl} \tag{2.11}$$

with the fourth order elasticity tensor c_{ijkl}, the second order strain tensor ϵ_{kl}, and $i, j, k, l = 3$. The strain tensor can be expressed in terms of deformation as

$$\epsilon_{kl} = \frac{1}{2} \left(\frac{\partial u_k}{\partial x_l} + \frac{\partial u_l}{\partial x_k} \right) \tag{2.12}$$

with the spatial coordinates $\vec{x}$ and the deformation vector $\vec{u}$. In an isotropic media the stiffness tensor c_{ijkl} can be simplified to be dependent on only two variables so that Hooke's law is stated as

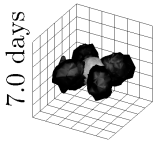

$$\sigma_{ij} = \lambda \epsilon_{kk} \delta_{ij} + 2G\epsilon'_{ij} \tag{2.13}$$

with the deviatoric part of the strain tensor ϵ'_{ij} and Lamé's parameters λ and G which can be rewritten as

$$\begin{aligned} \lambda &= \frac{E\nu}{(1+\nu)(1-2\nu)} \\ G &= \frac{E}{2(1+\nu)} \end{aligned} \tag{2.14}$$

in terms of the elastic Young's module E and the Poisson ratio ν.

For complex tectonic settings with discontinuities or density and strength contrasts an analytical solution of the partial differential equation of the equilibrium of forces cannot be estimated. Thus the finite element method is used to solve the partial differential equation that describes the in-situ stress state at discrete points within a volume. With given boundary conditions the partial differential equation (Eqn. 2.10) is reduced to a linear equation system

$$\mathbf{f} = \mathbf{K} \cdot \mathbf{u} \tag{2.15}$$

with the acting forces $\mathbf{f}$, the stiffness matrix $\mathbf{K}$, and the displacement $\mathbf{u}$. The displacement boundary conditions of the model and the Young's module, Poisson ratio and density of each element need to be defined. Then a solver software is applied to invert the sparsely populated matrix and thereby solve the equations.

2.3.3 Thermo-Hydro-Mechanical (THM) Models

In addition to the modelling of the in-situ stress state the modelling and simulation of THM processes such as fluid extraction and/or (re)injection are of interest. The modelling of such processes requires an extension of the geomechanical models in order to simulate the effect of thermal and pore pressure changes on the stress state.

According to Terzaghi (1943) pore pressure changes affect the entire stress tensor equally as described in

$$\sigma_{ij,eff.} = \sigma_{ij} + \delta_{ij} \Delta P_P \tag{2.16}$$

with the effective stress $\sigma_{ij,eff.}$ and the pore pressure changes ΔP_p. However, according to Rudnicki (1986) and Altmann et al. (2010) the stress state after injection or depletion in reservoirs is estimated by

$$\sigma_{ij}(\mathbf{x}, t) = -\frac{q}{\rho_f c} \frac{(\lambda_u - \lambda)G}{4\pi r \alpha_B (\lambda_u + 2G)} \left\{ \delta_{ij} \left[\operatorname{erfc}\left(\frac{1}{2}\zeta\right) - \frac{2}{\zeta^2} g(\zeta) \right] + \frac{x_i x_j}{r^2} \left[\operatorname{erfc}\left(\frac{1}{2}\zeta\right) + \frac{6}{\zeta^2} g(\zeta) \right] \right\} \tag{2.17}$$

where $\mathbf{x}$ is the location vector, q is a constant fluid flux, ρ_f the fluid density, $\zeta = r/\sqrt{dt}$ the Boltzmann variable, d the diffusivity, λ and G the drained Lamé parameters, and λ_u the undrained first Lamé parameter. Furthermore,

$$
\begin{aligned}
g(\zeta) &= \frac{1}{2\sqrt{\pi}} \int_0^{\zeta} s^2 \exp\left(-\frac{1}{4}s^2\right) ds \\
&= \operatorname{erf}\left(\frac{1}{2}\zeta\right) - \frac{1}{\sqrt{\pi}}\zeta exp\left(-\frac{1}{4}\zeta^2\right)
\end{aligned}
\tag{2.18}
$$

with erf as the error-function. The diffusivity d is computed as

$$
d = \frac{K(\lambda_u - \lambda)(\lambda + 2G)}{\alpha_B^2(\lambda_u + 2G)} \tag{2.19}
$$

with the hydraulic conductivity K and the Biot-Willis coefficient α_B. The hydraulic conductivity K can be expressed in terms of permeability k_f as

$$
K = \frac{k_f \rho_{fluid} g}{\mu_{dyn}} \tag{2.20}
$$

with the density of the fluid ρ_{fluid} and the dynamic viscosity of the fluid μ_{dyn}.

Equation 2.17 shows that the stress state after injection and/or depletion depends on the duration of injection or depletion t, the injection rate q, the permeability, and most importantly as well on the location of observation $\mathbf{x}$. Thus, pore pressure changes affect the stress state anisotropically.

Furthermore, thermally induced stress changes in 3D are described by

$$
\sigma_{ij,thermal} = 2G\epsilon_{ij} + \lambda\delta_{ij}(\epsilon_{11} + \epsilon_{22} + \epsilon_{33}) - \delta_{ij}\frac{E\alpha_T \Delta T}{1 - 2\nu} \tag{2.21}
$$

with the Young's module E, the thermal strain ϵ_{ij}, the thermal expansion coefficient of the rock material α_T, and the temperature difference ΔT (McTigue, 1986; Zimmerman, 2000; Jacquey et al., 2015).

Hence, for THM models the previously described effects are formulated as partial differential equations and coupled with the partial differential equation of equilibrium of motion without acceleration. Such models, in addition to the Young's module and the Poisson ratio, require the definition of the material properties porosity, permeability, bulk modulus of the solid grains and drained bulk modulus for the solid media. Furthermore, for both solid media and wetting fluid the material properties density, thermal conductivity, specific heat, latent heat, and thermal expansion are required.

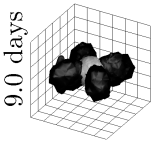

3 The Stress Pattern of Iceland

Moritz Ziegler[1,2], Mojtaba Rajabi[3], Oliver Heidbach[1], Gylfi Páll Hersir[4], Kristján Ágústsson[4], Sigurveig Árnadóttir[4], Arno Zang[1,2]

[1] Helmholtz Centre Potsdam, German Research Centre for Geosciences, Telegrafenberg, 14473 Potsdam, Germany

[2] University of Potsdam, Institute of Earth and Environmental Science, Karl-Liebknecht-Str. 24-25, 14476 Potsdam-Golm, Germany

[3] Australian School of Petroleum, The University of Adelaide, Adelaide, SA 5005, Australia

[4] Iceland GeoSurvey (ÍSOR), Grensásvegur 9, 108 Reykjavík, Iceland

Journal: Tectonophysics, 2016, Vol. 674, p. 101–113, doi: 10.1016/j.tecto.2016.02.008

Received 13 August 2015, Revised 29 January 2016, Accepted 2 February 2016, Available online 12 February 2016

Abstract

Iceland is located on the Mid-Atlantic Ridge which is the plate boundary between the Eurasian and the North American plates. It is one of the few places on earth where an active spreading centre is located onshore but the stress pattern has not been extensively investigated so far. In this paper we present a comprehensive compilation of the orientation of maximum horizontal stress (S_{Hmax}). In particular we interpret borehole breakouts and drilling induced fractures from borehole image logs in 57 geothermal wells onshore Iceland. The borehole results are combined with other stress indicators including earthquake focal mechanism solutions, geological information and overcoring measurements resulting in a dataset with 495 data records for the S_{Hmax} orientation. The reliability of each indicator is assessed according to the quality criteria of the World Stress Map project.

The majority of S_{Hmax} orientation data records in Iceland is derived from earthquake focal mechanism solutions (35%) and geological fault slip inversions (26%). 20% of the data are borehole related stress indicators. In addition minor shares of S_{Hmax} orientations are compiled, amongst others, from focal mechanism inversions and the alignment of fissure eruptions. The results show that the S_{Hmax} orientations derived from different depths and stress indicators are consistent with each other.

The resulting pattern of the present-day stress in Iceland has four distinct subsets of S_{Hmax} orientations. The S_{Hmax} orientation is parallel to the rift axes in the vicinity of the active spreading regions. It changes from NE–SW in the South to approximately N–S in central Iceland and NNW–SSE in the North. In the Westfjords which is located far away from the ridge the regional S_{Hmax} rotates and is parallel to the plate motion.

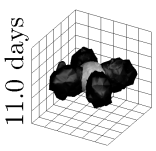

3.1 Introduction

The regional stress pattern along divergent plate boundaries has not been studied extensively yet due to the inaccessibility of submerged Mid Oceanic Ridges. Few and scattered earthquake focal mechanism solutions are the only sources of stress orientation in these areas in the World Stress Map (WSM) database (Heidbach et al., 2008, 2010). These indicators generally show a ridge parallel maximum horizontal stress (S_{Hmax}) orientation (Zoback et al., 1989; Zoback, 1992). In intra-plate regions the orientation of S_{Hmax} is often parallel to the absolute plate motion in a first order approximation and therefore generally normal to the ridges and subduction zones (e.g. Richardson, 1992; Müller et al., 1992; Grünthal and Stromeyer, 1992; Zoback, 1992; Zoback et al., 1989). A systematic rotation of S_{Hmax} from ridge parallel to ridge normal has been observed close to ridges in the Indian Ocean (Wiens and Stein, 1984) and at Mid Oceanic Ridges in general (Sykes, 1967; Sykes and Sbar, 1974).

Iceland is one of the few places on the Earth with an onshore divergent plate boundary (e.g. Ward, 1971; Sæmundsson, 1979; Einarsson, 1991, 2008; Bird, 2003). It is in a unique geological and tectonic setting, where an oceanic ridge (the Mid-Atlantic Ridge) traverses a (purported) mantle plume (e.g. Lawver and Müller, 1994; Wolfe et al., 1997; Allen et al., 2002). The rift zones in and around Iceland are dominated by various volcanic systems of different extents and activities (Thordarson and Larsen, 2007; Jóhannesson and Sæmundsson, 1998). Induced by the hotspot the plumbing of the volcanic systems is extended compared to a usual divergent plate boundary (Allen et al., 2002). As the plate boundary crosses the hotspot, it breaks up into a complex series of segments. Purely divergent segments are the Northern Volcanic Zone (NVZ) in North Iceland, and the sub-parallel Western and Eastern Volcanic Zones (WVZ, EVZ) in South Iceland which are generally assumed to be the expression of a ridge jump (Sæmundsson, 1979; Einarsson, 1991, 2008). In the South, the South Iceland Seismic Zone (SISZ) is the connecting segment between the Reykjanes peninsula and the Eastern Volcanic Zone (Sæmundsson, 1974, 1979; Einarsson, 1991; Stefánsson et al., 2008). In the North the Tjörnes Fracture Zone (TFZ) connects the NVZ to the southern end of the submarine Kolbeinsey Ridge (Sæmundsson, 1974, 1979; Einarsson, 1991; Stefánsson et al., 2008). The WVZ and NVZ are joined by a transverse E–W zone across central Iceland. Outside of the immediate plate boundary, volcanism occurs in the South Iceland Volcanic Zone, the Snæfellsnes Volcanic Zone and the Öræfajökull Volcanic Zone (e.g. Jakobsson, 1979; Sæmundsson, 1978, 1986).

This volcano-tectonic setting has received a particular attention in the first compilation of the present-day crustal stress by Hast (1969). Since then, several researchers investigated the state of stress in different parts of Iceland. An extensive campaign of in-situ stress measurements from shallow overcorings was carried out by Schäfer and Keil (1979). Haimson and Rummel (1982) conducted hydro-fracturing experiments in six onshore boreholes. Furthermore, extensive field campaigns to collect geological fault slip data provide information on the current and palaeo-stress field in Iceland as well as its temporal evolution (Gudmundsson et al., 1996; Bergerat and Angelier, 1998; Garcia and Dhont, 2005; Angelier et al., 2008; Plateaux et al., 2012). In total, the compilation of stress data records in the World Stress Map (WSM) database 2008 resulted in 38 data records of the contemporary S_{Hmax} orientation and the stress regime (9 focal mechanism solutions, 5 hydro-fracturing orientations, and 24 overcoring measurements, Heidbach et al., 2008, 2010). However, this small data set is not sufficient to reveal the presumably high variability of the stress field pattern of Iceland. This is especially important since Iceland's peculiar location causes extensive interactions between tectonic and volcanic processes which influence the local stress field (e.g. Sæmundsson, 1979; Gudmundsson, 2006; Andrew and Gudmundsson, 2008).

In this paper we present a new comprehensive compilation of the contemporary S_{Hmax} orientation

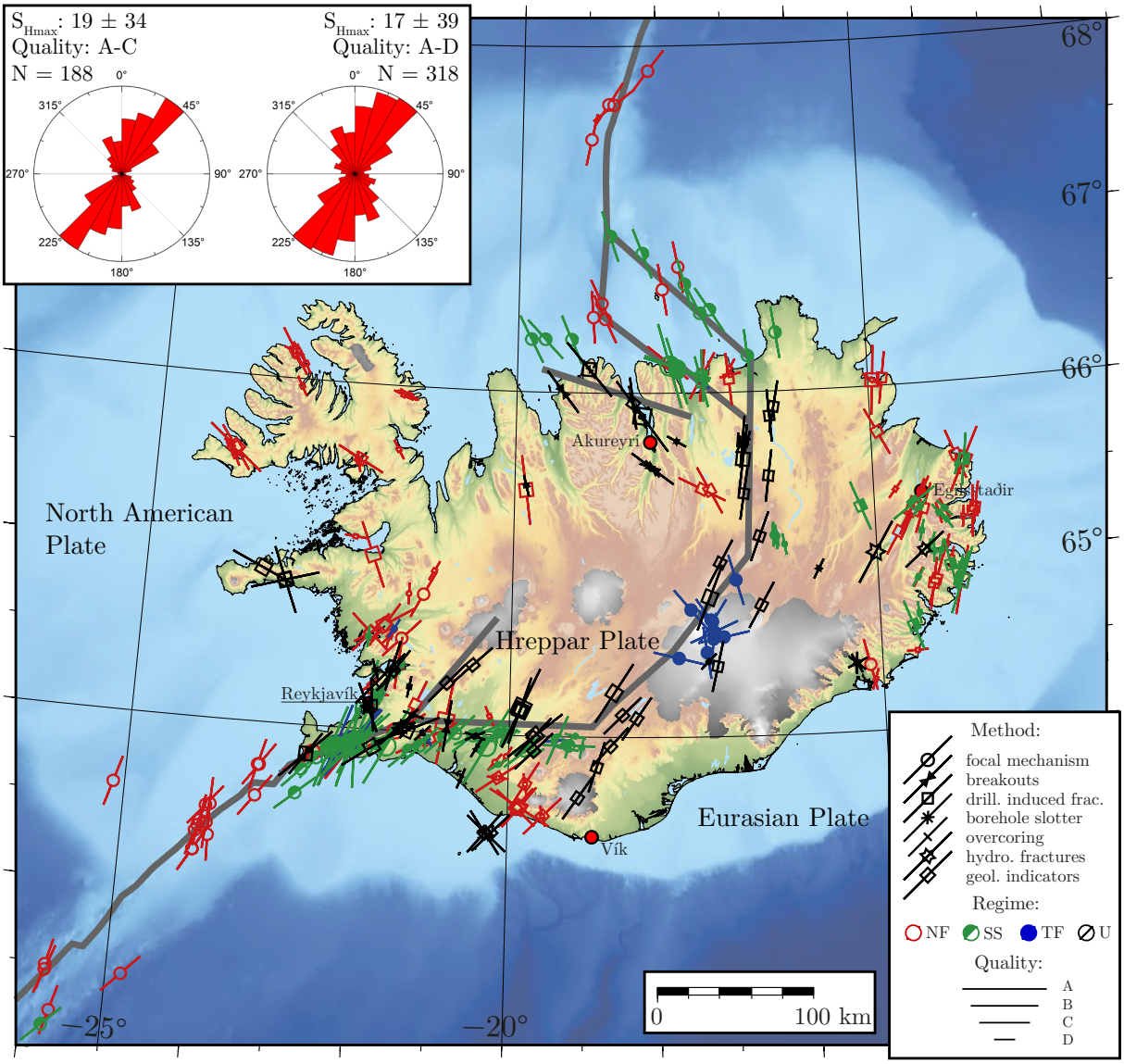

Figure 3.1: The first comprehensive stress map of Iceland with 318 data records with A–D quality according to the World Stress Map quality criteria (Sperner et al., 2003; Heidbach et al., 2010). Lines represent the orientation of maximum horizontal stress S_{Hmax} with the length proportional to quality. The symbols in the middle of the lines display the method used for stress determination. The colour coding is according to the stress regime with red indicating normal faulting, green indicating strike slip faulting, blue indicating thrust/reverse faulting, and black for unknown regimes. The plate boundaries according to Bird (2003) and Einarsson (2008) are indicated in grey. Two rose diagrams display the unweighted frequency distribution of the A–C and A–D quality data respectively. Mean S_{Hmax} orientations and their standard deviations are calculated with the circular statistics of bi-polar data (Mardia, 1972).

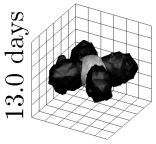

for Iceland with 495 data records (Fig. 3.1). In particular, we analysed ≈37 km of borehole acoustic image logs from 57 geothermal wells to interpret present-day stress indicators, i.e. borehole breakouts (BOs) and drilling induced fractures (DIFs). Furthermore, we revised the 38 data records from the WSM 2008 and conducted an extensive literature study to compile published focal mechanism solutions and geological stress indicators, e.g. fault slip inversions or the alignment of volcanic vents and fissures. All data records are quality ranked according to the WSM quality ranking system (Zoback, 1992; Sperner et al., 2003; Heidbach et al., 2010). We identify the regional pattern of the S_{Hmax} orientation by four different stress provinces with different mean S_{Hmax} orientations on Iceland.

3.2 Stress Data Compilation

The first comprehensive compilation of the contemporary S_{Hmax} orientation was made by Sbar and Sykes (1973) who mapped the stress pattern in North America. This effort was later institutionalised by Zoback et al. (1989) in the framework of the WSM project (e.g. Müller et al., 1992; Heidbach et al., 2010). In the literature there are several methods to determine the orientation of S_{Hmax} in a rock volume (Ljunggren et al., 2003; Zoback et al., 1989; Zang and Stephansson, 2010). However, these different methods may result in different orientations due to the depth of the phenomena, different reliability, or superposition of different forces at different scales (Heidbach et al., 2007). Hence, comparison between the S_{Hmax} from different indicators have received a particular attention to establish a quality ranking scheme for the WSM database (Zoback and Zoback, 1991; Zoback, 1992; Zoback et al., 1989; Sperner et al., 2003; Heidbach et al., 2010). Following this scheme each data record is assigned a quality from A (reliability of orientation ± 15 °), B (± 15–20 °), C (± 20–25 °), D (± 25–40 °) up to E (> ± 40 °) (Heidbach et al., 2010). A detailed description of the WSM quality ranking scheme for individual stress indicators can be found in Zoback (1992), Sperner et al. (2003), and Heidbach et al. (2010).

Our stress data compilation extends from 62 ° to 68 ° northern latitude and from -11 ° to -26 ° longitude. The image log data from the 57 geothermal wells resulted in 36 new A–D stress data records. In addition, we estimated 17 S_{Hmax} orientations from crater rows of fissure eruptions of different volcanic systems. Furthermore, an extensive literature review resulted in 374 new stress data records which are mainly from focal mechanism solutions of earthquakes. These new data records are from different earthquake catalogues such as the Global CMT (Ekström et al., 2012; Dziewonski et al., 1981), Geofon Potsdam (GEOFON Data Centre, 1993) and Zurich Moment Tensors. Furthermore data records were included from published papers by Angelier et al. (2004); Batir (2011); Bergerat et al. (1990); Bergerat and Angelier (1998); Bergerat et al. (1998); Bergerat and Plateaux (2012); Bjarnason and Einarsson (1991); Einarsson (1979, 1987); Forslund and Gudmundsson (1991); Garcia et al. (2002); Garcia (2003); Green et al. (2014); Gudmundsson et al. (1992, 1996); Gudmundsson (1995); Jakobsson (1979); Jefferis and Voight (1981); Hagos et al. (2008); Haimson and Voight (1977); Keiding et al. (2009); Khodayar and Franzson (2007); Kristjánsdóttir (2013); Lund and Slunga (1999); Lund and Bödvarsson (2002); Nakamura (1977); Plateaux et al. (2014); Rögnvaldsson and Slunga (1994); Roth et al. (2000); Schäfer and Keil (1979); Sigmundsson et al. (2005); Sigurdsson (1970); Soosalu and Einarsson (1997); Stefánsson (1966); Tibaldi et al. (2013) and Villemin et al. (1994). The detailed dataset of the Iceland stress map is provided in the supplementary material. In the following sections we briefly describe each individual stress indicator used for the Iceland stress dataset.

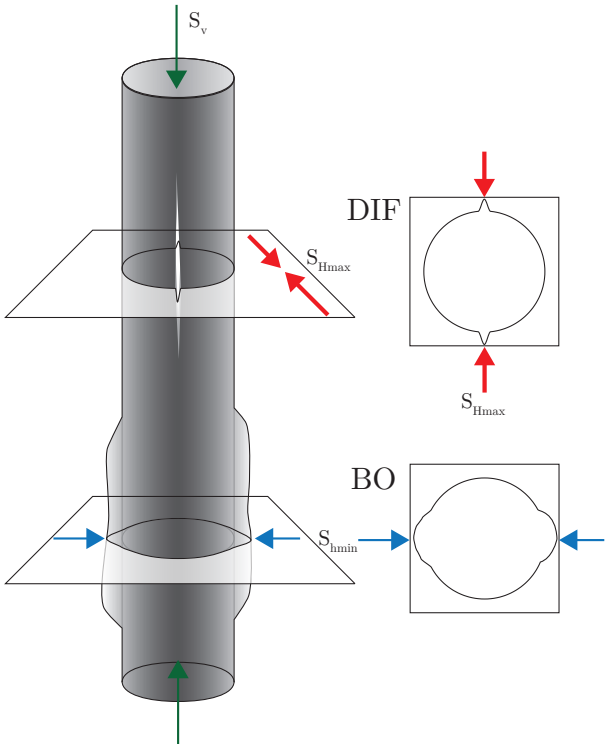

Figure 3.2: A vertical borehole section with stress indicator pairs. Top: Drilling induced fractures (DIFs) are narrow vertical fractures which indicate the orientation of S_{Hmax}. Bottom: Borehole Breakouts (BOs) are broad vertical widened zones of the borehole which indicate the orientation of S_{hmin}. These two features occur diametrically on both sides of the borehole wall.

3.2.1 Borehole Data

The possibility to determine the in-situ stress orientation from failure of borehole walls was first recognised by Bell and Gough (1979) in Alberta, Canada. They showed that if the stresses around a borehole exceed the strength of the rock, some pieces of the borehole wall spall off and the borehole is elongated in one orientation. According to Kirsch (1898) and Scheidegger (1962) the highest stresses around a circular hole are encountered perpendicular to the orientation of maximum compression (S_{Hmax}). These resulting broad elongated zones of so called borehole breakouts (BO, see Fig. 3.2) indicate the orientation of minimum horizontal stress (S_{hmin}) which is perpendicular to S_{Hmax} under the assumption that the vertical stress (S_v) is one of the principal stresses (Bell and Gough, 1979).

Furthermore, if the minimum circumferential stress around a borehole wall is smaller than the tensile strength of the rock, drilling induced fractures (DIF, see Fig. 3.2) occur (Aadnoy, 1990; Aadnoy and Bell, 1998). Therefore drilling induced fractures are recognised as an indicator for the orientation of S_{Hmax} as well (Wiprut et al., 1997; Bell, 1996; Sperner et al., 2003).

Acoustic image logs provide a picture of the borehole wall based on acoustic contrast of borehole wall and fluids. Borehole breakouts usually appear as broad vertical zones of a low acoustic amplitude on opposite sides of the borehole wall (separated by 180 °) while drilling induced fractures are indicated by narrow vertical zones of low amplitude (Fig. 3.3). A pair of DIFs or BOs on opposite sides of the borehole wall is considered as a single feature. Since the shapes of BOs and DIFs depend on rock strength and the elastic properties of rocks and these features are time dependent, incipient breakouts form at the initial stage of the formation of borehole breakouts (Aadnoy and Bell, 1998).

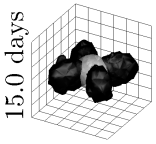

Table 3.1: Stress indicators from the analysed acoustic borehole images of A–D Quality. All the information required for the WSM quality ranking is included in the Table. Azimuth: Interpreted orientation of S_{Hmax}. Number: The amount of recognised feature pairs (BOs or DIFs) in a single well. S.D.: Standard deviation calculated according to the circular statistics of bi-polar data by Mardia (1972) with a weighting depending of the length (short: L) of the feature. Length: The added length of the fractured borehole sections. Top and Bottom: The depth of the uppermost and lowermost stress indicator found in the borehole. Depth: The mean between top and bottom. Date: Date of the tool run.

Borehole ID	Latitude	Longitude	Azimuth	Type	Depth [km]	Quality	Location	Date	Number	S.D.	Length [m]	Weighting	Top [m]	Bottom [m]
HH-08	63.425023	-20.25904	133	BO	1.05	C	Vestmannaeyjar	20050415	11	13	22	L	789	1719
RN-34	63.83951	-22.660869	36	BO	1.95	C	Reykjanes	20150328	15	12	25	L	1412	2628
RN-34	63.83951	-22.660869	47	DIF	2.45	B	Reykjanes	20150328	20	9	40	L	2317	2612
KH-34	63.98881	-20.44006	67	BO	0.04	D	Kaldárholt	20050322	1	0	2	L	38	40
KH-34	63.98881	-20.44006	109	DIF	0.2	D	Kaldárholt	20050322	2	2	3	L	55	390
SO-01	63.995165	-21.13729	47	DIF	0.32	D	Sogn/Ölfus	20050322	3	13	6	L	314	325
HE-21	64.008906	-21.3438	41	BO	1.67	D	Hellisheiði	20060215	11	14	16	L	1608	1748
HE-21	64.008906	-21.3438	67	DIF	1.35	B	Hellisheiði	20060215	53	14	123	L	912	1812
HE-58	64.033132	-21.376734	35	DIF	1.9	D	Hellisheiði	20150830	3	15	5	L	1609	2200
HN-01	64.026124	-21.45102	45	BO	0.9	C	Hellisheiði	20050405	20	22	26	L	866	977
HN-01	64.026124	-21.45102	44	DIF	0.85	D	Hellisheiði	20050405	7	18	10	L	768	977
HK-15	64.041	-20.81377	8	BO	0.1	C	Grímsnes	20060303	33	15	25	L	37	183
HN-12	64.044597	-21.38636	84	DIF	1.5	D	Hellisheiði	20101021	7	21	11	L	1152	1878
HN-16	64.045106	-21.3862	86	DIF	2.06	D	Hellisheiði	20101018	6	12	9	L	2021	2187
NJ-28	64.098521	-21.270345	107	DIF	1.05	D	Nesjavellir	20150625	5	9	11	L	1029	1057
HF-01	64.391916	-15.34195	151	DIF	0.6	D	Hoffell	20130221	10	11	17	L	424	805
ASK-29	64.393293	-15.343563	130	BO	0.11	D	Hoffell	20120926	6	16	6	L	103	123
ASK-57	64.393898	-15.34267	4	BO	0.28	D	Hoffell	20120926	1	0	1	L	283	284
ASK-122	64.393778	-15.33175	65	DIF	0.35	D	Hoffell	20150924	7	14	13	L	338	375
HO-02	65.04501	-22.77176	60	BO	0.36	D	Stykkishólmur	20070215	1	0	4	L	366	370
ST-16	65.5519	-18.07022	127	BO	0.35	C	Sigtún/Eyjafjörður	20050126	28	9	37	L	111	671
ST-16	65.5519	-18.07022	140	DIF	0.4	D	Sigtún/Eyjafjörður	20050126	5	7	16	L	329	508
BO-3	65.562966	-18.10464	107	DIF	0.07	D	Botn	20130122	3	13	10	L	60	80
KV-01	65.692163	-16.81934	29	BO	1.43	D	Krafla	20060803	1	0	1	L	1435	1437
KV-01	65.692163	-16.81934	164	DIF	1.43	D	Krafla	20060803	2	8	2	L	1432	1435
K-18	65.702026	-16.73063	17	BO	0.74	D	Krafla	20081118	2	4	6	L	733	750
HJ-17	65.855115	-18.2105	151	DIF	0.15	D	Hjalteyri	20020221	2	11	2	L	122	170
HJ-13	65.855337	-18.21303	145	DIF	0.06	D	Hjalteyri	20020220	1	0	3	L	62	65
HJ-20	65.856089	-18.21142	141	BO	1	D	Hjalteyri	20050202	4	8	12	L	784	1176
HJ-20	65.856089	-18.21142	144	DIF	0.75	A	Hjalteyri	20050202	60	11	136	L	352	1346
HJ-15	65.859457	-18.21754	154	DIF	0.2	D	Hjalteyri	20020223	1	0	2	L	204	207
ARS-32	65.931479	-18.33783	163	BO	0.75	D	Árskógsströnd	20060608	6	19	6	L	668	842
ARS-32	65.931479	-18.33783	173	DIF	0.55	C	Árskógsströnd	20060608	17	14	36	L	206	713
SK-28	65.997822	-19.33668	143	BO	0.5	C	Hrolleifsdalur	20051008	55	25	137	L	240	821
SD-01	66.127507	-18.96229	146	BO	0.45	D	Skarðdalur/ Tröllaskagi	20100925	2	3	3	L	430	537
SD-01	66.127507	-18.96229	140	DIF	0.5	B	Skarðdalur/ Tröllaskagi	20100925	20	11	69	L	319	687

Iceland's volcano-tectonic setting results in large geothermal resources which are extracted by various boreholes (Ragnarsson, 2015). In 2002 through 2015 the Iceland GeoSurvey (ÍSOR) ran borehole image logs in 57 geothermal and scientific boreholes mainly in the South Iceland Lowlands and around Akureyri and Krafla in the North (Fig. 3.4 for locations). From these data we collected and analysed 37 km of acoustic image logs. Most of them are slightly deviated from vertical ($< 10°$) which still allows the interpretation of stress related features in every stress regime (Mastin, 1988; Tingay et al., 2005; Peška and Zoback, 1995).

27 boreholes contained at least one BO or one DIF (Tab. 3.1, Fig. 3.4). In the case that both BOs and DIFs are found in the same well, the independently inferred S_{Hmax} orientations are generally in good agreement with each other (Tab. 3.1). In addition to the newly analysed borehole images 3 BOs and 1 DIF from published articles were included. In the analysed boreholes stress indicators are mainly found between the surface and 1 km depth. Some few BOs/DIFs are located in deeper sections of the boreholes

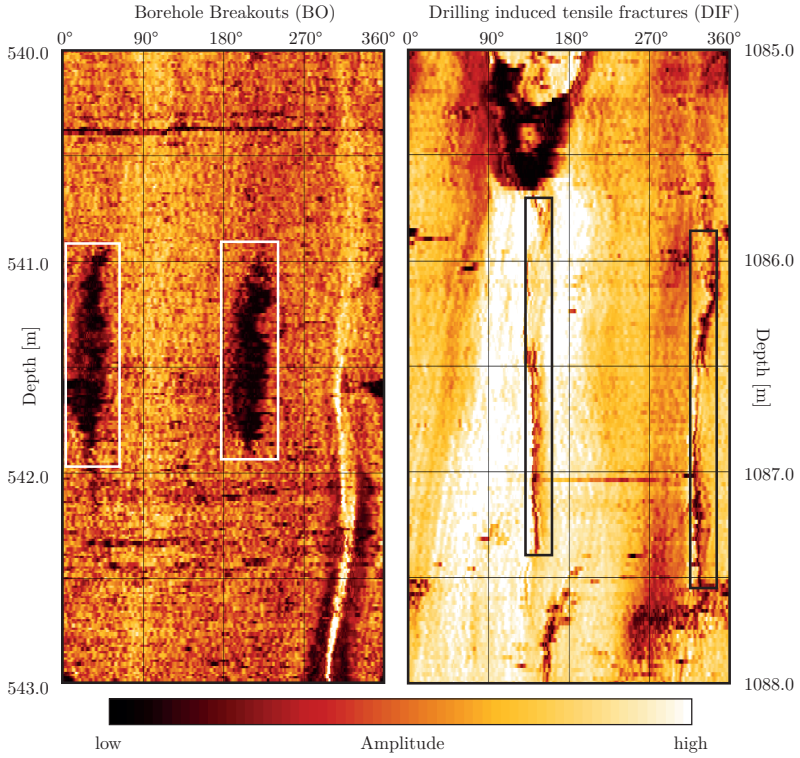

Figure 3.3: Borehole related stress indicators in acoustic image logs. Left: Borehole breakouts (BOs) in well ST-16 Sigtún close to Akureyri. The inferred overall orientation of S_{Hmax} from BOs is 127 ° in this well. Right: Drilling induced fractures (DIFs) in well HJ-20 Hjalteyri close to Akureyri. The inferred overall orientation of S_{Hmax} from DIFs is 144 ° in this well. The location of the two wells is shown in Figure 3.4.

with a maximum depth of 2.34 km in well RN-34 on the Reykjanes peninsula (Fig. 3.4). Thus borehole stress data bridge the gap between shallow stress indicators from geological data and focal mechanism solutions at greater depth.

Table 3.1 shows the results of image log interpretation and observed BOs/DIFs in the studied wells. 11 data records have a A–C quality and 25 data records have a D quality. The high number of low quality data records is partly related to the challenges of well-logging in a high temperature and igneous environment resulting in a partly poor image quality. Special tools adapted to high temperatures are required and can only remain in the well for a short time period (Ásmundsson et al., 2014). In addition, in some of the studied wells image tools were not centralised and produced low quality images with numerous vertical artefacts which do not allow a reliable detection of BOs and DIFs.

3.2.2 Focal Mechanism Solutions

Focal mechanism solutions of earthquakes have been used to infer stress information, both orientation and relative magnitudes, in the deeper part of the earth's crust which is beyond common drilling plans (Sbar and Sykes, 1973; Gephart and Forsyth, 1984; Zoback, 1992; Heidbach et al., 2010). The orientation of S_{Hmax} is estimated from the principal strain axes of the double couple components of the focal mechanism (McKenzie, 1969; Barth et al., 2008). However, these axes are not necessarily reliable proxies for the stress axis orientation (McKenzie, 1969; Célérier, 2010; Heidbach et al., 2010). Therefore, single focal mechanism solutions are never eligible for a quality better than C in the WSM database (Heidbach et al.,

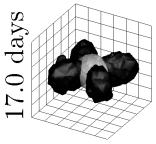

2010; Barth et al., 2008). A stress determination through the averaging of several focal mechanism's P, B, and T axes (FMA) is less reliable and is hence assigned D quality.

Between 1994 through 2007 250,000 seismic events were recorded by the Iceland Meteorological Office with 11 events of M > 5 (Einarsson, 1991, 2008; Jakobsdóttir et al., 2002; Jakobsdóttir, 2008; Einarsson et al., 1977; Keiding et al., 2009). The detection threshold in this time frame has been between M_l=2 and M_l=0 depending on the region (Jakobsdóttir, 2008). Focal mechanism solutions were publicly available for only a fraction of the recorded seismic events.

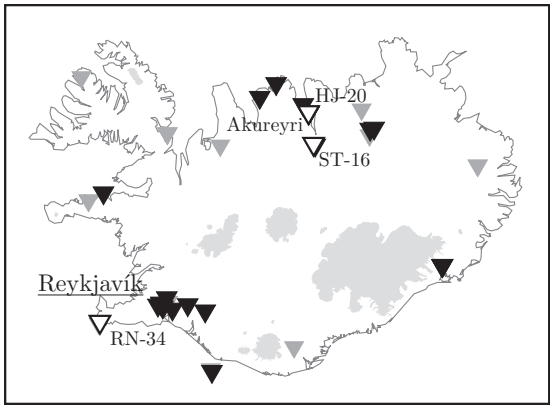

Figure 3.4: The location of geothermal boreholes with acoustic image logs. The black and grey triangles denote the location of boreholes with and without stress indicators (based on our image log analysis) respectively. The white triangles show the location of borehole HJ-20 Hjalteyri, ST-16 Sigtún (Fig. 3.3) as well as in RN-34 Reykjanes.

Presumably especially in Iceland many seismic events are related to volcanic eruptions or dyke intrusions and thus are potentially spatially and temporally restricted manifestations of the stress field (e.g. Roman et al., 2004; Sánchez et al., 2004; Einarsson, 1991; White et al., 2011). Hence they do not necessarily represent the long-term stress field but only short-term fluctuations of a perturbed regional stress field. In addition, such events may have a low double-couple and high compensated linear vector dipole (CLVD) component (Nettles and Ekström, 1998). That means the main strain component is due to an inflation or deflation above some pressure source in contrast to a double-couple mechanism (Nettles and Ekström, 1998; Ekström, 1994). Therefore events which can be spatially and temporally attributed to a volcanic eruption or rifting event are assigned E quality. However, seismic events which are only located at a volcano but cannot be linked to an eruption remain with a quality C. In the Vatnajökull area several thrust faulting events were recorded during an inter-volcanic period. Nettles and Ekström (1998) and Einarsson (1991) suggest that these events are a movement of the Barðabunga caldera rim. Hence they are not directly temporarily related to a volcanic eruption and assigned the quality C.

Furthermore, the phenomenon of induced seismicity in geothermal reservoirs is reported in Iceland (Flóvenz et al., 2015). The stress field in geothermal or hydrocarbon reservoirs can change significantly due to depletion and/or reinjection (Segall and Fitzgerald, 1998; Martínez-Garzón et al., 2013). Hence, focal mechanisms of seismicity located in the vicinity or within active reservoirs are prone to exhibit a perturbed stress state compared to the virgin in-situ stress state. Therefore seismic events which are in spatial and temporal proximity to e.g. dams or geothermal power plants are identified as potentially induced and are assigned E quality as well.

In addition to single focal mechanism solutions (FMS) or an average of FMS (FMA), inversions of focal mechanisms (FMF) can be performed (e.g. Gephart and Forsyth, 1984; Angelier, 1984). Generally results from inversions provide high quality (A or B) stress data records (e.g. Keiding et al., 2009; Kristjánsdóttir,

2013). However, the inversions of focal mechanism solutions performed by Bergerat et al. (1998); Garcia et al. (2002); Angelier et al. (2004), and Plateaux et al. (2014) show the existence of two spatially or temporally different local stress fields. Due to the high quality of the inversions they are included in the database anyway but assigned E quality since these two stress fields cannot be distinguished.

3.2.3 Geological Indicators

Geological indicators of past fault slip events can also provide information on the stress state and the data reliability is equal in comparison to other methods (Sperner et al., 2003). However, to prevent a mix of palaeo-stress and contemporary stress data records, geological indicators are generally not allowed to be older than Quaternary, i.e. not older than 2.85 Ma (Zoback, 1992). Sometimes the age of a fault slip or dyke intrusion is measured (e.g. radiocarbon dating), the relative age deduced by the stratigraphy (e.g. in Bergerat and Angelier, 1998), or the maximum age of the rock is otherwise known (e.g. in Bergerat and Plateaux, 2012). If this is not the case geological maps can provide information of the age of the indicators. Note that the rule applies to the age of the fault slip and not the age of the rock, in case where they can be distinguished.

In the new Iceland Stress Map a large amount of data records are provided by geological indicators, i.e. stress tensors inferred from fault slip data. This is due to the extensive work on the stress inversions of fault data (GFI) by J. Angelier, F. Bergerat, and A. Guðmundsson undertaken in Iceland (e.g. Bergerat et al., 1990, 1998; Angelier et al., 2004).

We assessed geological indicators (GFI) following strictly the WSM quality ranking scheme (Heidbach et al., 2010; Sperner et al., 2003). Zoback (1992) discusses the possible necessity to alter the age restriction according to the tectonic setting. In case two or more different temporally successive stress states are inferred in the exact same location and both originate in the Quaternary only the youngest can be taken into account in this compilation (as is the case in e.g. Bergerat and Angelier, 1998). In several instances, stress indicators from fault slip data are in close proximity to similarly oriented stress indicators which are definitely from the currently active stress field (e.g. a borehole breakout or focal mechanism solution). Their similar orientation is at least an indicator that the age restriction also applies in Iceland. Even though local stress perturbations do occur due to the presence of local structures (Rajabi et al., 2016b; Heidbach et al., 2007) hence different S_{Hmax} orientations in close spatial proximity must not be judged as unreliable.

3.2.4 Vent Alignments

Nakamura (1977) was one of the first to recognise the alignment of volcanic vents, eruptive fissures, and dykes (GVAs) as stress indicators. GVAs are always related to volcanic eruptions which tend to be easier to date compared to fault slip, since often the age of volcanic eruptions are known.

The high volcanic activity in Iceland allows inclusion of young eruptive fissures, vent alignments and dykes from the Quaternary. We therefore included 17 GVAs produced by recent volcanic activities (even in historic times, Thordarson and Larsen 2007). The data originates in geological mapping campaigns and is also displayed in the Geologic Map of Iceland – Bedrock (Hjartarson and Sæmundsson, 2014). Table 3.2 shows the stress orientations inferred from eruptive fissures mainly deduced from geologic mapping also presented in the map by Hjartarson and Sæmundsson (2014). They are quality ranked according to the WSM criteria shown in Table 3.3.

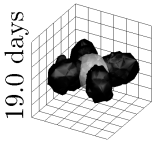

Table 3.2: Newly included volcanic vent and fissure alignments (GVAs) which are also shown in Hjartarson and Sæmundsson (2014). The required information for the World Stress Map as well as the age of the most recent eruption of the associated (central) volcano is listed. Number: The amount of parallel vent/fissure alignments. Vents: The overall number of vents/fissures which are considered. In case of parallel alignments the standard deviation is calculated according to the circular statistics of bi-polar data by Mardia (1972).

Latitude	Longitude	Azimuth	Quality	Location	Number	S.D.	Vents	Type	Last eruption/ rifting event
63.43	-20.2	45	C	Vestmannaeyjar	1		5	vents	1973 A.D.[a]
63.82	-18.83	18	C	Eldgjá (South)	1		6	fissures	934–940 A.D.[a]
63.9	-21.8	56	B	Reykjanes	4	5	21	vents	1231 A.D.[b]
63.94	-18.65	43	C	Eldgjá (Middle)	1		5	fissures	934–940 A.D.[a]
64.1	-18.3	35	C	Eldgjá (North)	1		9	fissures	934–940 A.D.[a]
64.25	-18.6	33	B	Veiðivötn	4	13	67	fissures	1477 A.D.[a]
64.29	-20.84	43	C	Þjófahraun	1		11	fissures	3600 B.P.[c]
64.4	-20.5	47	C	Langjökull	2	3	10	vents	950 A.D.[c]
64.75	-16.6	30	C	Kverkfjöll	1		7	fissures	9000 B.P.[b]
64.8	-17.3	22	B	Dyngjuháls	3	6	28	fissures	1902–1903 A.D.[e]
65	-17.15	29	C	Trölladyngja/ Frambruni	1		8	fissures	1300 A.D.[f]
65.15	-16.6	21	C	Askja	1		14	vents	1961 A.D.[b]
65.4	-16.8	9	C	Fremrinámur	1		9	vents	4000 B.P.[d]
65.5	-16.45	8	C	Nýjahraun	2	6	16	fissures	1874–75 A.D.[d]
65.6	-16.8	8	B	Reykjahlíð	4	2	16	fissures	1975–1984 A.D.[a]
65.7	-16.8	6	C	Krafla	1		10	fissures	1975–1984 A.D.[a]
65.9	-16.35	11	C	Hólssandur	1		7	fissures	Holocene[g]

[a] Thordarson and Larsen (2007), [b] Haflidason et al. (2000), [c] Sinton et al. (2005), [d] Sigurdsson and Sparks (1978), [e] Björnsson and Einarsson (1990), [f] Hjartarson (2003), [g] Hjartarson and Sæmundsson (2014)

Table 3.3: The World Stress Map quality ranking scheme version 2008 for borehole breakouts and drilling induced fractures from image logs and volcanic vent alignments (Heidbach et al., 2010). s.d. = standard deviation.

Stress indicator	**A** S_{Hmax} ±15 °	**B** S_{Hmax} ±15–20 °	**C** S_{Hmax} ±20–25 °	**D** S_{Hmax} ±25–40 °	**E** S_{Hmax} > ±40 °
Borehole Breakouts	≥ 10 distinct breakout zones and combined length ≥ 100 m in a single well with s.d. ≤ 12 °	≥ 6 distinct breakout zones and combined length ≥ 40 m in a single well with s.d. ≤ 20 °	≥ 4 distinct breakouts and combined length ≥ 20 m with s.d. ≤ 25 °	< 4 distinct breakouts or < 20 m combined length in a single well with s.d. ≤ 40 °	Wells without reliable breakouts or s.d. > 40 °
Drilling induced fractures	≥ 10 distinct fracture zones in a single well with a combined length ≥ 100 m and s.d. ≤ 12 °	≥ 6 distinct fracture zones in a single well with a combined length ≥ 40 m and s.d. ≤ 20 °	≥ 4 distinct fracture zones in a single well with a combined length ≥ 20 m and s.d. ≤ 25 °	< 4 distinct fracture zones in a single well or a combined length < 20 m and s.d. ≤ 40 °	Wells without fracture zones or s.d. > 40 °
Volcanic Vent Alignment	≥ 5 Quaternary vent alignments or "parallel" dikes with s.d. ≤ 12 °	≥ 3 Quaternary vent alignments or "parallel" dikes with s.d. ≤ 20 °	Single well-exposed Quaternary dike or Single alignment with ≥ 5 vents	Volcanic alignment inferred from < 5 vents	

3.2.5 Further Stress Indicators

In total 25 overcoring (OC) stress measurements are available throughout Iceland. Due to their shallow depth (0–30 m) the inferred stress state may be highly influenced by local topography or strength contrasts. Therefore the data records are assigned to E quality. Previous data records from the WSM 2008 which were assigned a different quality according to an outdated version of the ranking scheme were updated.

In addition 9 S_{Hmax} orientations are available from hydraulic-fracturing (HF). Previously listed HF data records were revisited and assigned a quality according to the most recent quality ranking scheme.

3.3 Stress Map & Pattern of Iceland

The new compilation of stress data for Iceland has 495 data records with 318 having A–D and 188 A–C quality (Tab. 3.4, Figs. 3.1 and 3.5). Most of the A–D quality data records are from focal mechanism solutions (35%) and geological fault inversions (26%). Borehole related indicators (BOs, DIFs, HFs) have a share of 20% while the alignments of volcanic vents, fissures and craters contribute with 8%. The inversion of several focal mechanism solutions make up 7% of the dataset.

56% of the data records are from the depth range of 0 to 1.25 km (Fig. 3.5). These are mainly geological stress indicators which are either exhumed faults or surface manifestations of the stress field. Most borehole indicators are in the same depth range. Even some very shallow focal mechanism solutions and inversions of several focal mechanisms are located in that depth range. Around 2.5 km depth stress indicators from deep boreholes and earthquake related indicators are equally abundant. Below that depth, focal mechanism solutions of seismic events are the only available stress indicators. The peak of events around 10 km is artificial because many focal mechanisms of small magnitude seismic events are assigned this depth as a default value if the depth cannot be estimated otherwise.

Some stress indicators (e.g. focal mechanism solutions, fault inversions) allow characterisation of the Andersonian faulting type of the stress field (Anderson, 1905, 1951). The method to derive the type of faulting is described by Zoback (1992). Figure 3.5 shows that normal faulting prevails at the surface. However, within the first kilometre this changes. In the following topmost 10 km a strike slip regime is dominant. With a further increase in depth the normal faulting regime prevails. Indicators for a reverse faulting regime are observed in all depths in a relatively small abundance. Nevertheless, around 1 km and 10 km depth they have a significant share.

The prevailing orientation of S_{Hmax} in Iceland inferred from A–C quality ranked data records is determined according to circular statistics of bipolar data (Mardia, 1972) which shows a mean S_{Hmax} orientation of 18 °±35 ° for the entire dataset. A closer look at Figure 3.1 demonstrates four predominant regional orientations of S_{Hmax}. In the Southwest and the Southern Iceland Lowlands S_{Hmax} is oriented approximately NE–SW (Fig. 3.6). In the Northern Volcanic Zone (north of the Vatnajökull glacier) which is presently the active rift zone, S_{Hmax} has almost N–S orientation (Fig. 3.7). S_{Hmax} is rotated by about 20 ° to NNE–SSW in the easternmost part of Iceland (Fig. 3.7). In Northern Iceland S_{Hmax} is rotated from the N–S orientation in the Northern Volcanic Zone to a predominant NNW–SSE orientation (Fig. 3.8). Finally in the Westfjords the S_{Hmax} trend is approximately NW–SE oriented (Fig. 3.9). For these four subsets the standard deviation for A–D quality data is between 19 ° and 29 ° which is comparable to other regional stress investigations (e.g. Pierdominici and Heidbach, 2012; Reiter et al., 2014; Reinecker et al., 2010).

Generally the standard deviation of the mean S_{Hmax} orientation of stress data records with A–C

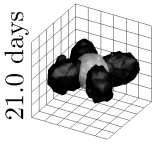

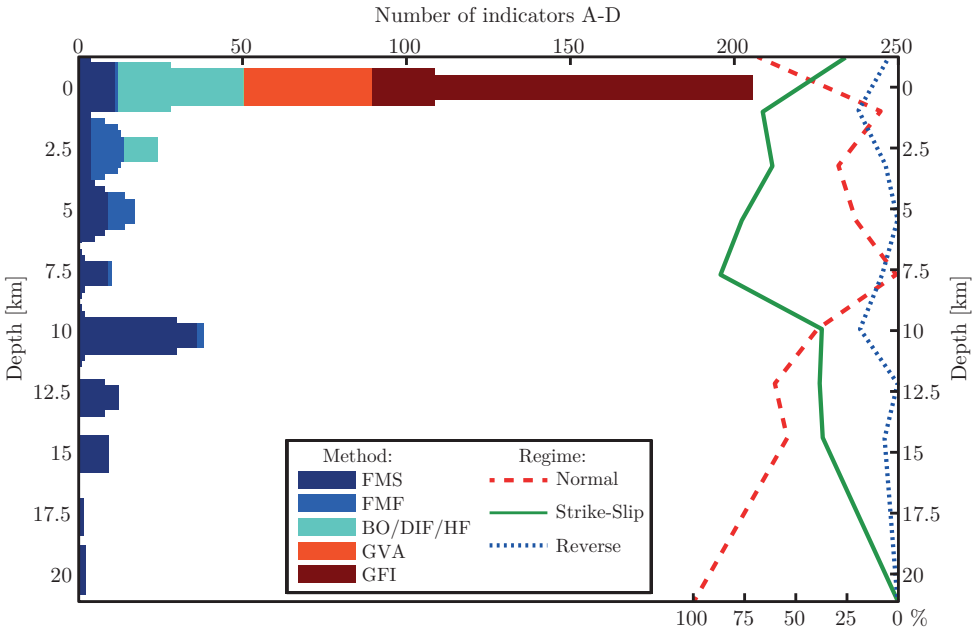

Figure 3.5: The depth distribution of the 318 stress indicators (A–D quality) is displayed here. The cluster of seismic events around a depth of 10 km is biased since many of the events with an uncertain depth were assigned this depth arbitrarily. The data is colour coded according to the type of the indicator. The width of the bar indicates the quality of the data from A (thick/left) to D (thin/right). Please note that the colour coding is independent of the width of the bar in this plot. In addition the variation of the stress regime with depth is shown on the right side.

Table 3.4: An overview of the quality and type of all stress indicators in the designated area (N: 62 ° – 68 °, W: 11 ° – 26 °). They include the revisited and re-ranked data from the WSM 2008 as well as the newly analysed data from acoustic image logs, the alignments of volcanic craters and fissures, and data records from literature research.

		Quality					
		A	B	C	D	E	Total
Type	FMF	15	7	-	-	14	36
	FMS	-	-	63	22	90	175
	FMA	-	-	-	9	-	9
	BO	-	-	6	13	30	49
	DIF	1	3	1	15	1	21
	HF	-	1	2	6	-	9
	OC	-	-	-	-	25	25
	GFI	1	11	40	63	14	129
	GVA	1	11	25	2	3	42
	Total	18	33	137	130	177	495

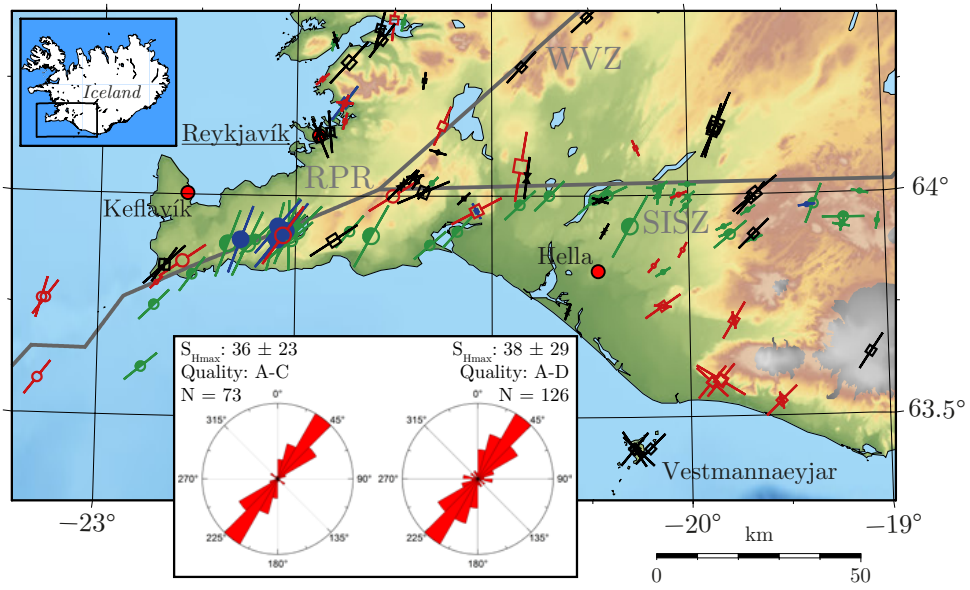

Figure 3.6: The orientation of S_{Hmax} (A–D Quality) on the Reykjanes peninsula ridge (RPR), the transform South Iceland Seismic Zone (SISZ), and parts of the Western Volcanic Zone (WVZ). Legend is the same as in Figure 3.1.

quality is found to be within ±25 ° (see rose diagrams in Figures 3.1, 3.6, 3.7, 3.8, and 3.9). If D quality data records are included the mean S_{Hmax} orientation changes by ≤ 4 °. The standard deviation increases by approximately 5 ° reflecting that D quality data introduces more noise to the dataset. Therefore D quality data should not be used individually for a local stress field analysis. Surprisingly, the standard deviation decreases by 1 ° with the introduction of 11 D quality data records in North Iceland. 10 of these data records are from boreholes and their quality depends on the short length of the feature and/or missing information on the standard deviation. These circumstances show that a well-picked distinct single feature in a borehole provides valuable information on the orientation of S_{Hmax}.

The types of available stress indicators varies in the different subsets. While all types of indicators are represented close to the plate boundary, in the Westfjords and Eastfjords the stress state is mainly derived from geological indicators and boreholes. That means that in those regions the information on the stress field is based mainly on shallow data.

Apart from lateral variations of the orientation of S_{Hmax}, the possibility of a vertical layering exists (Cornet and Röckel, 2012; Gudmundsson, 2002; Heidbach et al., 2007). In some regions, mainly sedimentary basins, moderate (Reiter et al., 2014; Reiter and Heidbach, 2014) or significant (Röckel and Lempp, 2003; Roth and Fleckenstein, 2001; Rajabi et al., 2016b) stress rotations occur with depth. For example, Rajabi et al. (2016b) reported significant rotation of the S_{Hmax} orientation with depth in the Clarence-Moreton Basin of eastern Australia due to presence of geological structures including intrusions of igneous rocks into sedimentary successions.

It is indicated by the propagation of dykes, that such a layering also exists in Iceland on a local scale (Gudmundsson, 2002, 2003). To find regional-scale depth-dependent differences in the S_{Hmax} orientation we compiled surface data (GFI, GVA) as well as intermediate (0.2–2 km) borehole indicators (BO, DIF) and deep (2–20 km) focal mechanism solutions (Fig. 3.5). In all areas where more than one type of indicator is available, the orientation of S_{Hmax} remains consistent with depth which highlights the independence from the type of stress indicator and the vertical homogeneity of S_{Hmax} throughout the crust. Thus, a potential regional-scale depth-dependency of S_{Hmax} is not observed.

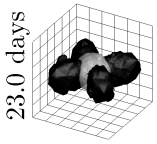

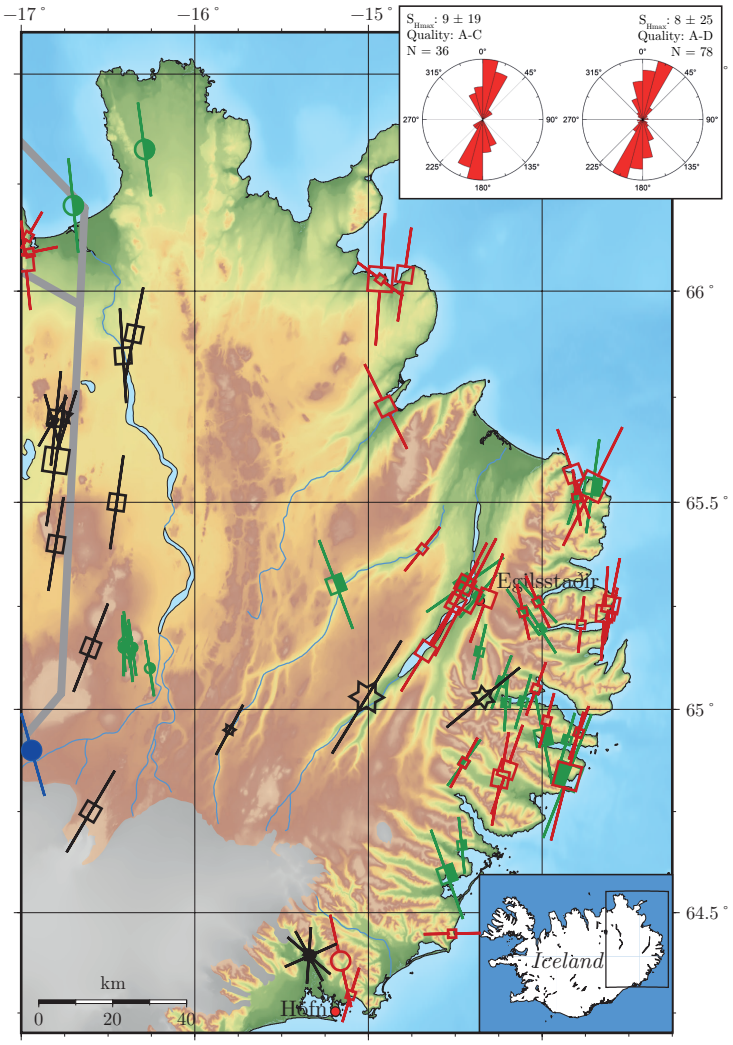

Figure 3.7: The orientation of S_{Hmax} (A–D Quality) in the Eastern Highlands/Northern Volcanic Zone and the East Fjords. Legend is the same as in Figure 3.1. Note that mainly surface geological indicators are available in this area.

3.4 Discussion

This study presents the first comprehensive and systematic compilation of the present-day tectonic stress in Iceland where all results are ranked based on a quality ranking scheme for the in-situ stress state. A high density of data records is achieved on the Reykjanes peninsula, in South Iceland, East Iceland, and the Akureyri area and Tjörnes Fracture Zone in North Iceland (Fig. 3.1). Few or no data records are available around Hofsjökull, Langjökull in the western Highlands, on the Snæfellsnes peninsula, and in the Westfjords (Fig. 3.1). Based on the available data from this compilation the orientation of the maximum compressive stress (S_{Hmax}) in Iceland is organised in four subsets and is consistent with the main plate boundaries in the region. This highlights the role of different plate boundary forces in the stress pattern of Iceland (Fig. 3.10). Furthermore the highly dynamic geological setting of Iceland is reflected in the stress field by effects of eruptions, geothermal activity, and rifting events.

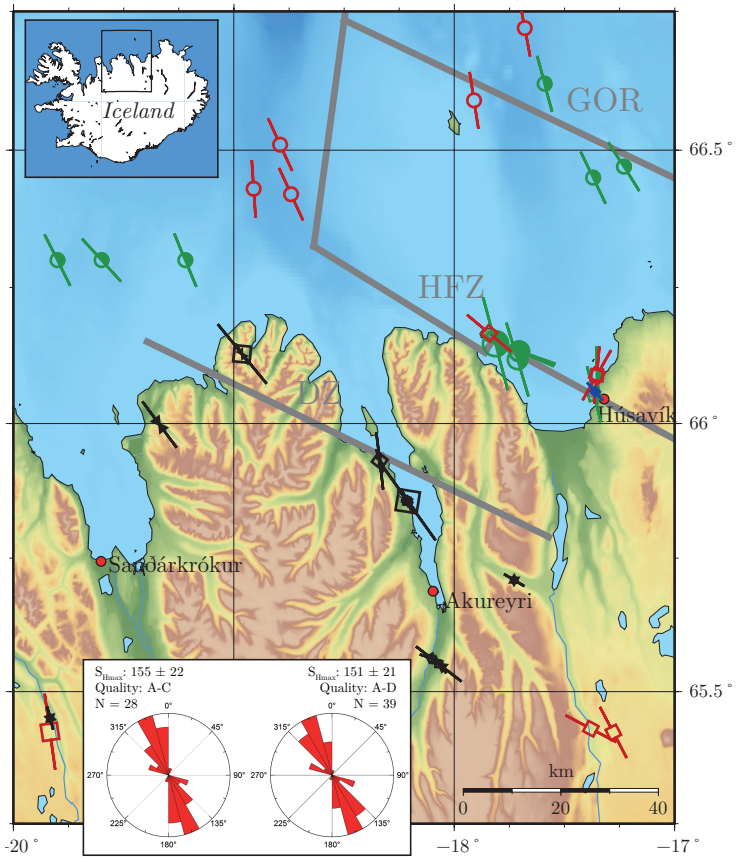

Figure 3.8: The orientation of S_{Hmax} (A–D Quality) in Northern Iceland. Displayed is the Tjörnes Fracture Zone with the Grimsey oblique rift (GOR), the Húsavík-Flatey-Zone (HFZ), and the Dalvík Zone (DZ). Legend is the same as in Figure 3.1.

3.4.1 Regional Stress Pattern

In the South–West a ridge parallel S_{Hmax} orientation can be observed along the Reykjanes Ridge (Fig. 3.1) which has the Eurasian plate to the East and the North American plate to the West (Einarsson, 2008; Bird, 2003). At the Reykjanes peninsula where the ridge makes landfall S_{Hmax} remains mostly ridge parallel (Figs. 3.1 and 3.6). This pattern of S_{Hmax} is consistent with observations by e.g. Sykes (1967) and Wiens and Stein (1984) who show ridge parallel S_{Hmax} close to the spreading centre along divergent plate boundaries in general and especially in the Indian Ocean.

Ridge parallel stress is also indicated further to the North along the WVZ (Fig. 3.1). The western boundary of the Hreppar microplate is at the WVZ and its northern boundary is the quietest Central Iceland Volcanic Zone (CIVZ) which is not represented by stress indicators here (Einarsson, 2008).

In the South the Hreppar microplate meets the Eurasian plate at the transform SISZ (Einarsson, 2008). This is one of the two areas with the largest seismic events (M=7.2) in Iceland (e.g. Stefánsson et al., 2000; Bergerat and Angelier, 2001). In the SISZ the S_{Hmax} is NNE to NE (Fig. 3.6) which is consistent with the surface ruptures of large earthquakes (e.g. Árnadóttir et al., 2003; Einarsson, 2008).

In the North–East of the SISZ the EVZ and the NVZ are the currently active rift zones (Einarsson, 2008). Most of the rifting events (Laki, Eldgjá, Krafla fires, Holuhraun) and volcanic eruptions (Grimsvötn, Gjálp, Askja, Hekla, Barðabunga) are in these two zones (Sigmundsson et al., 2015; Thordarson and Larsen, 2007). This activity is related to the current location of the centre of the hotspot

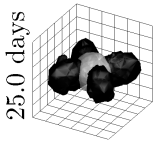

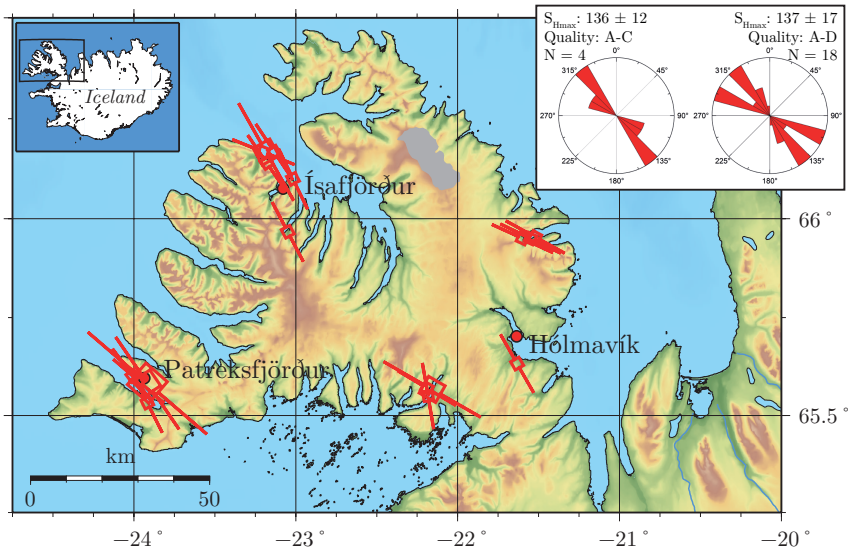

Figure 3.9: The orientation of S_{Hmax} (A–D Quality) in the Westfjords. In the oldest area of Iceland (10–16 Ma, Moorbath et al. 1968; McDougall et al. 1984) S_{Hmax} is rotated from rift parallel to rift normal. Legend is the same as in Figure 3.1. Note that only surface geological indicators are available in this area.

which is considered to be beneath the Vatnajökull glacier at the transition from the EVZ to the NVZ (e.g. Wolfe et al., 1997; Ito et al., 2003, Fig. 3.10). The S_{Hmax} is found to follow the orientation of the EVZ and NVZ which are considered as the plate boundary from NE–SW in the South to N–S in the North (Fig. 3.1). This pattern is also observed at some distance along the Icelandic east coast (Fig. 3.7).

In the North, the TFZ connects the NVZ with the Kolbeinsey Ridge north of Iceland (Sæmundsson, 1974, 1979; Einarsson, 1991; Garcia, 2003; Stefánsson et al., 2008). The spreading is distributed between the Dalvík Zone (DZ), the Húsavík-Flatey-Zone (HFZ) and the Grimsey Oblique Rift (GOR) (Sæmundsson, 1974). This is the second area with large magnitude seismic events in Iceland (Jakobsdóttir, 2008) and shows a NNW–SSE trend for the S_{Hmax} orientation which is mainly inferred from focal mechanism solutions (Fig. 3.8).

In the Westfjords which are the oldest part of Iceland (10–16 Ma, Moorbath et al. 1968; McDougall et al. 1984) and also partly on the Snæfellsnes peninsula a rotation of S_{Hmax} from ridge parallel towards ridge perpendicular is observed (Figs. 3.9 and 3.1). This rotation is interpreted as the transition from the ridge parallel stress orientation to the common intra-plate stress orientation (Wiens and Stein, 1984; Sykes, 1967; Sykes and Sbar, 1974; Müller et al., 1992; Grünthal and Stromeyer, 1992; Gudmundsson et al., 1996). This rotation is expected in some distance from the spreading centre which depends mainly on the composition of the rock and only partly on the age and distance from the ridge (Wiens and Stein, 1984). Such a rotation is also expected to occur off the Icelandic east coast to meet the overall trend of S_{Hmax} observed in Europe (e.g. Grünthal and Stromeyer, 1992; Müller et al., 1992; Heidbach et al., 2007).

Many of the stress indicators recognised in the applied quality ranking, e.g. focal mechanism solutions or borehole breakouts, are manifestations of a stress field which generally can be assumed as the currently active in-situ stress field. Still, seismic events and volcanic eruptions may change the local stress field in a very short time interval (e.g. Reasenberg and Simpson 1992; King et al. 1994; Dieterich et al. 2000). Albeit, these changes induced by seismic events are generally smaller than the regional stress magnitude (Hardebeck, 2010). Hence they are assumed to be within the uncertainty of S_{Hmax} $\pm 15°$ of even the

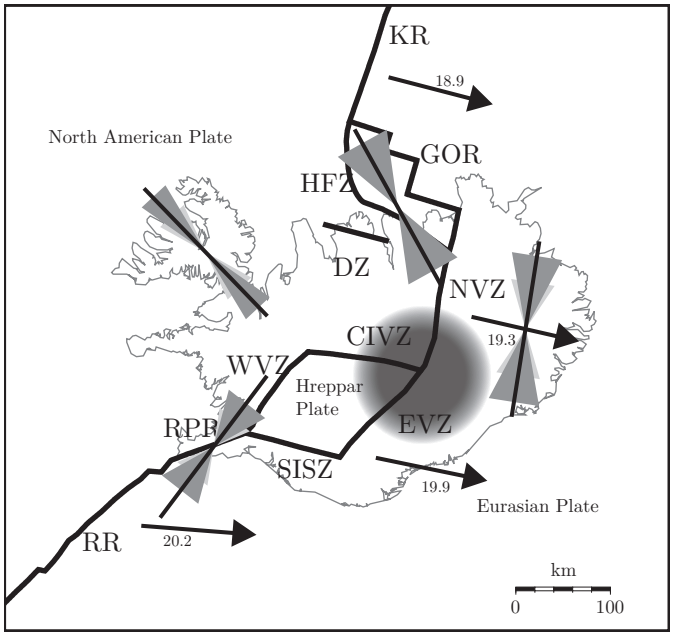

Figure 3.10: A simplified tectonic map of Iceland with the mean orientations of S_{Hmax} in the four stress provinces estimated from A–D quality data records (black lines). The standard deviation from A–C quality is shown by the large dark grey areas while the light grey areas show the standard deviation from A–D quality. The plate boundaries are from Einarsson (2008) and Bird (2003). The plate motion (mm/yr) is indicated by black arrows relative to the fixed North American plate (Geirsson et al., 2006). The continental plates and the approximate location of the hotspot (grey circle, Wolfe et al., 1997) are indicated. Furthermore the tectonic features are labelled as follows according to Einarsson (2008): RR: Reykjanes Ridge, RPR: Reykjanes Peninsula Ridge, WVZ: Western Volcanic Zone, SISZ: South Iceland Seismic Zone, EVZ: Eastern Volcanic Zone, NVZ: Northern Volcanic Zone, DZ: Dalvík Zone, HFZ: Húsavík-Flatey-Zone, GOR: Grimsey-Oblique-Ridge, and KR: Kolbeinsey Ridge.

highest quality stress indicators. As well the isostatic rebound from deglaciation is not expected to have an immediate impact on stress orientation (Plateaux et al., 2014).

3.4.2 Comparison with other Observations

A comparison of the orientation of S_{Hmax} with the direction of plate motion (Geirsson et al., 2006) shows that they are in quite large areas perpendicular to each other (Fig. 3.10). In a more local study Keiding et al. (2009) compared the stress and strain in the Reykjanes peninsula. The stress is determined from the inversion of focal mechanism from earthquake swarms while the strain is derived from GPS data. Keiding et al. (2009) conclude that the minimum horizontal stress (S_{hmin}) is parallel to the maximum horizontal strain $\dot{\epsilon}_{Hmax}$. This also holds for detailed GPS data provided by Árnadóttir et al. (2009). In the Westfjords the orientation of S_{Hmax} is sub-parallel to the plate motion (Fig. 3.9 and Árnadóttir et al., 2009, Figs. 3 and 4).

Extensive maps of surface fissure swarms are available for Iceland (e.g. Gudmundsson 1987; Clifton and Kattenhorn 2006; Hjartardóttir et al. 2009; Einarsson 2010; Hjartardóttir et al. 2015). Even though eruptive fissures can be used as stress indicators, surface fissure swarms do not provide information on the stress field but on the deformation (Hjartardóttir et al., 2015). The fissure swarms are very similarly oriented to the orientation of the S_{Hmax}. Especially in the NVZ the orientation of the fissure swarms are well in agreement with eruptive fissures and other stress indicators (e.g. Hjartardóttir et al., 2015).

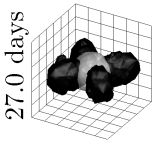

3.5 Conclusion

In this paper we present the first comprehensive and quality ranked compilation of the contemporary stress data in Iceland including the analysis of image logs from 57 geothermal boreholes. In total we compiled 495 S_{Hmax} orientations from different stress indicators. The main contributions to the newly compiled database are from 171 surface geological information, 61 geothermal wells (intermediate-depth), and 175 indicators from focal mechanism solutions of earthquakes (deep). The two key findings of this compilation are: (1) no significant depth-dependent variation in the S_{Hmax} orientation ($\pm 25\,^{\circ}$) is observed while the stress regime changes with depth. (2) four distinct contemporary stress provinces are present in Iceland. The stress provinces are in agreement with the large-scale regional tectonic setting.

Acknowledgement

The authors would like to thank Romain Plateaux and two anonymous reviewers for their comments which significantly improved the manuscript. Furthermore the authors would like to thank Orkuveita Reykjavíkur, RARIK, Norðurorka, Landsvirkjun, HS Orka, and Skagafjarðarveitur for the permission to publish the televiewer data. The research leading to these results has received funding from the European Community's Seventh Framework Programme under grant agreement No. 608553 (Project IMAGE). With respect to this we like to thank David Bruhn and Ólafur G. Flóvenz. The maps are generated with CASMI (Heidbach and Höhne, 2008) and GMT (Wessel et al., 2013) with topographic data from ETOPO1 (Amante and Eakins, 2009) and bathymetric data from the GEBCO_2014 Grid, www.gebco.net. We also would like to thank Kristján Sæmundsson and Maryam Khodayar who read the manuscript as well as John Reinecker and Sebastian Specht for their support in technical issues. Mojtaba Rajabi's contribution forms TRaX record #344.

Supplementary Data

A spreadsheet file of the Iceland stress database is provided in the supplementary data section on page VII.

4 A Multi-Stage 3D Stress Field Modelling Approach Exemplified in the Bavarian Molasse Basin

Moritz O. Ziegler[1,2], Oliver Heidbach[1], John Reinecker[3], Anna M. Przybycin[4], Magdalena Scheck-Wenderoth[1,5]

[1] Helmholtz Centre Potsdam, German Research Centre for Geosciences, Telegrafenberg, 14473 Potsdam, Germany

[2] University of Potsdam, Institute of Earth and Environmental Science, Karl-Liebknecht-Str. 24-25, 14476 Potsdam-Golm, Germany

[3] GeoThermal Engineering GmbH, Baischstrasse 8, 76133 Karlsruhe, Germany

[4] Bundesanstalt für Gewässerkunde, Am Mainzer Tor 1, 56068 Koblenz, Germany

[5] RWTH Aachen University, Department of Geology, Geochemistry of Petroleum and Coal, Templergraben 55, 52056 Aachen, Germany

Journal: Solid Earth, 2016, Vol. 7, p. 1365–1382, doi: 10.5194/se-7-1365-2016

Received 21 June 2016, Revised 1 September 2016, Accepted 6 September 2016, Published 21 September 2016

Abstract

The knowledge of the contemporary in-situ stress state is a key issue for safe and sustainable subsurface engineering. However, information on the orientation and magnitudes of the stress state is limited and often not available for the areas of interest. Therefore 3D geomechanical-numerical modelling is used to estimate the in-situ stress state and the distance of faults from failure for application in subsurface engineering. The main challenge in this approach is to bridge the gap in scale between the widely scattered data used for calibration of the model and the high resolution in the target area required for the application. We present a multi-stage 3D geomechanical-numerical approach which provides a state-of-the-art model of the stress field for a reservoir-scale area from widely scattered data records. Therefore, we first use a large-scale regional model which is calibrated by available stress data and provides the full 3D stress tensor at discrete points in the entire model volume. The modelled stress state is used subsequently for the calibration of a smaller-scale model located within the large-scale model in an area without any observed stress data records. We exemplify this approach with two stages for the area around Munich

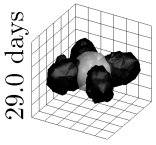

in the German Molasse Basin. As an example of application, we estimate the scalar values for slip tendency and fracture potential from the model results as measures for the criticality of fault reactivation in the reservoir-scale model. The modelling results show that variations due to uncertainties in the input data are mainly introduced by the uncertain material properties and missing S_{Hmax} magnitude estimates needed for a more reliable model calibration. This leads to the conclusion that at this stage the model's reliability depends only on the amount and quality of available stress information rather than on the modelling technique itself or on local details of the model geometry. Any improvements in modelling and increases in model reliability can only be achieved using more high-quality data for calibration.

4.1 Introduction

The contemporary in-situ upper crustal stress field is of key importance for our understanding of geodynamic processes such as natural and induced seismicity (Häring et al., 2008; Gaucher et al., 2015; Scholz, 2002; Heidbach and Ben-Avraham, 2007; Townend and Zoback, 2004; Zang et al., 2014). The stress field also provides critical a priori information for safe and sustainable underground engineering such as wellbore planning and stability, reservoir management, tunnelling, mining, and underground waste storage (Altmann et al., 2014; Cornet et al., 1997; Fuchs and Müller, 2001; Moeck and Backers, 2011; Tingay et al., 2008; Zang et al., 2013; Ziegler et al., 2015; Zoback, 2010). The quantification of the criticality of the in-situ stress state in terms of fault reactivation in advance of any underground treatment is essential for identifying areas of low criticality for safe and efficient utilization of the subsurface (Hornbach et al., 2015; Zoback et al., 1985; Häring et al., 2008; Kohl and Mégel, 2007). In particular, the enhancement of permeability through hydraulic fracturing should be achieved without reactivation of sealing faults or inducing seismic events of economic concern (Deichmann and Ernst, 2009; Yoon et al., 2015a; Zoback et al., 1985; Townend and Zoback, 2000). The main focus of current research is to quantify stress changes due to anthropogenic underground usage (McClure and Horne, 2014a; Jeanne et al., 2014; Orlecka-Sikora, 2010; Gaucher et al., 2015; Magri et al., 2013). Induced changes of the 3D stress state in georeservoirs are simulated with thermo-hydro-mechanical (THM) models since the treatment of the underground, e.g. the rate of injected fluid or the amount of mass removal, is well known (Kohl and Mégel, 2007; Gaucher et al., 2015; Van Wees et al., 2014; Jeanne et al., 2014; Cacace et al., 2013; Rutqvist et al., 2013; Magri et al., 2013). However, to assess whether the subsurface engineering pushes the system into a critical stress state in terms of absolute values, knowledge of the contemporary in-situ stress, i.e. the undisturbed stress state, is essential (Hergert et al., 2015; Häring et al., 2008).

The 3D in-situ stress state can be described with a symmetric tensor of second degree with six independent components (Jaeger et al., 2007; Zang and Stephansson, 2010). Assuming that the vertical stress S_v is one of the principal stresses in the upper crust, the number of independent unknowns reduces to four (Zoback, 2010). In the principal axis system these are the orientation of one of the two principal horizontal stresses, i.e. the maximum and minimum horizontal stress, S_{Hmax} and S_{hmin}, as well as the magnitudes S_v, S_{Hmax} and S_{hmin} (Zoback, 2010; Schmitt et al., 2012). Thus, the orientation of this so-called reduced-stress tensor is described by the S_{Hmax} orientation, which is systematically compiled by the World Stress Map (WSM) project (Heidbach et al., 2010, 2008; Sperner et al., 2003; Zoback, 1992).

Figure 4.1 shows a stress map with a typical density of S_{Hmax} orientation data records with 172 reliable data records for the 82 000 km^2 large part of the Alpine Foreland Molasse (Reiter et al., 2015; Reinecker et al., 2010; Heidbach and Reinecker, 2013). This results in an average data density of 0.21 data records per 100 km^2, which is the typical claim size for exploration. In general, the orientation of the stress field does not change with depth in the upper crust (Rajabi et al., 2016b; Pierdominici and

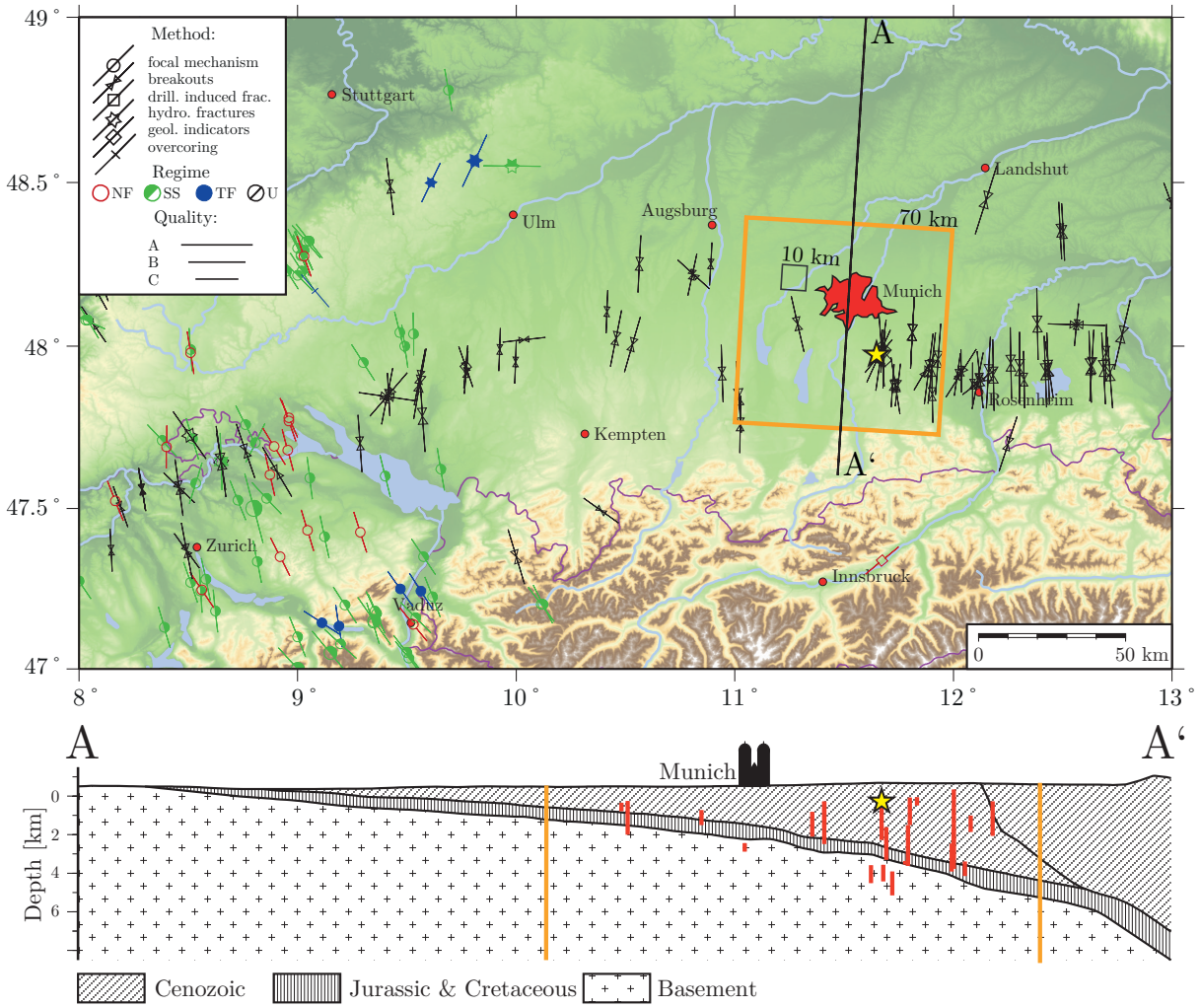

Figure 4.1: Stress map of the Bavarian Molasse with 172 A-C quality data records based on the World Stress Map database release 2008 (Heidbach et al., 2008, 2010) and additional data from Reiter et al. (2015) and Heidbach and Reinecker (2013). Lines show the S_{Hmax} orientation with line length proportional to WSM data quality (Heidbach et al., 2010). Colour coding of the data shows the stress regime with red for normal faulting (NF), green for strike-slip (SS), blue for thrust faulting (TF), and black if the regime is unknown (U). The star marks the location of the Sauerlach project where information on the S_{hmin} magnitude is available (Seithel et al., 2015). The orange box shows the lateral boundaries of the 3D geomechanical-numerical model area ($70 \times 70\,km^2$) and the small black box indicates the typical dimensions of a reservoir model ($10 \times 10\,km^2$). The cross section A-A' (based on Przybycin, 2015) shows a 1 : 2.5 exaggeration of the area with red lines being the borehole sections and stress indicators within the model area.

Heidbach, 2012; Heidbach et al., 2007). Laterally the stress field in the Alpine Molasse rotates only gently anticlockwise from east to west (Reinecker et al., 2010). Thus, the available stress orientation data allows the determination of the orientation of the reduced-stress tensor to a relatively high degree of reliability (Heidbach et al., 2007; Ziegler et al., 2016a; Reiter et al., 2015).

More important for assessing criticality is the estimation of the differential stress between the magnitudes of the largest and smallest principal stresses and their changes during stimulation and production. The S_v magnitude can be derived from the vertical-density distribution. In contrast to this, the horizontal stress magnitudes originate from geological history and ongoing tectonic evolution and cannot be determined directly from rock properties (Brown and Hoek, 1978; Zang et al., 2012; Zang and Stephansson,

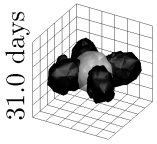

2010). Furthermore, the increase of horizontal stress magnitude with depth is often described with a linear gradient, which is only justified when rock strength and density do not change significantly with depth (Brudy et al., 1997; Lund and Zoback, 1999). In sedimentary basins this linear increase cannot always be assumed. Competent layers, e.g. from the Malm and Muschelkalk, alternate with weaker layers with high clay content such as Dogger and Keuper and result in a sudden deviation of the stresses from a linear trend across these layers (Warpinski, 1989; Hergert et al., 2015; Cornet and Röckel, 2012; Gunzburger and Cornet, 2007; Zang et al., 2012). Moreover, the density of stress magnitude data records is, in general, up to 2 magnitudes lower than that of the orientation data (Fig. 4.1).

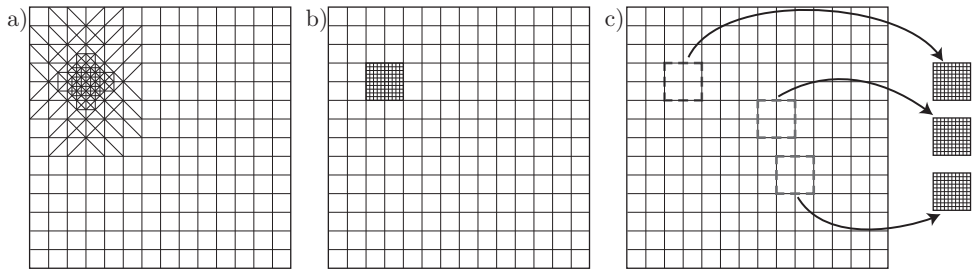

Figure 4.2: Different types of modelling approaches. (a) A refined mesh in the area of interest is expensive and inefficient due to the large number of elements required for the discretization of the gradient in resolution. Furthermore, it requires a complete remesh and re-evaluation in case of any change in the geometry or input data. (b) A local model nested within a regional model matches the variables at the boundary. A complete remesh and re-evaluation is required in case of geometry or input data changes. (c) A multi-stage approach has the easiest mesh generation since the differently sized models are generated independently. Furthermore, several reservoir models can be based on the same regional model.

To summarize, our knowledge of the 3D in-situ stress state is based on sparsely distributed and incomplete information. Only the orientation of the reduced-stress tensor and, to a lesser extent, information about the stress regime are relatively well estimated from stress indicators. The crustal in-situ stress magnitudes are underdetermined, since they vary laterally and vertically. To determine the full stress tensor for every point in a volume, a 3D geomechanical-numerical model workflow that uses the available stress information for model-independent constraints for calibration is essential. Moreover, at reservoir scale, often no stress information is available for model calibration (Fig. 4.1). Thus, it is necessary to enlarge the model area until sufficient stress data are within the model volume. In the Bavarian Molasse Basin, which we use as an example, this enlargement of the model area leads to an increase in model size from a $10 \times 10\,\mathrm{km}^2$ reservoir-sized model to $70 \times 70\,\mathrm{km}^2$ regional model (Fig. 4.1). Considering a constant resolution, this enlargement would lead to a higher number of model degrees of freedom by a factor of 50. In most cases of THM reservoir modelling, this is beyond feasibility due to the time required for iterations and limitations in computation power. One option for avoiding a high degree of freedom is to refine the structure only in the area of interest (Jeanne et al., 2014; Westerhaus et al., 2008) (Fig. 4.2a). However, this becomes challenging when local structures have to be integrated. An alternative option is to use nested modelling, which is applied in various scientific disciplines such as meteorology, climate simulations, and the simulation of seismic cycles (Warner and Hsu, 2000; Cacas et al., 2001; Giorgi et al., 1998; Hergert and Heidbach, 2011). Essentially, a nested modelling approach can be (1) a local high-resolution grid inside a coarse grid where the variables are matched at the boundaries (Fig. 4.2b) (Oey and Chen, 1992) or (2) a multi-stage approach of two or more individual models which increase their resolution within the same area or subarea (Warner and Hsu, 2000) (Fig. 4.2c). In contrast to the previously named nested approaches, the multi-stage procedure is most favourable in terms of required workload

(fast and simple mesh generation) and quality of results (high spatial resolution in the area of interest). Furthermore, it may serve several individual reservoir model locations within the regional-area model volume (Fig. 4.2c). However, so far this procedure has not been applied in 3D geomechanical-numerical modelling of the crustal stress field.

In this paper we demonstrate the applicability of the multi-stage nesting workflow for the 3D geomechanical modelling of the stress tensor. We exemplify our approach with a 3D model of the Greater Munich area in the northern Alpine Molasse Basin and a generic reservoir model (Fig. 4.1). We demonstrate the conceptual advantages of the multi-stage approach as a detailed, yet fast workflow for exploration from planning to exploitation. Furthermore, we quantify the impact of the uncertainties of the model parameters and the limited amount of calibration data on the model results and discuss the reliability of the 3D geomechanical-numerical modelling.

4.2 Geological Setting

The northern Alpine Molasse Basin is a typical asymmetric foreland basin which extends over 1000 km from Lake Geneva in the west to Lower Austria in the east (Bachmann et al., 1987). Its widest N–S extent is 130 km in southern Germany (Lemcke, 1988). The basin mainly consists of Tertiary sediments on top of Mesozoic successions and a Variscan basement with Permo-Carboniferous troughs (Lemcke, 1988; Bachmann et al., 1987). In the Foreland Molasse these sediments dip towards the south where a maximum thickness of approximately 6000 m is reached in front of and beneath the Alpine mountain chain and the Folded Molasse (Fig. 4.1) (Bachmann et al., 1987). Due to the Molasse Basin's close link to the Alpine orogeny (Schmid et al., 2008) most of the main faults in the Bavarian Foreland Molasse are steeply dipping ($> 60\,^{\circ}$) and strike at least subparallel to the Alpine front approximately E–W (Reinecker et al., 2010; Bachmann et al., 1987; Lemcke, 1988). They are considered mostly inactive at the moment (Reinecker et al., 2010; Bachmann et al., 1987; Lemcke, 1988).

For our model geometry we use the upper 9 km of the 3D structural model of the northern Alpine Foreland Basin by Przybycin (2015), which covers the entire German part of the Molasse Basin. It provides 12 stratigraphical units in total with a focus on the Malm and Purbeck, two target horizons for geothermal exploration (Lemcke, 1988; Bachmann et al., 1982; Fritzer et al., 2012). The lateral resolution of the structural model ($1 \times 1.7\,\mathrm{km}^2$) is sufficient to provide the geometry for the generation of our regional-scale model of the Greater Munich area. The structure is based on freely available data on the depth and thicknesses of stratigraphic units from wells and seismic lines as well as 3D gravity modelling as a further constraint (Przybycin, 2015). The part of the structural model used for the geomechanical model has a size of $70 \times 70\,\mathrm{km}^2$ and is referred to as the root model. It includes the sediments in the Molasse Basin in their entire vertical extent. The bottom of the model is situated at a depth of 9 km entirely within the upper crust. The generic reservoir model located within the root model volume is called a branch model. It has a size of $10 \times 10\,\mathrm{km}^2$ with more detailed structural information, e.g. provided by a 3D seismic survey.

4.3 In-Situ Stress Data

4.3.1 Orientation of S_{Hmax}

Within the root model area (Fig. 4.1, orange box) 18 reliable S_{Hmax} orientation data records are located, while there are none in the branch model area (Fig. 4.1, black box). These data are exclusively from

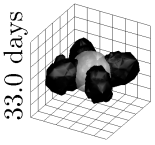

Table 4.1: The stratigraphic units, their discretization, and according rock properties, which are present in the root and branch models. Units which are only preserved in parts of the root model are marked with *.

Unit(s)	Root model: vertical layers	Branch model: number of elements	Density [kg m^{-3}]	E-module [GPa]	Poisson ratio
Molasse	6	-	2375[a,b]	15[c]	0.29[c]
Upper Molasse	-	1.1×10^6	2375[a,b]	15[c]	0.29[c]
Aquitanian	-	2.3×10^6	2495[d]	32.5[d]	0.21[d]
Chattian	-	7.6×10^6	2758[e]	39[d]	0.23[d]
Cretaceous	3*	-	2647[a,b]	22.5[b]	0.25[b]
Malm δ – Purbeck	8	6.3×10^6	2667[d,e]	40[b]	0.25[b]
Malm $\alpha - \gamma$	6	2.2×10^6	2460[d]	30[b,c]	0.29[b,c]
Pre-Malm	4*	-	2680[a,b]	20[c]	0.25[c]
Crust	6	2.2×10^6	2850[a]	45[c]	0.24[c]

[a] Przybycin (2015), [b] Koch (2009), [c] Hergert et al. (2015), [d] Lama and Vutukuri (1978), [e] Koch and Clauser (2006)

borehole measurements using drilling-induced tensile fractures (Aadnoy, 1990) and borehole breakouts (Bell and Gough, 1979; Bell, 1996) as indicators for the S_{Hmax} orientation (Reinecker et al., 2010). In 15 wells in the model area, borehole breakouts are found with a combined length of 7.7 km. In three wells drilling-induced fractures are found with a combined length of 0.3 km. The stress indicators are found mainly between the surface and a depth of 2–3 km even though some are located at greater depth (Fig. 4.1). No significant stress rotation or perturbation with depth is observed in the available data (Reinecker et al., 2010; Heidbach et al., 2016b). The quality of the data is exceptionally good according to the WSM quality ranking (Heidbach et al., 2010; Sperner et al., 2003; Zoback, 1992) with eight A-quality data records (i.e. an uncertainty of ±15 °), six B-quality data records (±15–20 °), and four C-quality data records (±20–25 °). Under the assumption that S_v is a principal stress component, the reduced 3D stress tensor within the model area has a mean S_{Hmax} orientation of $1.7° \pm 19.2°$ which is approximately perpendicular to the Alpine front (Fig. 4.1).

4.3.2 Stress Magnitudes

The magnitude of S_v can be estimated with a relatively high reliability from the thickness of the different overlying units (z) in the structural model provided by Przybycin (2015), the density of the corresponding rock material (ρ_{rock}, Tab. 4.1) and the gravitational acceleration (g) given by

$$S_v = \sigma_{zz} = \rho_{rock} g z. \tag{4.1}$$

However, information on the horizontal stress magnitudes is sparse even within the root model area. The magnitude of S_{hmin} is usually derived from hydraulic fracturing (Haimson and Fairhurst, 1969; Hubbert and Willis, 1972), but such data are not available publicly for the Bavarian Molasse Basin. Alternatively, leak-off tests (LOTs), which rely on a cheaper and faster method, are more frequently used for the estimation of S_{hmin}. They provide information on the break-down pressure of the tested

formation, which is then used as an approximation for the S_{hmin} magnitude (Haimson and Fairhurst, 1969; Bell, 1990; Zang et al., 2012). Further information on the S_{hmin} magnitude can be derived from a formation integrity test (FIT). It does not fracture the rock but provides a minimum pressure value at which the rock is stable, which in turn provides a lower bound for the S_{hmin} magnitude (Zoback et al., 2003). Even though no hydraulic fracturing was done in the model area a LOT has been conducted in the Unterhaching Gt 1/1a borehole which is used for calibration (T. Fritzer, personal communication, 2016). Furthermore, several FITs have been performed in the borehole Sauerlach (Fig. 4.1) that is in the root model area (Seithel et al., 2015). In contrast to the LOTs FITs are not used for calibration since the difference between the FIT pressure and the actual magnitude of S_{hmin} is not known. However, during one of the FITs in the Sauerlach borehole bore fluid was lost into the formation (T. Fritzer, personal communication, 2016). Hence a leak-off occurred and this FIT is treated as a LOT and used for the model calibration.

The direct estimation of the S_{Hmax} magnitude would only be possible with overcoring measurements (Hast, 1969; Sjöberg et al., 2003). In addition, reasonable values for the S_{Hmax} magnitude can be derived on the basis of the frictional equilibrium theory (Zoback et al., 2003) or physics-based relations for which reliability is largely dependent on the quality of the S_{hmin} magnitude estimation (Zoback, 2010; Cornet, 2015). Seithel et al. (2015) use the friction equilibrium approach and derive a single S_{Hmax} magnitude between 112 and 116 MPa at a depth of 4 km. We use an S_{Hmax} magnitude of 112 MPa in Sauerlach for the calibration even though the uncertainties introduced by the derivation are high. The impact of these high uncertainties on the model results is discussed later on.

4.3.3 Stress Regime

In areas with a low number of magnitude stress data records, the stress regime provides information on the relative magnitudes of S_v, S_{Hmax}, and S_{hmin}. The stress regime is mainly derived from focal mechanisms of seismic events and, to a small extent, from geological indicators or hydraulic fracturing experiments (Zoback, 1992; Sperner et al., 2003). In the Swiss part of the northern Alpine Molasse Basin a strike-slip ($S_{Hmax} > S_v > S_{hmin}$) and, to a smaller extent, extensional ($S_v > S_{Hmax} > S_{hmin}$) stress regime is mainly observed (Heidbach and Reinecker, 2013). However, in the Bavarian Molasse Basin north of the Alpine front, no natural seismicity has been recorded (Grünthal, 2011; Grünthal and Wahlström, 2012) to derive the stress regime from focal mechanisms.

Information from structural geology observing steeply dipping faults in the Bavarian Molasse Basin (Bachmann et al., 1987; Lemcke, 1988) indicates an extensional tectonic faulting regime (Anderson, 1905, 1951). In contrast to this Illies and Greiner (1978); Lemcke (1988), and Reinecker et al. (2010) propose a compressional ($S_{Hmax} > S_{hmin} > S_v$) or strike-slip stress regime in the Molasse Basin. Seithel et al. (2015) also propose a strike-slip stress regime at a depth of 4 km for the Sauerlach project according to their analysis based on the frictional equilibrium theory. However, without further estimations of the stress magnitudes in other depth sections and locations, the regional tectonic stress regime setting is subject to large uncertainties.

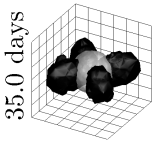

4.4 Model Workflow

4.4.1 Model Set-up

Both the regional-scale root model and the reservoir-scale branch model are based on the same modelling assumptions. Assuming that accelerations other than gravity can be neglected, the models solve the partial differential equation of the equilibrium of forces. Furthermore, we assume a linear elastic rheology and solve for absolute stresses (no pore pressure). The general model procedure follows the technical workflow explained in detail by Hergert et al. (2015) and Reiter and Heidbach (2014).

The root model extends $70 \times 70 \times 10\,\mathrm{km}^3$ in the entire Greater Munich area (Fig. 4.1). It consists of six different stratigraphic layers (Tab. 4.1) based on the 3D structural model by Przybycin (2015). The generic branch model of a potential geothermal site has a size of $10 \times 10 \times 10\,\mathrm{km}^3$ and includes six different stratigraphic units (Tab. 4.1). For both models the boundaries are oriented perpendicular and parallel to the orientation of S_{Hmax} and S_{hmin} respectively (Fig. 4.1). Both models are populated with the Young's modulus, the Poisson ratio and the density according to the stratigraphic units (Tab. 4.1).

An exact fit of the overburden S_v is achieved by applying gravity, provided that the density of the stratigraphic units is correctly chosen. We implement an equilibrated initial stress state close to lithostatic ($S_{Hmax} \approx S_{hmin} \approx S_v$). Dirichlet boundary conditions (i.e. displacements) are applied to the sidewalls of the model to create horizontal differential stresses. The boundary conditions are adjusted in a way that the modelled magnitude of S_{Hmax} and S_{hmin} at the calibration points fit the observed magnitudes.

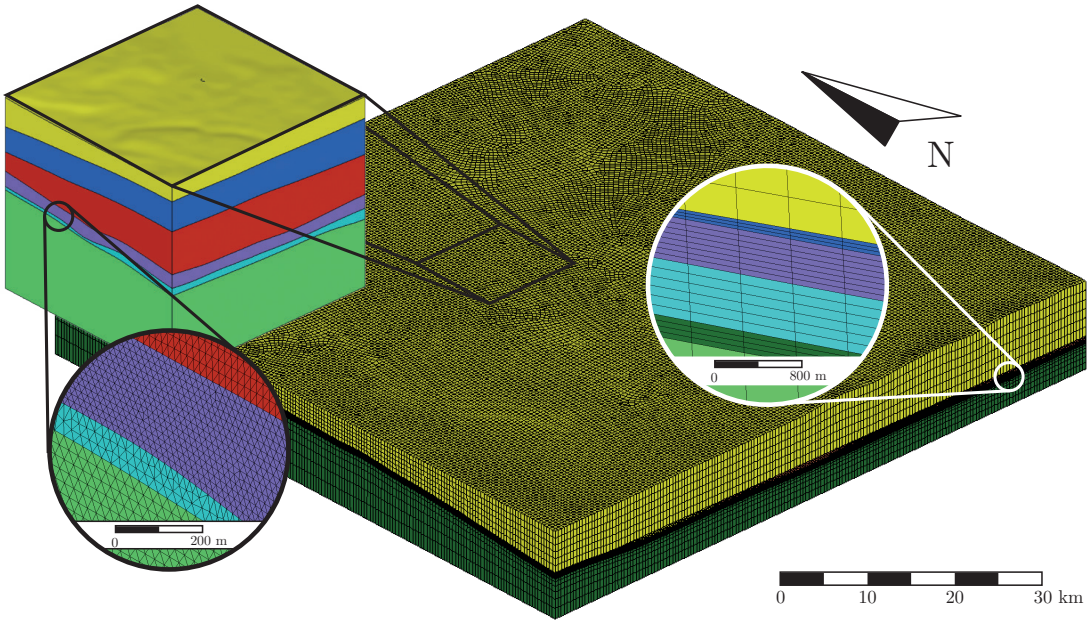

Figure 4.3: The root and branch model discretized with 10^6 hexahedral and 21×10^6 tetrahedral elements respectively. Please note that to improve visibility the discretization of the branch model is only displayed within the magnified inset. Both magnified regions show the Malm $\alpha - \gamma$ (turquoise) and Malm $\delta - \zeta$ and Purbeck (purple) units, which are the predominant target units for geothermal exploration in the Bavarian Molasse Basin.

Due to the complex topology of the stratigraphy and inhomogeneous rock properties of the different units the finite element method (FEM) that allows unstructured meshes is used to solve the partial differential equation of the equilibrium of forces at discrete points. Thus, both models are discretized

into finite element meshes. The root model is constructed with approximately 10^6 hexahedral elements resulting in approximately 400 m of horizontal and between 15 and 700 m of vertical resolution (Fig. 4.3). A vertically refined resolution is created in the units of interest for geothermal exploration, namely the Malm and Purbeck formation. The Cretaceous and the Triassic (pre-Malm) are only preserved in parts of the root model. Compared to the root model a significantly finer resolution with a total of 21×10^6 tetrahedral elements is chosen in the branch model. The edge length of the elements varies between 10 and 160 m with the coarsest resolution located at the bottom and the edges of the model and the highest resolution in the Purbeck and Malm units of interest for geothermal exploration (Fig. 4.3).

4.4.2 Model Calibration Procedure and Two-Stage Approach

The calibration of the root model with stress magnitude data is achieved by applying two Dirichlet boundary conditions, each on one of the perpendicular sidewalls of the model (Fig. 4.4, left row). A single S_{hmin} magnitude data record can be exactly modelled by a certain combination of two boundary conditions. More precisely an unlimited combination of two boundary conditions exist to achieve an exact fit of a single S_{hmin} magnitude calibration point. This unlimited number of combinations of displacement boundary conditions is a linear function of the E–W and N–S displacements and is displayed as a linear slope in Figure 4.4a with displacement in N–S direction on the x-axis and displacement in E–W direction on the y-axis. Due to the assumed linear elastic model rheology, each combination of East–West and North–South displacement that lies on the slope leads to an exactly calibrated model (Fig. 4.4a).

If several S_{hmin} magnitudes are available for calibration, each of them can be exactly reproduced by an unlimited number of combinations of displacement boundary conditions. However, to achieve a calibration which works for all of the observed S_{hmin} magnitudes, a single "best-fit" slope is derived from the linear slopes for the individual calibration points using a linear regression (Fig. 4.4b) (Reiter and Heidbach, 2014). Each combination of displacement boundary conditions specified by this slope results in a best-fit model for all of the considered calibration points.

The same procedure is applied for the calibration of S_{Hmax} magnitudes so that eventually a best-fit slope for both the S_{Hmax} and S_{hmin} magnitude stress data records used for calibration are available (Fig. 4.4c). Displacement boundary conditions defined by the point where these two best-fit slopes intersect are used to compute the best-fit model that reproduces the S_{Hmax} and S_{hmin} stress data records best (Fig. 4.4c) (Reiter and Heidbach, 2014).

Application of this calibration procedure is fast and simple since the best-fit boundary conditions can be found by combining two linear slopes based on the calibration data and the displacement boundary conditions. Therefore, to find the best-fit boundary conditions only three different models with arbitrary displacement boundary conditions are required (Fig. 4.5a). The modelled S_{Hmax} and S_{hmin} magnitudes at the location of calibration points in each of the three models are compared to the actually observed data records (Fig. 4.5b, c). A linear regression with two unknown variables leads to the best-fit slopes for the combination of boundary conditions to model the S_{Hmax} and S_{hmin} magnitude (Fig. 4.5d). At the intersection of the two slopes, the boundary conditions for the best-fit model can be derived (Fig. 4.5d).

It is assumed that the stress data records used for the calibration are the result of the far-field stress state and its interaction with structural features such as local density and/or strength contrasts represented within the root model. If the measurements were, e.g. the result of an unknown or unimplemented local active fault, the results of the calibration would not be reliable. Thus, in general, the data used for calibration should be representative for a large volume of the individual lithological layer.

Under this assumption the best-fit model simulates the stress state at discrete points in the entire

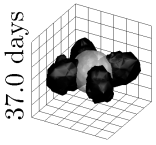

model volume. Hence, information on the stress state is now also available in areas of the root model where previously no observables on the stress state were available. This means that in the branch model, which does not include any observed stress data records, simulated information on the stress state is also now available from the root model and can be used to calibrate the branch model (Fig. 4.5d, f).

Since the branch model is calibrated in the same way as the root model (but with a simulated stress state from the root model as calibration points instead of observed stress data records), a large number of potential calibration points with S_{hmin} and S_{Hmax} magnitudes are available. The S_{Hmax} and S_{hmin} magnitudes at each calibration point can be modelled individually in the branch model by combinations of boundary conditions, each described by a linear slope (Fig. 4.4a). For all S_{Hmax} and S_{hmin} magnitudes a best-fit slope is derived, based on the individual linear slopes (Fig. 4.4b). Two best-fit slopes describe the combinations of boundary conditions which model the S_{Hmax} and S_{hmin} magnitudes best. The

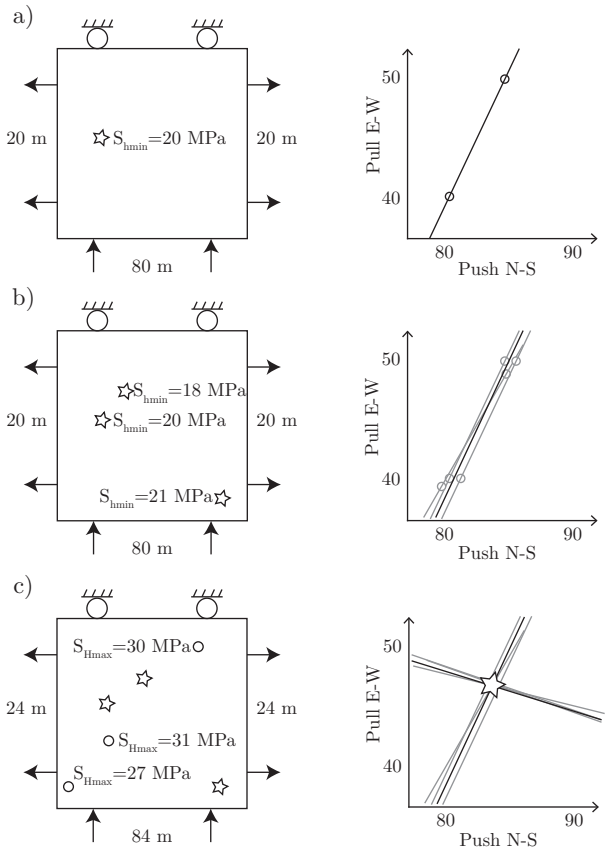

Figure 4.4: Left: exemplified schematic models with the data records used for calibration (star: S_{hmin} magnitude, circle: S_{Hmax} magnitude). Right: linear slopes that display the magnitudes of possible combinations of displacement boundary conditions applied normal to the E–W (y-axis) and N–S (x-axis) sidewalls of the model. For each data record an individual slope defines the possible combinations of boundary conditions to fit the model to this calibration data record. (a) A single S_{hmin} magnitude can be calibrated by an unlimited number of combinations of boundary conditions which are on a linear slope. (b) Several S_{hmin} magnitudes usually cannot be calibrated to an exact fit. However, a linear regression of all the linear slopes derived for the calibration of each individual data record provides a best-fit slope. This slope defines combinations of best-fit boundary conditions that fit the data records used for calibration equally well. (c) Several S_{hmin} and S_{Hmax} magnitude data records used for calibration results for each S_{hmin} and S_{Hmax} in a linear slope of combinations of best-fit boundary conditions. At the intersection of these two slopes the best-fit boundary conditions (indicated by a star) are found for the calibration of S_{Hmax} and S_{hmin} together.

intersection of these two best-fit slopes defines the boundary conditions, which are used to compute the best-fit branch model (Fig. 4.4c). This calibration procedure is performed analogously to that of the root model (Fig. 4.5e–h).

For a successful transfer of the stress state from the root to the branch model, it is critical that the stress state used for the calibration of the branch model is obtained at discrete points of the root model and not in its volume. Otherwise the stress state extracted from the root model is potentially biased due to interpolations from discrete points into the volume, which are performed by the visualization software. Since the large number of possible calibration points can be chosen arbitrarily, their locations need to be considered. We recommend using calibration points close to the border of the branch model but outside the zone prone to boundary effects. Calibration points from the root model in the centre of the branch model are a contradiction of the two-stage approach which aims at finding local stress changes due to high-resolution structural features that are only present in the branch model. Due to the lack of any other stress data in the branch model area, the calibration procedure imposes the root model's basic stress state on the branch model, which prevents such local stress perturbations. Hence, this necessary imposition should be reduced to the boundaries of the branch model that are not used for interpretation. Furthermore, the calibration points should be evenly distributed along the branch model boundary and represented in all stratigraphic units to account for different material properties. Special attention needs to be paid to units which are either only present in the root or the branch model or have a significantly different geometry or rock properties in the two models.

4.5 Model Results

In the following two sections we present the results of two model scenarios for the root model that fit equally well the observed stress data, but with different stress regimes (Fig. 4.6). For the branch model we present our results on one scenario that can be considered our best-fit model (Fig. 4.7).

4.5.1 Root Model

The best-fit root model of the stress state at discrete points in the Greater Munich area is calibrated using S_{hmin} magnitudes from the two LOTs and one S_{Hmax} magnitude described in detail in the stress data in Section 4.3.2. The best-fit model has a good fit to the two S_{hmin} calibration data points and an almost perfect fit for the single S_{Hmax} calibration point. Deviations between observed and modelled data are on average 0.4 MPa for the two S_{hmin} calibration points and 0.04 MPa for the single S_{Hmax} calibration point.

Figure 4.8 shows the best-fit model results along the Sauerlach borehole profile along with the FIT data of Seithel et al. (2015). The black line shows the vertical stress magnitude with depth, which depends only on the chosen rock density. The blue line is the S_{hmin} magnitude, which is larger than all FIT values

Figure 4.5 (following page): The calibration workflow for the root and branch model. (a) Three models with different Dirichlet boundary conditions provide stress data comparison values for a calibration with (b) observed magnitude stress data. The deviation of the modelled from the observed stress state of each of the three scenarios (c) is used in a linear regression to derive the boundary conditions to compute the best-fit root model (d). (e) Three different branch models provide stress data comparison values for a calibration with magnitude data from the best-fit root model (f). The deviation of the modelled stress state to that provided from the root model for each of the three scenarios (g) is used in a linear regression to derive the boundary conditions required to compute the best-fit branch model (h).

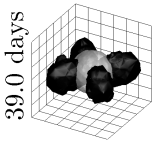

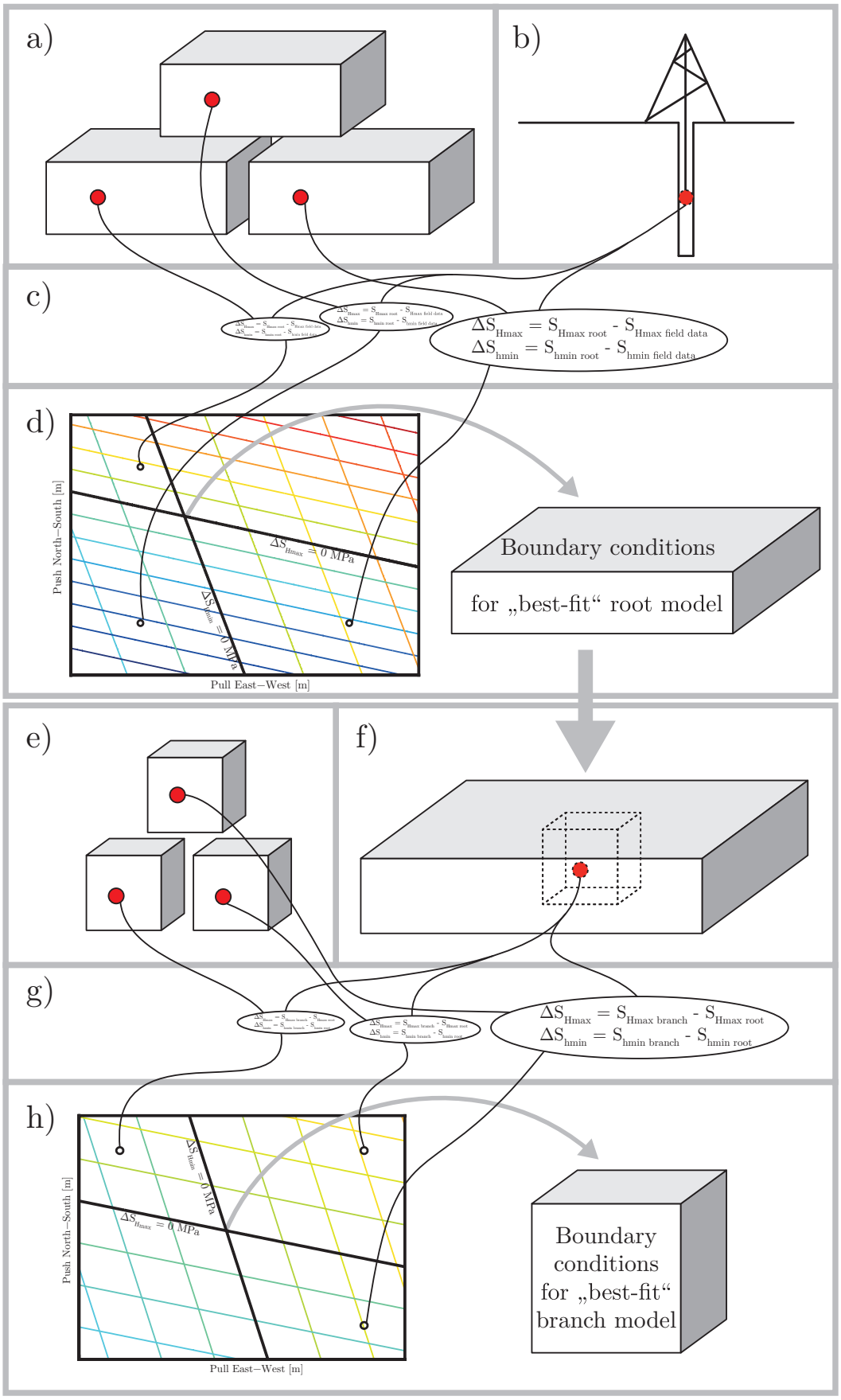
a)
b)
c)
$\Delta S_{Hmax} = S_{Hmax\ root} - S_{Hmax\ field\ data}$
$\Delta S_{hmin} = S_{hmin\ root} - S_{hmin\ field\ data}$
d)
Push North–South [m]
Pull East–West [m]
$\Delta S_{Hmax} = 0$ MPa
$\Delta S_{hmin} = 0$ MPa
Boundary conditions
for „best-fit“ root model
e)
f)
g)
$\Delta S_{Hmax} = S_{Hmax\ branch} - S_{Hmax\ root}$
$\Delta S_{hmin} = S_{hmin\ branch} - S_{hmin\ root}$
h)
Push North–South [m]
Pull East–West [m]
$\Delta S_{Hmax} = 0$ MPa
$\Delta S_{hmin} = 0$ MPa
Boundary conditions for „best-fit“ branch model

at all depth sections. The blue star represents the magnitude and depth of the S_{hmin} magnitude inferred from a FIT with leak-off. The red line is the S_{Hmax} magnitude in the best-fit model while the dashed line represents S_{Hmax} in another model scenario. The red star marks the depth and magnitude of S_{Hmax} in the best-fit model. The shaded areas show the modelled magnitudes for model scenarios, which use S_{Hmax} magnitudes between 92 and 118 MPa in a depth of 4 km below the Sauerlach site for calibration. This demonstrates that the single S_{Hmax} magnitude derived in conjunction with the ambiguity of the stress regime opens up a wide range of model scenarios which all equally well fit the S_{hmin} data. Even though a compressional regime can be excluded by the available data in Sauerlach, no indication exists of whether $S_{Hmax} > S_v$ or $S_{Hmax} < S_v$. That means that the prevalence of a normal faulting or a strike-slip stress regime is possible. To account for this variability, several different scenarios have been computed, two of which are compared in Figure 4.6. Note that the only difference between these scenarios is the S_{Hmax} magnitude value used for the root model calibration (Fig. 4.6a 96 MPa, Fig. 4.6b 112 MPa); the fit to the S_{hmin} data from the LOTs is equally good (Fig. 4.6).

In Figure 4.6 we show a number of scalar stress values derived from the modelled 3D stress tensor on cross sections and within stratigraphic units for the aforementioned two model scenarios. The figure shows that the values vary depending on the stratigraphic units horizontally and laterally. More importantly, the results from the two model scenarios which fit the model-independent calibration data equally well are quite different. The first row of Figure 4.6 shows the variability of the stress regime using a continuous scale, the so-called regime stress ratio (RSR) from Simpson (1997). Close to the surface a strike-slip regime dominates with compressional components in some areas. With increasing depths this changes to a prevailing extensional regime. Moreover, some changes from strike-slip to extensional and back to strike-slip can be observed. They are not a smooth linear trend but are highly dependent on the lithology.

The second row of Figure 4.6 displays the horizontal stress anisotropy as a stress magnitude ratio of S_{Hmax}/S_{hmin} on a N–S and E–W cross section through the two model scenarios of the root model. It is clearly visible that the ratio varies significantly with depth and between the model scenarios. The southward-dipping Malm and Purbeck units have stress ratios of up to 0.15 higher than the basement layer and overlying sediments respectively.

The last row in Figure 4.6 shows the differential stress in the middle of the Malm unit. Both model scenarios show higher differential stresses in the south where the Malm units are deeper than in the north. The largest N–S difference is 7 MPa in model scenario (a) in contrast to 12 MPa in model scenario (b), even though the relative pattern of the differential stresses in the Malm unit is quite similar in both model scenarios. This pattern highlights the main trend of an increasing differential stress towards the south. At the same time significant changes of the differential stress within less than 10 km of up to 1 MPa are predicted.

4.5.2 Branch Model

In this section we show the model results of the branch model (Fig. 4.7) that uses the stress data derived from the root model scenario displayed in the right row of Figure 4.6. In order to visualize the criticality of the reservoir, we use two scalar values which are computed from the modelled 3D stress state. The first one is the fracture potential (FP) of intact rock volume (Connolly and Cosgrove, 1999). It is computed as

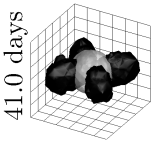

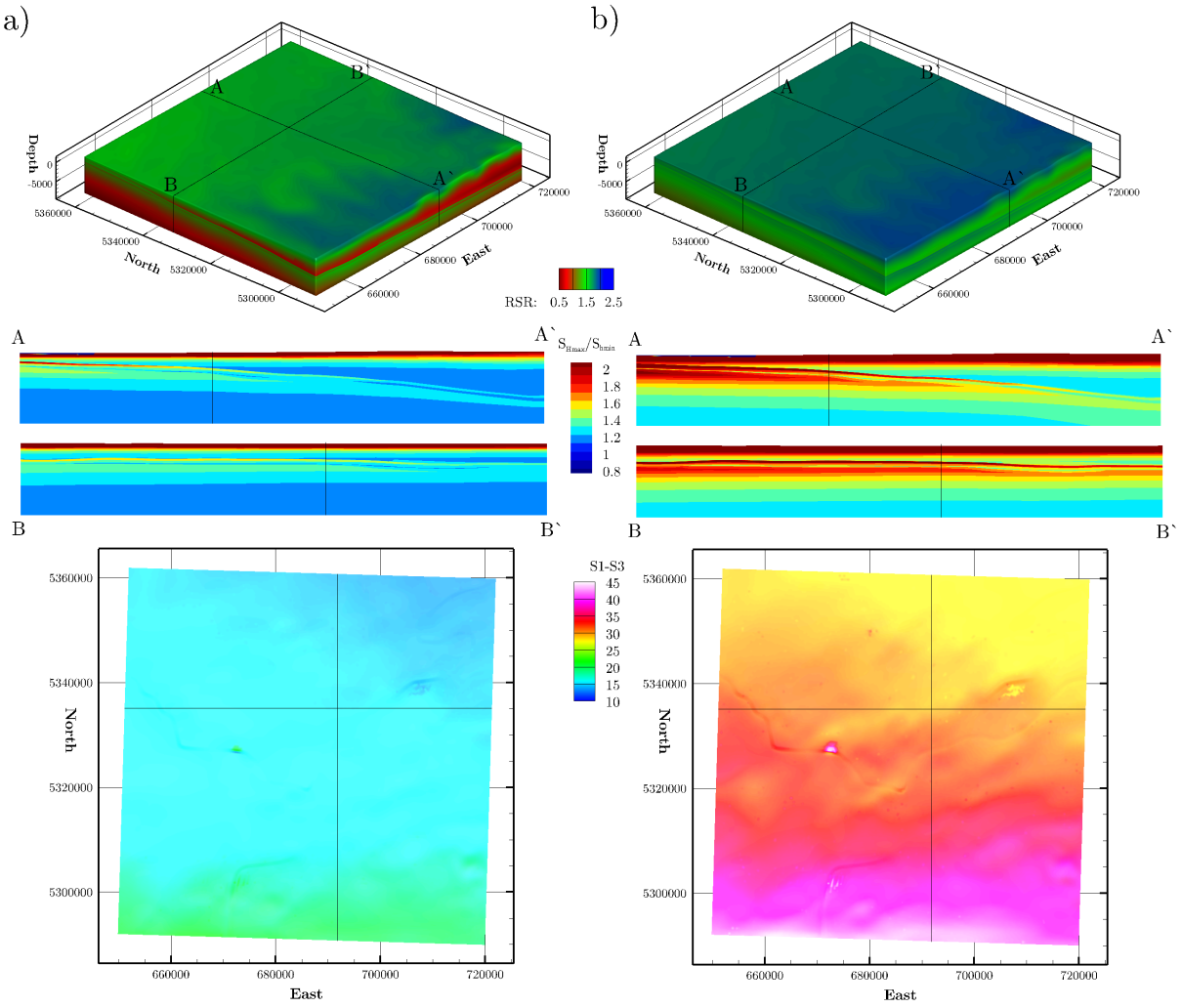

Figure 4.6: Results of the best-fit root model (b) and an alternative scenario that fits the S_{hmin} values equally well, but is calibrated against a lower S_{Hmax} value (a). The overall difference that results from the different S_{Hmax} values used for the calibration is expressed in the continuous scale of the regime stress ratio (RSR), which is between 0.5 (normal faulting regime), 1.5 (strike-slip), and 2.5 (thrust faulting regime) (Simpson, 1997) in the model volume. The horizontal stress anisotropy expressed in the ratio of S_{Hmax}/S_{hmin} is shown on two cross sections which intersect below Munich. The differential stress (difference between the maximum and minimum principal stress, lowermost panel) is mapped on a surface which is vertically centred in the Malm $\alpha - \gamma$ units.

$$\begin{aligned} \mathrm{FP} &= \frac{\text{actual maximum shear stress}}{\text{acceptable shear stress}} \\ &= \frac{0.5(S1 - S3)}{C\cos(\Phi) + 0.5(S1 + S3)\sin(\Phi)}, \end{aligned} \tag{4.2}$$

with $S1$ and $S3$ as the maximum and minimum principal stress, C as the cohesion, and Φ as the friction angle. As a second scalar value, slip tendency (ST) is computed on faults (Morris et al., 1996). It is a measure of the criticality of faults which is illustrated as a scalar value for the distance to failure derived from the stress tensor with values between 0 (safe) and 1 (failure). Slip tendency is computed for faults or fault segments of a certain orientation and is defined as

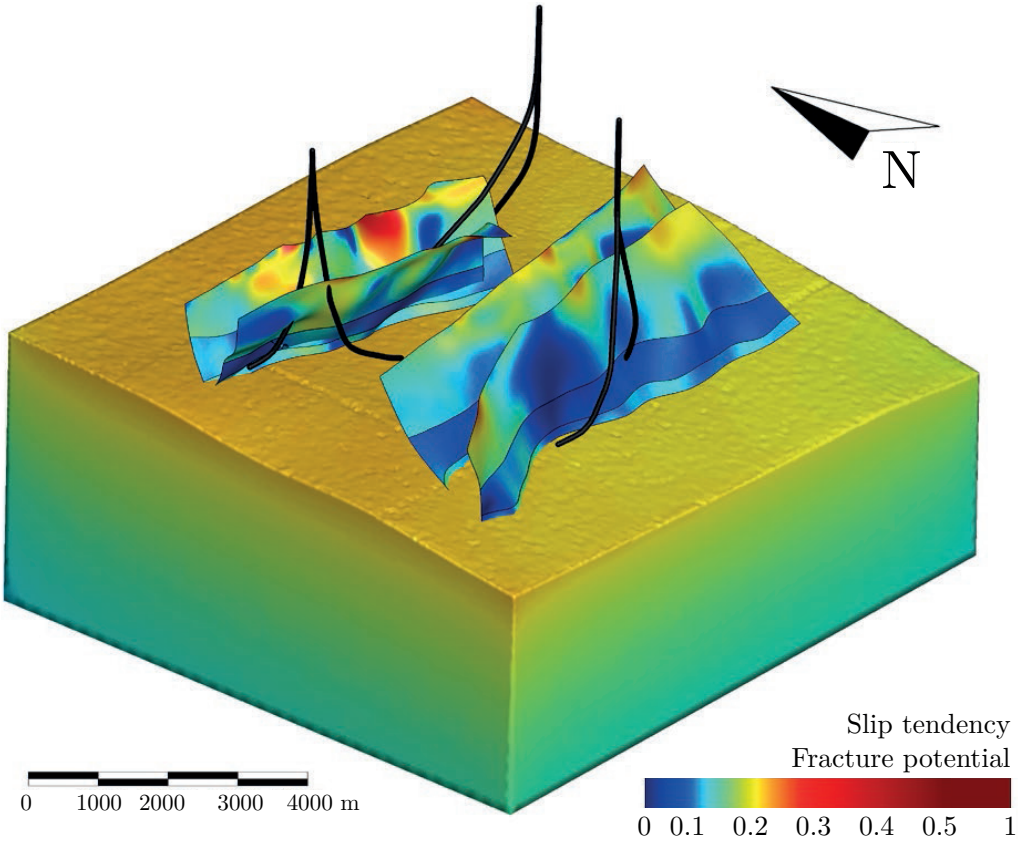

Figure 4.7: The generic branch model results are shown by means of slip tendency (ST) values (Morris et al., 1996) mapped on generic faults in the Chattian, Purbeck, and Malm units and by means of the fracture potential (FP) (Connolly and Cosgrove, 1999) displayed for the model volume of the basement. Both values vary from zero to one indicating low and high criticality. Note, that the colour map of these values is non-linear. The results clearly indicate that the generic faults are far away from failure with the largest value of ST of 0.3. The low FP values (max. 0.38) give an estimate on how much fluid pressure would be needed to fracture the intact rock in a stimulation experiment to enhance the permeability.

$$\mathrm{ST} = \frac{\tau_{\max} - C}{\sigma_n} \mu^{-1} = \frac{\tau_{\max} - C}{\sigma_n} (\tan(\Phi))^{-1}, \quad [1] \tag{4.3}$$

with the maximum shear stress $\tau_{\max}$, the normal stress σ_n, the friction angle $\Phi = \arctan(\mu)$, and the friction coefficient μ. The application of these two values is shown in the branch model with generic faults in Figure 4.7.

The high dependence of slip tendency on the orientation, friction, and cohesion of the fault is displayed in Figure 4.7. A high variability of slip tendency between 0.05 and 0.3 is observed on the generic faults. This variability is induced by the 3D stress tensor and the curved fault surfaces. Furthermore, due to differently assumed friction and cohesion of the rocks, the Malm δ – Purbeck units have a clearly smaller value of slip tendency compared to the Chattian units in the hanging wall and the Malm $\alpha - \gamma$ in the footwall. The fracture potential in the basement generally lies between 0.1 and 0.2, which is quite low, hence it requires high pressure for hydraulic fracturing operations to enhance the permeability of the fracture network.

[1] Equation 4.3 in the original manuscript erroneously reads: $\mathrm{ST} = \frac{\tau_{\max} C}{\sigma_n} \mu^{-1} = \frac{\tau_{\max} C}{\sigma_n} \tan(\Phi)^{-1}$. A corrigendum is published (Ziegler et al., 2016d).

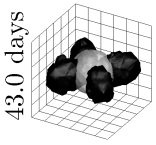

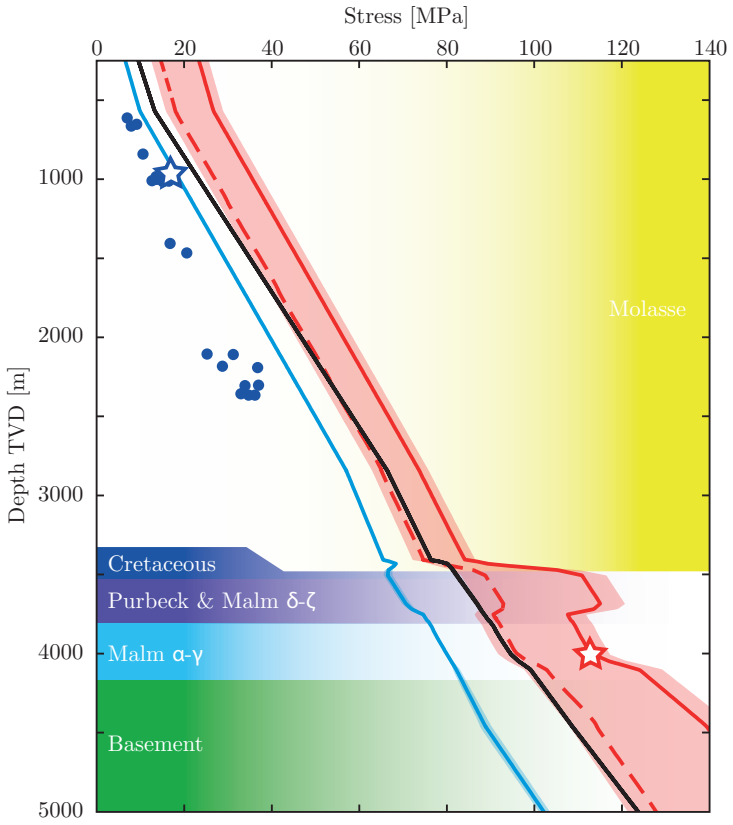

Figure 4.8: Stratigraphy and model result of the root model along the borehole of the geothermal project in Sauerlach. Lines show the results of the best-fit root model: blue for the S_{hmin} magnitude, black for the vertical stress S_v, and red for the S_{Hmax} magnitude. The blue dots are formation integrity tests (FITs), which are a lower boundary for the magnitude of S_{hmin} and not used for calibration, the blue star represents the suspected LOT, the red star shows the S_{Hmax} magnitude of 112 MPa used for calibration (Seithel et al., 2015). Shaded areas in the same colour around the lines show the range of model scenarios that fit equally well to the model-independent constraints. The dotted red line shows the S_{Hmax} magnitude for the model scenario in Figure 4.6a.

Information provided by the branch model is used in an early pre-drilling stage of a project to assess whether the initial conditions of the reservoir and its criticality allow safe production; i.e. both slip tendency and fracture potential have low values as in Figure 4.7. Before the drilling of the borehole begins the planning of the drill paths can be optimized. Especially if intersections with faults are required, their paths can be monitored and adapted in a way that they circumnavigate fault segments which have a higher value of slip tendency, meaning that this fault segment is more favourably oriented for a potential failure compared to other fault segments. In Figure 4.7 areas with cool colours are preferred for intersections of boreholes with faults compared to areas with hot colours. In Figure 4.7 the Malm δ – Purbeck unit is mostly blueish coloured which indicates the lowest slip tendency values. Hence these are the best units for the intersection of boreholes with faults. An intersection with the northernmost fault in the red areas should be avoided.

4.6 Reliability of the Model Results

One of the key points in geomechanical modelling is the reliability of the model results in terms of the predicted processes and the presented multi-stage simulation of the in-situ stress field. As already

Table 4.2: The expected maximum variations in slip tendency (ST) introduced by the uncertainties of the model parameters. This comparison is made at 40 locations in the Malm $\alpha - \gamma$ and Purbeck target units and an arithmetic mean is computed for each model parameter.

Source of uncertainty		Δ_{max} ST
Rock properties		0.18
Calibration	S_{Hmax}	0.14
	S_{hmin}	0.01
Analysis	Strike $\pm 10\,^\circ$	0.02
	Dip $\pm 10\,^\circ$	0.03
	Cohesion ± 5 MPa	0.07
	Friction angle $\pm 10\,^\circ$	0.07
Two-stage calibration		0.05
Total variations		0.57

mentioned in the result Section 4.5 the calibration procedure introduces uncertainties due to the low number of data points as well as their relatively large uncertainties. Further uncertainties are introduced by the model input, e.g. calibration data, rock properties, and structure. Hence, the reliability of the model depends on the uncertainties of the input data used for the model. To quantify the model's reliability we use the already presented scalar value slip tendency (Morris et al., 1996), for which variability is introduced by the uncertainties in different input data.

We compute the slip tendency for model scenarios which use the extreme values of the input parameters range of uncertainties. The model's linear elastic behaviour allows the individual quantification of the impact of different model parameter uncertainties on the model's reliability. Therefore we compute several model scenarios in which sequentially only a single parameter is changed to an extreme value. This enables us to derive the individual impact of different parameters and quantify the most important ones. The results of the slip tendency for each model scenario are subsequently compared to the best-fit slip tendency values from the best-fit model (Tab. 4.2). The variations of slip tendency introduced by the different independent parameters are added together, which leads to an expected maximum variability in slip tendency of ± 0.57.

The two main sources for the variability of slip tendency can be identified as the model-independent data for the S_{Hmax} magnitude used for the model calibration and the rock properties density, Young's modulus, and Poisson ratio (Tab. 4.2). A high variability of slip tendency of 0.14 is introduced by uncertainties in the S_{Hmax} magnitude. Since the S_{Hmax} magnitude is derived under several assumptions, a wide range of possible S_{Hmax} magnitudes is used for the calibration of the slip tendency model scenarios. Due to the fact that only limited knowledge and measurements of the rock properties are available a wide range of values are possible and they introduce a high variability of 0.18 in slip tendency.

Slip tendency proves to be quite robust (± 0.01) to the small uncertainties in the S_{hmin} magnitude under the assumption that the available data used for calibration is a valid proxy for the entire model (Tab. 4.2). Likewise only small variations in slip tendency are introduced by changes of $\pm 10\,^\circ$ in the fault strike (± 0.02) and dip (± 0.03). The cohesion and friction angle act as more sensitive parameters (each ± 0.07). Finally the two-stage calibration procedure itself introduces some moderate deviations (± 0.05) with a large number of calibration points and their individual locations used in the branch model.

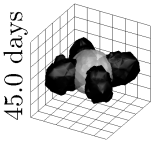

4.7 Discussion

The objective of this work was to demonstrate the multi-stage approach for a high-resolution 3D geomechanical-numerical modelling workflow assessing the criticality in reservoirs. In contrast to a single model, which includes both stress data records for calibration and high-resolution representation of a local reservoir structure, we use two models of different sizes. The regional-scale root model is calibrated on stress data records and provides the stress state for the calibration of the reservoir-scale branch model. This approach provides a cost-efficient, quick, and reliable state-of-the-art calibration of geomechanical-numerical models of the contemporary 3D in-situ stress field across scales. It is used to assess the criticality of reservoirs which can be quantified by scalar values such as slip tendency. If detailed information on the fracture behaviour of the rock are known, more elaborate fracture criteria than Mohr-Coulomb (e.g. Sulem, 2007; Zang and Stephansson, 2010) can be applied to analyse the model results. Furthermore, the approach provides the initial stress state for local application such as in THM models.

4.7.1 Workflow

A single model with the same functionality as the two models in the multi-stage approach needs to account for the required high resolution in the reservoir area and the large model extent to include data for calibration. These two requirements are not contradictory per se but prolong the process of mesh generation, e.g. by needing to harmonize a regional-scale low-resolution and local-scale high-resolution structural model in the area of overlap. Furthermore, the manageability of the model (e.g. logical size) and the available time for computation (number of elements) in most instances requires a variable resolution which is refined only in the target area. Such a change in element size in a single model is possible but the mesh generation is cumbersome and needs a high number of elements. For a THM simulation of production and (re)injection, incrementation over time significantly increases the computation time for each single element. Furthermore, in a single large model, only a very small area is of interest, hence large areas are simulated to no purpose while at the same time the logical size, computation time, and effort are increased.

If a multi-stage approach with two models is applied, each model has its own fixed resolution with no required variation in element size (Fig. 4.2c). This significantly speeds up and simplifies the process of model generation since neither the structural models need to be harmonized nor a large difference in elements size needs to be implemented. Regarding the same resolution in the target area, the time required for computation decreases, but not as much as the logical size of the models, which improves the model's manageability. A geomechanical root model can also provide the stress state for a THM branch model which helps to save computation time by focussing the time-consuming THM simulation on the actual area of interest. Calibration data records for the additionally required scalar values on the pore pressure or temperature are provided in the literature or by dedicated models, e.g. Przybycin et al. (2015).

In addition the application of two models opens further possibilities for improved and safer exploration and drilling. Structural features and stress magnitude measurements recorded during advanced exploration or even initial drillings can be implemented into the model workflow due to the simplified mesh regeneration. Even a change in the target area within the root model can be more easily implemented in the workflow since only a new branch model is required. The calibration of the root model can be updated with new stress data records as soon as they become available. Finally, a large calibrated root model may include several target areas and can be reused and applied for more than one project.

4.7.2 Calibration

The two models in the presented two-stage approach are calibrated with different Dirichlet boundary conditions applied to an initial stress state. This approach follows the modelling procedure using isotropic elastic materials described by e.g. Reiter and Heidbach (2014), Hergert et al. (2015), and Gunzburger and Magnenet (2014). Almost identical results can be achieved by the application of according orthotropic elastic material and gravity loading only (Cornet and Magnenet, 2016). For deep lithosphere and asthenosphere models elasto-plastic materials with the application of gravity but no further boundary conditions can be applied and yield similar results (Maury et al., 2014).

Our root model is calibrated with data records which display the stress state as a result of the geologic history and tectonic evolution. In the presented region the stress field is very homogeneous but in other regions significant local lateral variations exist and need to be accounted for. This can be accomplished for example by lateral variations of the material properties or faults. It is crucial to ensure that the data used for the calibration is representative for the regional material and geometry in the root model.

The branch model, however, is calibrated on the stress state simulated in the root model. Both calibration procedures are not limited in the number of calibration points and a weighting of the calibration points according to reliability can be easily realized. An extension of the two-stage approach to include three (or even more) models of different sizes is possible. Furthermore, the calibration procedure allows running several alternating models with different calibration data or differently weighted calibration points as well as variations in rock properties to quantify model-specific variations. This ability was used to quantify the reliability of the model's results. It is also useful for future attempts at statistically determining uncertainties in the model's results.

Even without any additional computations, a first-order assessment of the impact of individual data records on the model calibration can be made by assessing changes in the boundary conditions. Therefore the best-fit boundary conditions derived with and without certain data records are compared. Such a data record could be a newly performed hydraulic fracturing experiment which provides an additional S_{hmin} magnitude data record. The variation of the derived boundary conditions induced by such a new data record provides a first idea of the variation of the stress state. Although, this feature cannot be used as a replacement for computations it helps to identify whether the newly included calibration point yields a significantly different stress state which requires a reassessment of the situation or if the changes are minor and the exploration can be continued as planned.

The models showed in this work do not include any implicit faults and no strain partitioning is assumed. The calibration of a model including faults and fault-specific behaviour, e.g. strain weakening or hardening or long-term relaxation of the gauge material, is possible as well if sufficient information on the fault properties are available. However, due to the non-linearities introduced by active faults the calibration process requires a regression analysis of a higher degree, hence several more test scenarios. This is beyond the scope of this work.

4.7.3 Model Independent Reliability

Apparently the model's reliability is mainly affected by the lack and high uncertainty of S_{Hmax} magnitude data. The large influence of the S_{Hmax} magnitude is shown by two different models for viable S_{Hmax} magnitudes in Figure 4.6. A feasible method to narrow down the S_{Hmax} variability is to enhance the knowledge of the Andersonian stress regime, e.g. by gathering information on earthquake focal mechanism data (if available) or the crack orientation induced by leak-off tests or hydraulic fracturing (Haimson and Fairhurst, 1969; Hubbert and Willis, 1972; Zang and Stephansson, 2010). Such information is most likely

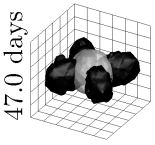

available in the model area but not publicly accessible. Furthermore, an array of many expensive deep overcoring measurements (several per borehole) could provide valuable information on the stress state and S_{Hmax} in particular (Hast, 1969; Sjöberg et al., 2003).

The uncertainties related to the material properties are another large factor that limits the model's reliability. This can be mitigated at least partly by using data from extensive databases (e.g. Bär et al., 2015; Lama and Vutukuri, 1978; Koch, 2009) or by converting seismic velocities which are founded on empirical relations (Mavko et al., 2009). Finally, averaging mean values from several laboratory tests of rock samples from the area and lithologic formations of interest are the safest but most expensive ways to retrieve reliable information of rock properties.

The uncertainties in the strike and dip of faults have a comparably small share in the reliability of the model while being challenging to mitigate due to the general uncertainties in the interpretation of 3D subsurface structures. The fault parameters cohesion and friction angle which are even more difficult to determine compared to the orientation reduce the model's reliability to a slightly higher degree compared to strike and dip. Increasing the model's reliability through a better understanding of these parameters is possible but requires a detailed understanding of the great variability of in-situ fault zone behaviour and extent at depth.

Statistical methods to quantify uncertainties in the subsurface geometry exist for purely static structural models (Wellmann, 2013; Wellmann and Regenauer-Lieb, 2012). However, the computation time required to extend this approach to a 3D geomechanical-numerical modelling approach and the ensuing analysis is beyond the scope of this work. A further investigation should be conducted as a sequel to the work by Bond et al. (2015) in a generic approach including geomechanical-numerical modelling.

4.7.4 Model Dependent Reliability

This model focusses on the stress tensor in the uppermost part of the crust and its extent is accordingly chosen. Deep-seated processes at depths larger than 9 km are, therefore, not represented in the model. However, as shown by Maury et al. (2014), the lateral variations in the differential stress in the depths are small compared to variations introduced by the uncertain material properties and magnitude of S_{Hmax} in our model. Furthermore the influence of deep structures such as the Moho geometry is minor, as shown by Reiter and Heidbach (2014) or Hergert et al. (2011).

The model does not include any faults. The inclusion of faults makes sense in situations where detailed information on fault geometry, extent, and parameters are available and a significant impact of the faults on the regional stress field or (re)activation is expected. However, in this example, the available stress data suggests that no faults with a major impact are located neither within the root model nor the branch model area. Therefore the variations introduced by omitting faults is assumed to be small.

Variations of the model results are also introduced by the multi-stage calibration approach itself and cannot be mitigated due to both models 3D stress state with lateral and vertical variations. The model's calibration, however, depends on the variations of only two independent boundary conditions. Additionally, small variations may be introduced by the model assumptions. However, these variations can be disregarded in the light of the major reasons for variations due to the small amount of stress magnitude data and rock properties. Table 4.2 clearly shows that any further advances in modelling are not efficient as long as the amount and quality of input data (S_{Hmax}, rock properties) is not increased.

4.8 Application in Geoengineering

Hydrocarbon reservoirs are currently exploited on a minor level in the Alpine Foreland (Lemcke, 1988; Sachsenhofer et al., 2006) and some of the former reservoirs are used for oil and gas storage (Sedlacek, 2009). However, hydrothermal reservoirs of economic interest for district heating or power generation are available (Lemcke, 1988; Bachmann et al., 1982; Fritzer et al., 2012). These reservoirs are situated in highly karstified limestones of the Late Jurassic which are locally referred to as Malm formations (Lemcke, 1988). As of 2016 those deep reservoirs have already been exploited by 21 municipal geothermal power plants and district heating projects of which Aschheim, Dürrnhaar, Erding, Freiham, Garching, Holzkirchen, Ismaning, Oberhaching, Poing, Riem, Sauerlach, and Unterschleißheim are in the root model area (Bundesverband Geothermie, 2016). Borehole data from these projects could be easily implemented in the calibration of the root model and would increase its reliability if they became publicly available.

Within the root model perimeter, several geothermal projects are currently at the planning stage, namely Bernried, Gräfelfing/Planegg, Königsdorf, Markt Schwaben, Puchheim/Germering, Raststätte Höhenrain, Starnberg, Weilheim/Wielenbach, and Wolfratshausen (Bundesverband Geothermie, 2016). In addition the municipal energy supplier of Munich (SWM) plans to install an extensive geothermally driven district heating grid for the entire city (Stadtwerke München GmbH, 2012). Therefore, a 3D seismic survey was conducted in the entire southern part of Munich in winter 2015/16 (Bundesverband Geothermie, 2015). The presented root model provides data for a first-order assessment of the in-situ stress state at the exact locations of these planned geothermal projects. Furthermore, it provides calibration data for local-/reservoir-scale models based on high-resolution 3D seismic surveys which simulate the stress state, its criticality, and the possibility of subsidence due to the production and reinjection of fluid and heat.

Furthermore, the two-stage approach could be extended to a three-stage approach which incorporates a global model of the entire Bavarian Molasse Basin. More data for calibration, as well as more potential applications, might be available in such an enhanced area. Thereby the regional or global root model could be established as a community model which provides the stress state for further applications and/or local models for planned projects.

4.9 Conclusions

In this work we present a multi-stage 3D geomechanical-numerical modelling approach, which provides a cost-efficient, reliable, and fast way to generate and evaluate the criticality of the stress state in a small target area where, in general, no stress data for model calibration are available. The approach uses a large-scale root model which is calibrated on available stress data and a small-scale branch model which is calibrated on the root model. We exemplify this in a two-stage approach in the German Molasse Basin around the municipality of Munich. The discussion of reliability of the model results clearly shows (1) that variations are large and (2) that they are mainly introduced by the uncertain material properties and missing S_{Hmax} magnitude data. At this stage, the model's quality depends on the amount and quality of available input data and not on the modelling technique itself. Any further improvements in the model's resolution and applied techniques will not lead to an increase in reliability. This can only be achieved by more high-quality data for calibration.

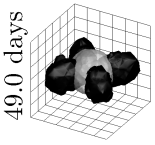

Data Availability

The stress orientation data used for model set-up and calibration is available from Reiter et al. (2016) and Heidbach et al. (2016a).

Acknowledgements

The research leading to these results has received funding from the European Community's Seventh Framework Programme under grant agreement No. 608553 (Project IMAGE). The authors would like to thank François Cornet and an anonymous reviewer for their comments which helped to clarify the manuscript, Thomas Fritzer (LFU Augsburg) for his support, Dietrich Stromeyer for discussing the procedure and the programming of the stress data analysis tool, and Arno Zang for his comments which significantly improved the manuscript. The map is prepared with the Generic Mapping Tool GMT (Wessel et al., 2013) using SRTM topographic data (Farr et al., 2007).

The article processing charges for this open-access publication were covered by a Research Centre of the Helmholtz Association.

Edited by: F. Rossetti

Reviewed by: F. H Cornet and one anonymous referee

5 Estimation of the Differential Stress from the Stress Rotation Angle in Low Permeable Rock

Moritz O. Ziegler[1,2], Oliver Heidbach[1], Arno Zang[1,2], Patricia Martínez-Garzón[1], Marco Bohnhoff[1,3]

[1] Helmholtz Centre Potsdam, German Research Centre for Geosciences, Telegrafenberg, 14473 Potsdam, Germany

[2] University of Potsdam, Institute of Earth and Environmental Science, Karl-Liebknecht-Str. 24-25, 14476 Potsdam-Golm, Germany

[3] Free University Berlin, Department of Earth Sciences, Malteser Strasse 74-100, 12249 Berlin, Germany

Journal: Geophysical Research Letters, doi: 10.1002/2017GL073598

Received 28 March 2017, Revised 2 May 2017, Accepted 4 May 2017, Available online 8 May 2017

Abstract

Rotations of the principal stress axes are observed as a result of fluid injection into reservoirs. We use a generic, fully coupled 3D thermo-hydro-mechanical model to investigate systematically the dependence of this stress rotation on different reservoir properties and injection scenarios. We find that permeability, injection rate, and initial differential stress are the key factors while other reservoir properties only play a negligible role. In particular, we find that thermal effects do not significantly contribute to stress rotations. For reservoir types with usual differential stress and reservoir treatment the occurrence of significant stress rotations is limited to reservoirs with a permeability of less than approximately $10^{-12}\,\mathrm{m}^2$. Higher permeability effectively prevents stress rotations to occur. Thus, according to these general findings the observed principal stress axes rotation can be used as a proxy of the initial differential stress provided that rock permeability and fluid injection rate are known a priori.

5.1 Introduction

Sustainable and safe subsurface engineering as well as seismic hazard assessment requires detailed information on the initial stress state (Cornet et al., 1997; Harris, 1998; Zoback, 2010; Fuchs and Müller, 2001; Heidbach and Ben-Avraham, 2007). However, widely available are only the orientation of the maximum

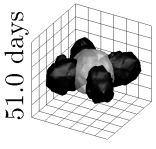

horizontal stress S_{Hmax} (Heidbach et al., 2010, 2016a; Zoback, 2010) while information on the stress magnitudes is very sparse (Zang et al., 2012). To date, the estimation of the stress magnitudes is only partly possible or economically feasible and remains a challenge (Brown and Hoek, 1978; Brudy et al., 1997; Lund and Zoback, 1999; Zang and Stephansson, 2010).

Though, the general knowledge on induced and natural subsurface processes steadily grows due to the often extensive monitoring during the exploitation of geological reservoirs, unconventional hydrocarbons among them. The recordings from local seismic networks operating with a low magnitude detection threshold and good azimuthal coverage can be used to determine focal mechanism solutions and to apply a stress inversion technique (Schoenball et al., 2014; Dorbath et al., 2009; Gritto and Jarpe, 2014). If a sufficiently high number of seismic events with focal mechanisms is available in a spatially confined area over a certain time period, advanced stress inversion techniques even allow for determining temporal variations of the stress state (Hardebeck and Michael, 2006; Martínez-Garzón et al., 2014a) or the 3D spatial distribution (Martínez-Garzón et al., 2016). Thereby temporal local rotations of the stress tensor have been observed as a physical response of the rock formation to large tectonic earthquakes (Hardebeck and Hauksson, 2001; Bohnhoff et al., 2006; Ickrath et al., 2015). Typically, these co-seismically introduced stress rotations decrease within weeks or months back to pre-mainshock orientations to a large extent (Hardebeck, 2012). More recently, systematic temporal stress rotations have also been observed in reservoirs in relation to massive fluid injection (Martínez-Garzón et al., 2013, 2014b; Schoenball et al., 2014). These stress rotations have been shown to correlate with fluid injection rates in accordance with pore pressure changes (Fig. 5.1) and reduced in-situ temperatures by the cold fluid (Jeanne et al., 2015; Yoon et al., 2015b). In addition to these local perturbations stress rotations depend mainly on the initial background stress (Sonder, 1990; Zoback, 1992). Since the local perturbations in terms of the injection rate are known and an approximate knowledge of the reservoir rock properties is usually available the initial differential stress $S1 - S3$ as the remaining unknown can be estimated.

Herein we demonstrate the feasibility of such initial differential stress estimation based on stress rotations. For this we use a generic, fully coupled 3D thermo-hydro-mechanical (THM) model that simulates the pore pressure and thermal effects of cold fluid injection into a hot reservoir. (1) In a systematic sensitivity study, we assess the reservoir properties and treatment that are needed to cause a stress rotation and quantify the resulting angle of stress rotation. (2) We then discuss the key parameters and their influence on the occurrence of stress rotations and (3) derive from our findings an approach to estimate the initial differential stress of a reservoir with known properties from observed injection induced stress rotations.

5.2 Stress Rotations

The in-situ stress state is described by the symmetric second order stress tensor with six independent components (Zoback, 2010; Jaeger et al., 2007) or using the principal axis system with the three orientations and three magnitudes of the principal stresses $S1$, $S2$, and $S3$ (Zang and Stephansson, 2010; Zoback, 2010). Isotropic changes in the stress state do not affect the orientation of these principal stress axes, but by changes in the differential stress $S1 - S3$ the orientation of the principal stress axes are potentially affected as well. This is for example the case for pore pressure changes due to reservoir depletion or injection. According to pore pressure stress coupling, the principal stresses are not equally reduced or increased by the pore pressure changes (Rudnicki, 1986; Altmann et al., 2010, 2014; Schoenball et al., 2010). This means that the principal stress changes around an injection or production well are dependent on their position relative to the wellbore (Altmann et al., 2014). Hence, the differential stresses and

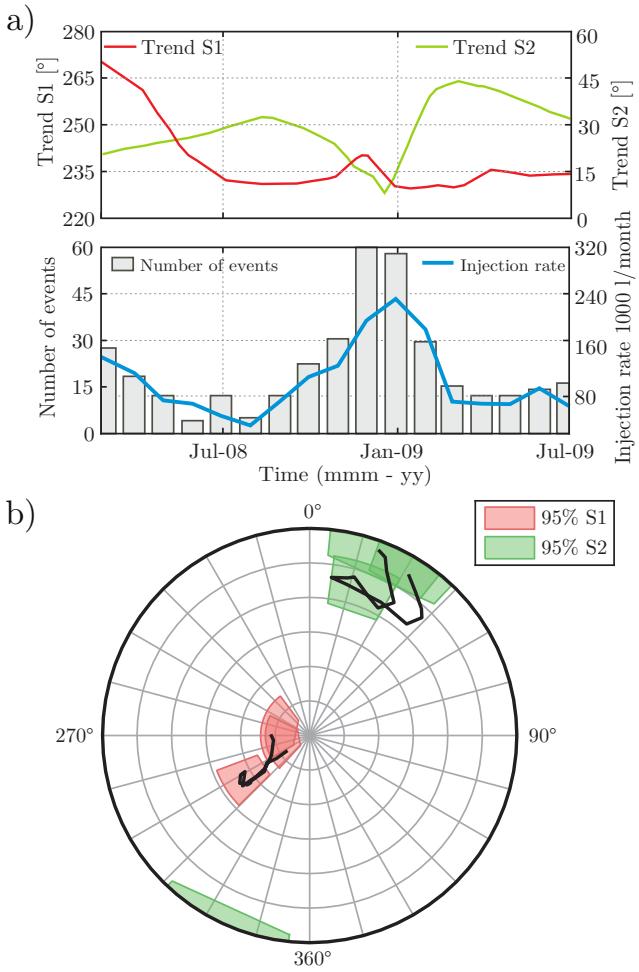

Figure 5.1: Temporal changes in fluid injection induced stress rotations in The Geysers NW site, California (Martínez-Garzón et al., 2013). (a) Rotations in the trend of $S1$ (red) and $S2$ (green) due to fluid injection rate (blue) and number of detected seismic events (grey bars) over the course of 18 months. (b) Schmidt plot of the temporal variations of the initially principal stress axes $S1$ (red) and $S2$ (green) during the fluid injection indicated by stress inversions of focal mechanisms. The stress paths (black line) as well as the 95% confidence intervals (boxes) are indicated.

therefore the orientation of the principal stress axes are altered.

The magnitude of anisotropic stress changes is dependent on several reservoir and material properties (Rudnicki, 1986) and controls the stress rotation. The angle of stress rotation itself is a manifestation of the physical response of a reservoir to fluid injection or depletion and thus depends on the magnitude of the initial differential stress, the material properties of the reservoir rock, and the reservoir treatment such as injection rate and fluid temperature. Thus, if stress rotations are observed and a sufficient amount of reservoir properties are known, the information can be used towards an improved geomechanical characterisation of geological reservoirs.

An observation of injection induced stress rotation is available from the NW part of The Geysers geothermal area, California (Martínez-Garzón et al., 2013, 2014b). A high density seismic network of 32 permanent stations is deployed within the geothermal area (Martínez-Garzón et al., 2013). In the vicinity of the injection wells Prati-9 and Prati-29 within almost five years, 973 focal mechanisms from seismic events with moment magnitude Mw between 1.0 and 3.3 were computed (Martínez-Garzón et al., 2014b). A subsequent spatio-temporally binned stress inversion allowed the observation of rotations of the

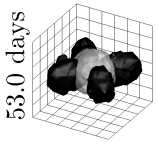

principal stress axes of up to 20 ° (Fig. 5.1) (Martínez-Garzón et al., 2013, 2014b). The time-dependent rotations of the principal stress axes correlate well with the variations in the monthly injection rates into the reservoir from both nearby wells (Fig. 5.1a) (Martínez-Garzón et al., 2013, 2014b). The relationship between fluid injection and stress rotation has recently been observed in another part of The Geysers field (Dreger et al., 2017) and was also confirmed by geomechanical-numerical modelling calibrated on The Geysers scenario (Jeanne et al., 2015).

5.3 Generic Model

In order to identify the reservoir parameters controlling the stress rotations, we built a fully-coupled generic 3D THM model with isotropic and homogeneous rock properties. It has drained pore pressure and fixed temperature boundary conditions at the borders that are far away from the area of interest to prevent boundary effects and feedbacks. The model simulates the injection of a cold fluid at a single point into the centre of a fully saturated hot reservoir. The solution of the poro-elastic equation (Rudnicki, 1986; Altmann et al., 2010, 2014) implies that stress changes are independent of the initial stress state; the stress rotation, however, depends on the ratio of the initial differential stress and the stress changes. The effects of the coupled temperature and pore pressure changes on the stress field are simulated. The reservoir properties, treatment and the initial differential stress can be easily altered in order to compare their influence on the angle of stress rotation. The properties of the reference model are presented in Table 5.1. They are chosen in a way to be comparable to values reported for The Geysers reservoir (e.g. Rutqvist and Oldenburg, 2008; Rutqvist et al., 2013; Jeanne et al., 2015) where injection induced stress rotations have been observed. The parameters printed in italic in Table 5.1 are individually investigated in the sensitivity study with respect to the reference model. Several scenarios in which only a single parameter is altered from the reference value are computed in order to estimate the significance of the influence of the individual parameters on the stress rotation. The scenarios are chosen to represent a reasonable range of maximum and minimum values observed in reservoirs.

Due to the observation of stress rotations by the stress inversion of spatially binned focal mechanisms (Martínez-Garzón et al., 2013), each rotation is actually an integral value valid for that particular rock volume. Hence, the volume enclosed by the seismicity in each stress inversion needs to be accounted for in the model as to guarantee comparison with the observations. Thus, the stress rotations in the model are regarded concerning the angle of rotation within an affected rock volume. The necessity to regard the reservoir volume in which the stress rotation is estimated requires the 3D analysis of the THM model. We use the finite element method with fully coupled partial differential equations for the thermo-poro-elastic processes. A finer resolution is achieved close to the injection point and a coarse resolution at the boundaries (Fig. 5.2c). The fluid injection is assumed to be constant during the entire injection time interval. The finite element solver Abaqus is applied to solve the resulting coupled partial differential equations which characterise the stress due to temperature and pore pressure changes. The equations result in the stress tensor, temperature, and pore pressure at each integration point in the entire model volume with no phase changes assumed.

5.4 Results

To derive the initial differential stress from stress rotations as a physical response of the reservoir to fluid injection, a sensitivity analysis is performed by investigating the key properties controlling the stress rotation. Then, a reservoir characterisation approach is presented.

Table 5.1: Reservoir parameters in the reference model. The properties shown in italics are regarded in the sensitivity analysis and reasonable maximum and minimum values observed in reservoirs are provided. If no reference is provided, standard values are assumed.

Material	Property Value	Minimum	Maximum
Rock density	$2750\,\mathrm{kg/m^3}$		
Young's module rock	$26\,\mathrm{GPa}$		
Poisson ratio rock	0.35		
Porosity rock[a]	5%	2%	30%
Permeability rock[a,b,c]	$1 \times 10^{-14}\,\mathrm{m^2}$	$1 \times 10^{-15}\,\mathrm{m^2}$	$5 \times 10^{-14}\,\mathrm{m^2}$
Bulk modulus solid grains[d]	$50\,\mathrm{GPa}$		
Drained bulk modulus[d]	$26\,\mathrm{GPa}$		
Thermal conductivity rock[e,f]	$3\,\mathrm{W/(m\,K)}$	$1\,\mathrm{W/(m\,K)}$	$5\,\mathrm{W/(m\,K)}$
Specific Heat rock	$800\,\mathrm{J/(kg\,K)}$		
Latent Heat	$100\,\mathrm{kJ/kg}$		
Thermal expansion[e]	$1 \times 10^{-6}\,\mathrm{K^{-1}}$	$0.1 \times 10^{-6}\,\mathrm{K^{-1}}$	$30 \times 10^{-6}\,\mathrm{K^{-1}}$
Density pore fluid[g]	$1000\,\mathrm{kg/m^3}$		
Latent Heat pore fluid[g]	$350\,\mathrm{kJ/kg}$		
Conductivity pore fluid[g]	$0.6\,\mathrm{W/(m\,K)}$		
Specific heat pore fluid[g]	$4200\,\mathrm{J/(kg\,K)}$		
Expansion[g]	Temperature dependent		
ΔT	$50\,\mathrm{K}$	$0\,\mathrm{K}$	$200\,\mathrm{K}$
Injection rate[h]	$100\,\ell/\mathrm{s}$	$25\,\ell/\mathrm{s}$	$175\,\ell/\mathrm{s}$
Injection duration	12 months	6 months	24 months
Differential stress	$2.3\,\mathrm{MPa}$	$0.6\,\mathrm{MPa}$	$8.3\,\mathrm{MPa}$

[a]Moeck (2014), [b]Bear (1972), [c]Martínez-Garzón et al. (2014b), [d]Altmann et al. (2010), [e]Robertson (1988), [f]Rutqvist et al. (2013), [g]IAPWS (1997), [h]Zang et al. (2014)

5.4.1 Sensitivity Analysis

For the sensitivity analysis the reservoir parameters porosity, permeability, thermal conductivity, thermal expansion, and the initial stress state as well as the reservoir treatment parameters temperature difference between rock formation and injected fluid, injection rate, and injection duration were tested across physically reasonable ranges in reservoir environments (Tab. 5.1). The analysis of the results is conducted in a volume-based approach rather than at discrete points in the reservoir. This is in order to be comparable to the observation of stress rotations by a spatio-temporally binned stress inversion of focal mechanism solutions (Martínez-Garzón et al., 2013). Such observations are also within a confined volume in contrast to a single observation point.

Figure 5.2 shows the results for the three significant parameters initial differential stress, permeability, and injection rate as a function of stress rotation within a given volume. An increase in initial differential stress is associated with a decrease in the volume affected by stress rotation. In the reference setting, a

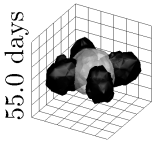

rotation of at least 15–20 ° in a volume of $10^6\,\mathrm{m}^3$ requires a reduction of the initial differential stress to $S1 - S3 = 1.4\,\mathrm{MPa}$. As for the rotation angle this refers to the minimum rotation that can be reliably observed from inversion of focal mechanisms given the fact that the inverted data (focal mechanisms) themselves include an error of typically not less than 10 ° (Bohnhoff et al., 2004). Moreover, a low permeability of the rock is beneficial for stress rotations to occur. A decrease in permeability from $1 \times 10^{-14}\,\mathrm{m}^2$ to $5 \times 10^{-15}\,\mathrm{m}^2$ has a similar effect as the reduction of initial differential stress by about $\Delta(S1 - S3) = 1\,\mathrm{MPa}$. Furthermore, the injection rate is correlated with the stress rotation. Exemplified this means that an increase of the injection rate from $100\,\ell/\mathrm{s}$ to $200\,\ell/\mathrm{s}$ has about the same effect as a decrease in permeability from $1 \times 10^{-14}\,\mathrm{m}^2$ to $5 \times 10^{-15}\,\mathrm{m}^2$ or a reduction of the initial differential stress by $\Delta(S1 - S3) = 1\,\mathrm{MPa}$.

Additionally, Figure 5.2 displays the parameters which prove to have no significant influence on the stress rotation. Changes in the porosity, the temperature difference between reservoir rock and injected fluid, the thermal conductivity of the rock, and the duration of constant injection prove to be entirely insignificant in a long-term scenario of ≥ 6 months. However, minor changes in the volume affected by stress rotation can be observed for changes in the thermal expansion of the rock. Still, rotations induced solely by thermal effects are not large enough to be considered relevant.

5.4.2 Effective Range of Key Parameters

The individual circumstances which favour or prevent the occurrence of a stress rotation are governed by the three key parameters permeability, initial differential stress, and injection rate. In order to investigate the numerical range in which these parameters allow a stress rotation, they are individually tested with realistic values. According to Bear (1972), the permeability in (oil) reservoir rocks is between $10^{-11}\,\mathrm{m}^2$ and $10^{-15}\,\mathrm{m}^2$. Differential stresses between $S1 - S3 = 0\,\mathrm{MPa}$ and $40\,\mathrm{MPa}$ are likely to occur in reservoir settings (Zang et al., 2012; Brudy et al., 1997). Typical injection rates during stimulation of (enhanced) geothermal reservoirs vary between $0.5\,\ell/\mathrm{s}$ and $175\,\ell/\mathrm{s}$ (Zang et al., 2014). The limit above which stress rotation is considered relevant is set to 5 ° in a volume of $25 \times 25 \times 25\,\mathrm{m}^3$ ($= 15625\,\mathrm{m}^3$).

It is revealed that in the range of realistic values, the permeability is the main and decisive factor which regulates the occurrence of stress rotation. In a semi-permeable setting ($10^{-12}\,\mathrm{m}^2$ according to Bear 1972) a very high injection rate of $175\,\ell/\mathrm{s}$ and a very low differential stress ($0.6\,\mathrm{MPa}$) are required in order to generate a stress rotation above the limit. On the other hand, in an impermeable setting ($10^{-15}\,\mathrm{m}^2$ according to Bear 1972) with a medium differential stress ($8.3\,\mathrm{MPa}$) an injection rate of $7.5\,\ell/\mathrm{s}$ is sufficient to create stress rotations larger than the limit. If the initial differential stress is reduced to $S1 - S3 = 0.6\,\mathrm{MPa}$ the same angle of rotation in the same volume is generated by 10% of the injection rate ($0.75\,\ell/\mathrm{s}$). This depicts the small extent of stress rotation control by the magnitude of initial differential stress in comparison to the permeability. In addition to an already low permeability, a small initial differential stress further increases the angle of stress rotation. However, even an unrealistically high value of $S1 - S3 = 50\,\mathrm{MPa}$ allows stress rotations above the limit as long as the permeability is low ($10^{-15}\,\mathrm{m}^2$) and the injection rate high ($175\,\ell/\mathrm{s}$). The injection rate significantly controls the angle of the rotation. Yet it is not a decisive factor for the occurrence of stress rotations since unrealistically high injection rates ($\gg 200\,\ell/\mathrm{s}$) are required to generate a rotation above the limit in a high permeability ($\geq 10^{-10}\,\mathrm{m}^2$) setting with a low differential stress ($0.6\,\mathrm{MPa}$). Even a further increase in the injection rate cannot counterbalance an additional increase in permeability and no stress rotations will occur.

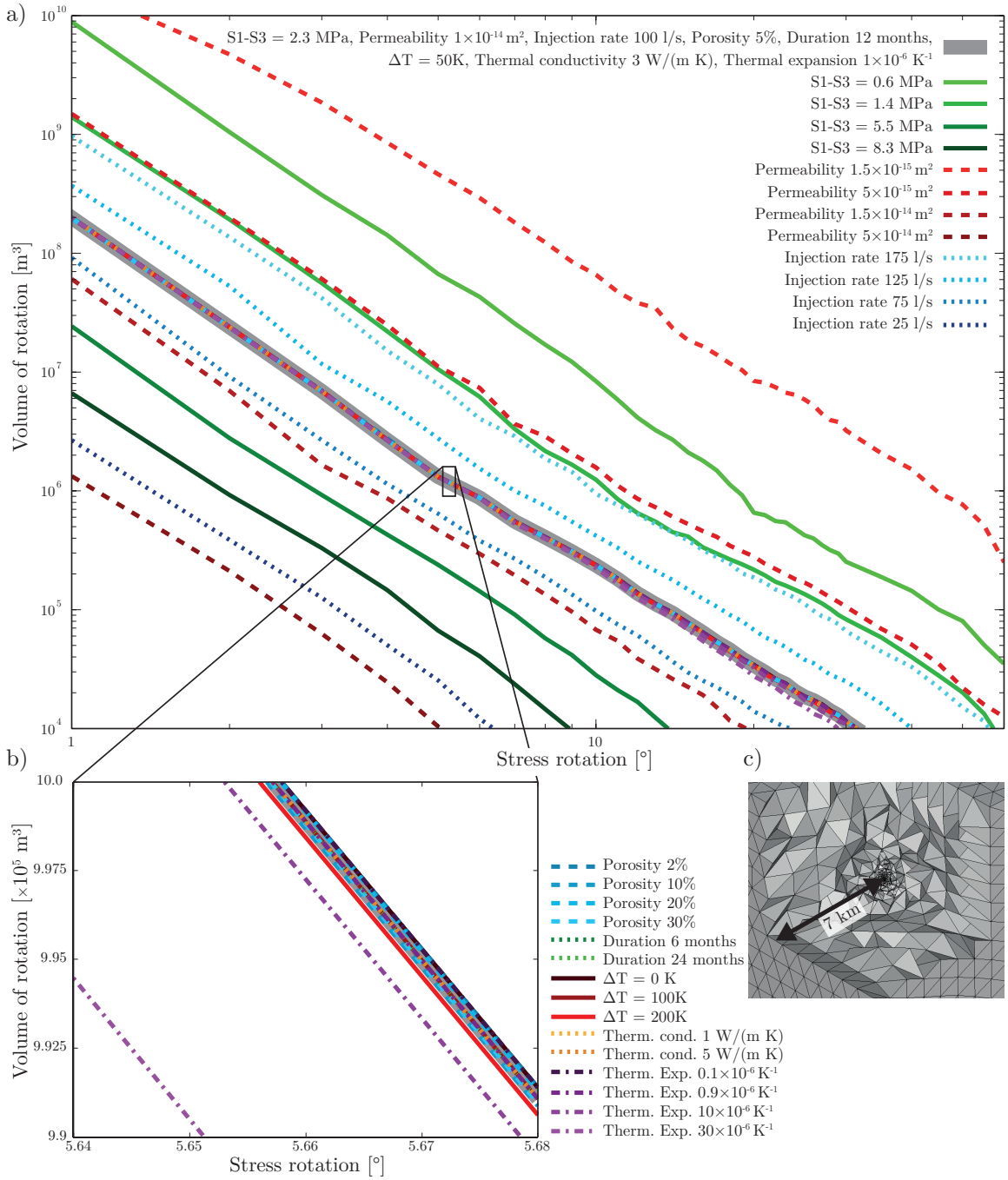

Figure 5.2: (a) & (b) Influence of several parameters on the rotation angle of the principal stress axes displayed in logarithmic scale. On the x-axis is the stress rotation angle; on the y-axis is the volume in m^3 affected by at least the stress rotation specified on the x-axis. In relation to a reference scenario (grey solid) variable angles of stress rotations are indicated. (a) They result from variations in the initial differential stress (green solid), permeability (red dashed), and injection rate (blue dotted). (b) The insignificant influence of the porosity (blue dashed), duration of injection (green dotted), temperature difference (red solid) and thermal conductivity (orange dotted) on the stress rotation angle is displayed in a close-up together with the slightly more prominent influence of the thermal expansion of the rock (violet dot-dash). (c) A cut-view of the generic 3D model indicates the refined discretization towards the injection point in the centre of the model. The modelled injection point has a minimum distance of 7 km from the model boundaries.

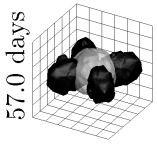

5.4.3 Reservoir Characterisation

The estimation of the differential stress is based on observations of the mean stress rotations by the stress inversion of spatially binned focal mechanisms and several modelled scenarios of stress rotation. The modelled scenarios are identical in their geometry and the reservoir properties and treatment with the exception of the initial differential stress which is altered in each scenario. Every modelled scenario simulates the stress rotation due to fluid injection into the reservoir. The simulated mean stress rotation is estimated in a volume that is equivalent to the volume used for the spatial binning of focal mechanisms in the stress inversion. The resulting scenario and reservoir specific relationships between the initial differential stress and the stress rotation are displayed in Figure 5.3.

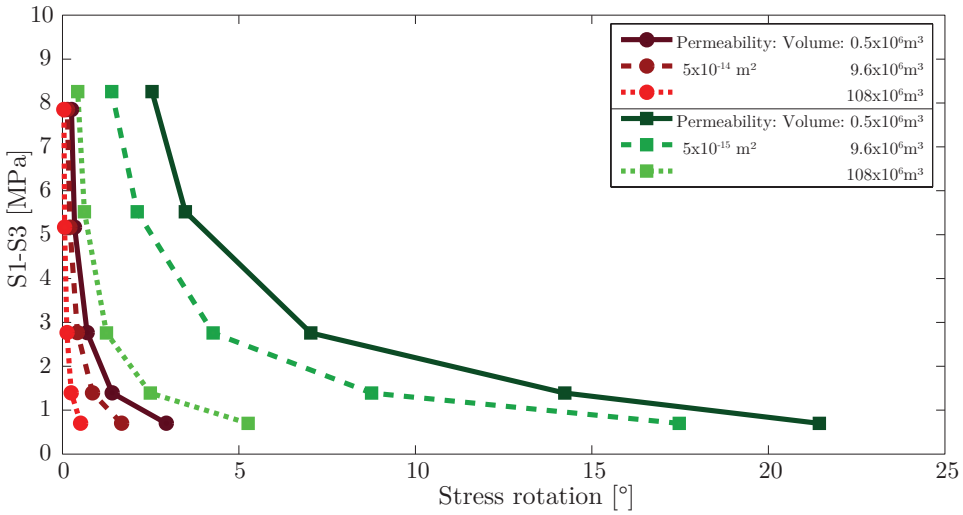

Figure 5.3: The initial differential stress as a function of stress rotation, permeability, reservoir characteristics and volume of observed stress rotation. On the x-axis is the stress rotation, on the y-axis the initial differential stress. Two different permeabilities are assumed ($5 \times 10^{-14}\,\mathrm{m}^2$ (red) and $5 \times 10^{-15}\,\mathrm{m}^2$ (green)) while all other reservoir characteristics remain the same. The stress rotation is evaluated within three different volumes around the injection point and averaged at 200 random locations. For each setting five model scenarios at different initial differential stresses are computed. This results in the displayed points that are used to interpolate reservoir specific curves. The curves depend on the initial differential stress, the permeability, and the regarded volume of interest.

In Figure 5.3 each of the dots and squares represents such a relationship between stress rotation and initial differential stress. Thus, each reservoir specific curve links the observed stress rotation with an initial differential stress state. As an example, two different reservoir permeabilities were assumed in Figure 5.3 ($5 \times 10^{-14}\,\mathrm{m}^2$: red and $5 \times 10^{-15}\,\mathrm{m}^2$: green). The significant difference in modelled stress rotation between the two different permeabilities is in line with the previously indicated sensitivity analysis (Fig. 5.2). The higher permeability results in clearly smaller stress rotations for the same differential stresses compared to the permeability which is one order of magnitude lower (Fig. 5.3). This is especially significant for low differential stresses and high stress rotations. Furthermore, for each permeability scenario the mean stress rotation was obtained in three different volumes ($0.5 \times 10^6\,\mathrm{m}^3$, $9.6 \times 10^6\,\mathrm{m}^3$, and $108 \times 10^6\,\mathrm{m}^3$). This shows the dependency of the stress rotation on the distance to the injection point and the regarded volume respectively which is according to the findings presented in Figure 5.2. Due to the pore pressure diffusion an increase in volume for the estimation of the mean stress rotation results in a decrease of the mean rotation angle (Fig. 5.3).

5.5 Discussion

In this work we investigate the controlling factors for injection induced stress rotations. In order to identify the significant parameters a sensitivity study provides the influence of reservoir properties and treatment on the stress rotation. It indicates that the parameters with the largest influence on the stress rotation are the known injection rate, the often estimated permeability of the reservoir, and the unknown initial differential stress. Other inherent reservoir properties such as porosity and thermal conductivity or reservoir treatment such as injection duration do not contribute in a significant extent to the development of stress rotation in a long-term scenario.

Amongst the three key parameters the permeability is identified to be the most influential one which partly owes to its large variety of observed values in reservoirs (Bear, 1972). Moreover, a high permeability is the only parameter which is able to prevent stress rotations at all because in this case the poro-elastic stress changes are negligible. Significant stress rotations are not expected in reservoirs with permeability larger than approximately $10^{-13}\,\mathrm{m}^2$ even though theoretically stress rotations may occur in such settings due to very high injection rates ($> 150\,\ell/\mathrm{s}$) or very low differential stress ($< 2\,\mathrm{MPa}$). Conversely, a low injection rate ($< 10\,\ell/\mathrm{s}$) and a high differential stress ($> 10\,\mathrm{MPa}$) can significantly limit stress rotations even in a low permeability reservoir ($< 10^{-14}\,\mathrm{m}^2$).

In this work, a THM model was used to simulate stress rotations in a homogeneous isotropic generic test scenario. The described model is ready to alter material properties to relevant values for a certain reservoir type and even include anisotropies. Furthermore, the reservoir engineering parameters can be adapted to represent cyclic injection (Zang et al., 2013; Zimmermann et al., 2010), production and injection from the same well (Tischner et al., 2010), different injection durations, and different injection temperature. The stress rotation angle is quite robust to small changes in injection rate. However, significant fluctuations are expected to result in clearly observable effects (Fig. 5.1a). The approach can be easily adapted to include an actual reservoir geometry. The significance of the influence of reservoir features such as sealing and conducting faults, anisotropies, and inhomogeneities are expected to depend mainly on their deviation from the rest of the reservoir. Small deviations can be neglected. Furthermore, a more realistic injection geometry (line source) and lateral and vertical extent of the reservoir is expected to result in a similar stress rotation angle. Injection and production layouts featuring several boreholes will affect the stress rotation angle in a way that is mainly influenced by the communication of the wells and their distance. Such adaptions of the reservoir model improve the precision of the differential stress estimation approach for a distinct reservoir setting.

The primary challenges remain to be the precise detection and localization of induced seismic events and the availability of information on the permeability. Still, in case of large uncertainties in both parameters conclusive results are provided. In Figure 5.3 the permeability is between $5 \times 10^{-15}\,\mathrm{m}^2$ and $5 \times 10^{-14}\,\mathrm{m}^2$. If stress rotations of more than $7\,^\circ$ are observed an initial differential stress of maximum $3\,\mathrm{MPa}$ can be concluded. Furthermore, the permeability is then most likely in the area of $5 \times 10^{-15}\,\mathrm{m}^2$. This knowledge of the differential stress in most tectonic settings allows the derivation of additional information on the stress state such as S_{Hmax} if the minimum horizontal stress S_{hmin} and the vertical stress S_v magnitudes are available.

As an application to the geothermal reservoir characterisation (Moeck, 2014) our results imply that significant stress rotations are to be expected in reservoirs dominated by crystalline rock, micritic carbonate rock, and sediments with a permeability of $< 10^{-15}\,\mathrm{m}^2$ (porosity $< 15\%$). The individual angle of stress rotation and affected volume is dependent on the site specific injection rate and differential stress. Furthermore, rotations are expected for reservoirs in dolomitic carbonate rocks and sediments with per-

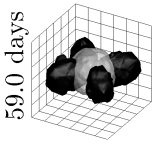

meabilities $< 5 \times 10^{-14}\,\mathrm{m}^2$ (porosity between 15 – 25%). In those settings rotations can be very small or even prevented if the differential stress is large. In addition, a low injection rate can mitigate the angle of stress rotations. Almost no stress rotations are expected in fracture or karst dominated reservoirs or sedimentary reservoirs with a high permeability ($> 10^{-13}\,\mathrm{m}^2$, porosity >25%). In most of those scenarios even very high injection rates and very low differential stress will not lead to a significant stress rotation due to the high permeability ($> 10^{-13}\,\mathrm{m}^2$). In summary, stress rotations are mainly to be expected in petrothermal enhanced geothermal systems (EGS) and their occurrence is likely in hydrothermal reservoirs which require stimulation. This could be the reason that to date they have only been observed at The Geysers geothermal field. Hydrothermal systems are not prone to stress rotations since their initial permeability is usually already high effectively preventing stress rotations.

5.6 Conclusion

We apply a generic 3D thermo-hydro-mechanical model to demonstrate that injection-induced stress rotations in a reservoir can be used to estimate the initial differential stress within a particular rock volume given certain rock permeability and fluid injection rates since they are the physical response of the rock to the injection. The approach requires detailed information on the injection rate and the reservoir permeability which are the most influential parameters. Any further reservoir and engineering properties are secondary for a successful application. In addition, it is indicated that thermal effects have no significant influence on stress rotations. Furthermore, we find that for common differential stress and reservoir treatments stress rotations are only expected in settings with a permeability of less than approximately $10^{-12}\,\mathrm{m}^2$. The presented approach can also be used to first order assess the expected stress rotations within a reservoir prior to injection. In addition, the mitigation of stress rotations by limitation of the injection rate can be estimated. Further investigations are required in order to address the sensitivity of the stress rotation angle to reservoir geometry, faults, anisotropies, and injection scenarios.

Acknowledgments

The authors would like to thank two anonymous reviewers whose comments significantly improved the manuscript. Furthermore, we would like to thank Birgit Müller who read and commented on a initial version of the manuscript. The research leading to these results has received funding from the European Community's Seventh Framework Programme under grant agreement No. 608553 (Project IMAGE). All data for this paper is properly cited and referred to in the reference list or presented in figures.

6 Discussion

The three manuscripts presented in the previous chapters embrace the range from basic stress data analysis and static 3D in-situ stress modelling to transient stress changes due to anthropogenic subsurface processes. In this chapter these manuscripts are discussed individually and in context to each other.

6.1 Stress Data Compilation (Chapter 3)

Chapter 3 describes the first integrated, quality ranked, and comprehensive compilation of the in-situ stress state of Iceland and at the same time in the vicinity of a spreading ridge. In comparison to 38 data records in the World Stress Map (WSM) release 2008 (Heidbach et al., 2010, 2008) in Iceland and the surrounding marine areas 457 new stress data records have been added to the database. The data records are from different stress indicators such as focal mechanism solutions, geological fault slip inversions, and from the analysis of borehole breakouts and drilling induced tensile fractures from image logs of 57 geothermal boreholes. As an island that is located on a hot spot and on a spreading ridge Iceland is tectonically and volcanically highly active. The geologically young age allows the comparably frequent compilation of fault slip data and the orientation of geologically young dykes which serve as stress indicators. Furthermore, the extensive usage of geothermal resources requires a significant amount of boreholes which provide image logs that are potentially suitable for stress orientation estimation.

This thorough compilation and mapping of stress data records helps to identify prevalent regional stress patterns and provinces. Stress patterns are observed on continental scale with wavelengths longer than 1,000 km (Coblentz et al., 1998; Reiter et al., 2014; Rajabi et al., 2017) as well as on regional scale with wavelengths of approximately 200 km as observed in Iceland (Fig. 6.1), in the Taranaki Basin (Rajabi et al., 2016c), or in other basin scaled areas (Snee and Zoback, 2016; Bada et al., 2007). In addition, stress pattern that feature reorientations due to local effects are also frequently observed on reservoir scale with wavelengths of 10 km or smaller (Heidbach et al., 2007; Tingay et al., 2010; Rajabi et al., 2016b). Furthermore, S_{Hmax} reorientations with depth indicate mechanical decoupling by e.g. salt layers or detachment horizons (Roth and Fleckenstein, 2001; Heidbach et al., 2007; Röckel and Lempp, 2003). Stress patterns are either indicated visually (e.g. Chap. 3, Grünthal and Stromeyer 1992, or Müller et al. 1992) or with algorithms that spatially smooth and filter the stress data records in order to provide a mean orientation of the stress field (Rajabi et al., 2016c; Reiter et al., 2014; Heidbach et al., 2010; Müller et al., 2003; Coblentz and Richardson, 1995). Ziegler and Heidbach (2017a,b) describe such an improved algorithm that takes advantage of the comprehensive information provided by the WSM for the computation of a mean orientation of S_{Hmax} at equally spaced grid-points (Fig. 6.1). The mean S_{Hmax} orientation is computed from the individual data records weighted by their WSM quality, the method of stress indication, and/or their distance from the grid point (Ziegler and Heidbach, 2017a). Optionally, the wavelength of the stress pattern is computed.

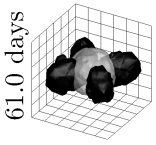

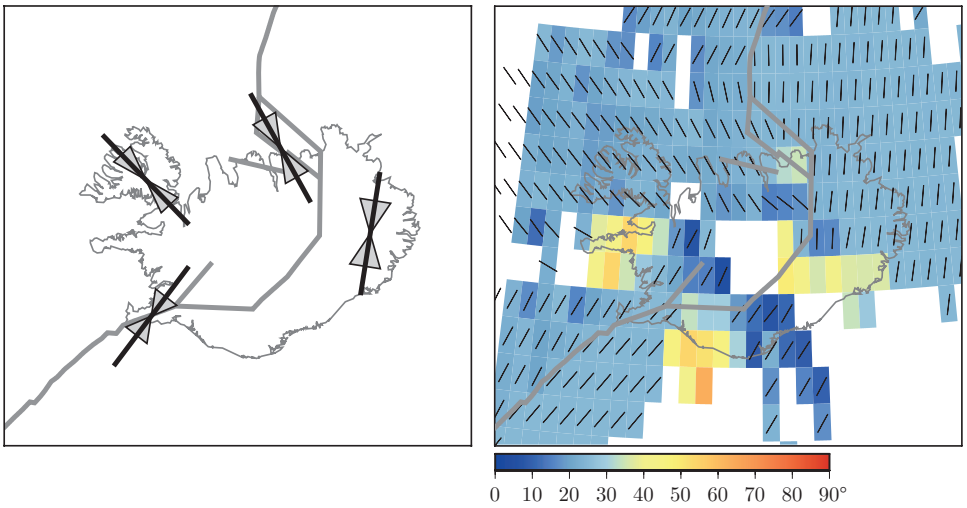

Figure 6.1: The stress pattern of Iceland visually derived (left, cf. Fig. 3.10) and computed by an algorithm (right). Both patterns are derived from A-D quality WSM data records. The visually derived stress pattern (left) shows the orientation of S_{Hmax} by thick black lines and the uncertainties as triangles. The computed mean azimuth of S_{Hmax} (right) is derived from quality and distance weighted data records by the algorithm described in Ziegler and Heidbach (2017a,b). The black lines indicate the orientation of S_{Hmax} on a 0.5 ° grid. The variance of the mean azimuth of S_{Hmax} is indicated by the colour coded pattern. In both maps the plate boundaries (thick grey line) according to Einarsson (2008) and Bird (2003) are marked.

The analysis of the compiled stress data records reveals four distinct stress orientation provinces in Iceland (Fig. 6.1 and Fig. 3.10 on page 37 in Chapter 3). This proves the existence of a distinct stress field with an S_{Hmax} orientation parallel to the plate boundary in the direct vicinity of a spreading ridge. Even though this pattern has been previously indicated by focal mechanism solutions in other areas (Wiens and Stein, 1984; Heidbach et al., 2008) this is the first time that it is observed by various different types of stress indicators. This includes stress indicators which are not biased by the possibility to be a plate boundary event such as borehole breakouts (Heidbach et al., 2010; Heidbach, 2016). The ridge parallel S_{Hmax} orientation seems to rotate with increasing distance from the ridge. In the Westfjords which is the area farthest away from the currently active rifting the orientation of S_{Hmax} is ridge normal and therefore parallel to the plate motion. It is assumed that this reorganization of the stress orientation results from the increasing distance from the extensional forces of the plate boundary in addition to the weak tensile strength of the newly formed rock material (Wiens and Stein, 1984). In order to confirm this observation the influence of a palaeo-rift on the stress field in the Westfjords remains to be quantified especially since in that area only stress data records from geological fault slip inversions are available (Bergerat and Angelier, 1998; Gudmundsson et al., 1996) that might show the orientation of a palaeo stress field rather than that of the current stress field. Even though the guidelines for geological data were strictly observed and proved to be valid in other Icelandic areas the highly dynamic tectonic setting increases the potential for such a misidentification of a palaeo stress field as the contemporary stress field. Therefore, the inclusion of additional stress data records from other indicators is desirable in such areas.

The continuous increase in stress data records provides increasingly detailed information on the stress field (Heidbach et al., 2008, 2016a). Densely populated areas close to plate boundaries such as Japan or California boast an extreme wealth of available data records (Heidbach et al., 2016a). In some areas even local perturbations from borehole to borehole can be observed (Rajabi et al., 2016b). Concurrently, large areas have only very few to no information on the stress field since the data records are not evenly

distributed (Heidbach et al., 2016a).

The information provided by a compilation of stress data records and a subsequent analysis of the stress pattern is useful in order to assess the stability of the rock mass and pre-existing faults in terms of the potential for natural and induced seismicity (Morris et al., 1996; Connolly and Cosgrove, 1999; Bott, 1959; Anderson, 1905). The integrity and safety of geotechnical installations such as boreholes, tunnels and caverns also depend on the orientation of S_{Hmax} (Plumb and Hickman, 1985; Cai, 2008; Zang and Stephansson, 2010). In addition, the orientation of S_{Hmax} indicates the preferred orientation of permeability, stimulated fractures, and natural fluid pathways (Barton et al., 1995; Sibson, 1996; Brown, 2009; Zang and Stephansson, 2010). Hence knowledge of its orientation is of imminent interest for exploration, stimulation, production, and injection operations. Furthermore, the stress pattern is used in order to find the orientation of boundaries of geomechanical in-situ stress models (Chap. 4, Reiter and Heidbach 2014; Hergert et al. 2015; Fischer and Henk 2013).

6.2 Geomechanical Modelling (Chapter 4)

In order to derive a continuous stress state from single data records 3D geomechanical-numerical modelling is essential. The presented calibrated modelling approach consists of two differently sized models that together demonstrate a multi-stage stress modelling scheme. In order to maintain the time required for computation without a reduction of element numbers the multi-stage approach separates the requirements of a single comprehensive model and assigns them to two or more different models. In this example, a large scale model with a coarse resolution is calibrated on the available stress data records. This model then provides the boundary conditions for a small scale reservoir model which has a considerably higher resolution but no data records for calibration within its perimeter. Here a regional scale ($70 \times 70 \times 10\,\mathrm{km}^3$) model of the greater Munich area and a generic reservoir scale ($10 \times 10 \times 10\,\mathrm{km}^3$) model are used. The reservoir model is applied to assess the fault criticality, rock stability, and to optimise borehole trajectories. Furthermore, it provides an initial stress state for THM reservoir models or for other subsurface engineering structures such as mines or radioactive waste disposal sites.

The calibration and multi-stage workflow presented in this work proves to result in a fast and efficient 3D geomechanical-numerical estimation of the in-situ stress state. The calibration scheme enables the weighting of input data according to credibility such as used in the WSM and the Quantitative World Stress Map (Q-WSM) (Zang et al., 2012). The multi-stage approach, which is presented here as a two-stage approach, can be easily enhanced to include three or even more models of different scales (Fig. 6.2). An approach featuring four models includes (1) a plate-wide continental scale model that simulates the stress state mainly as a result of large scale geodynamical processes (Grünthal and Stromeyer, 1992; Gölke and Coblentz, 1996), (2) a country wide model that has a simplified geology and is calibrated on the stress state from the continental model in addition to stress data records, (3) a regional model that has a detailed geological background model with dominant local features that is calibrated on the country wide model and on stress data records within its perimeter, and (4) a reservoir scale model that is entirely calibrated on the stress state provided by the regional model and has a highly detailed geometry (Fig. 6.2).

The multi-stage approach is beneficiary from two points of view. (1) The local stress state largely depends on the far-field stresses. Therefore, a calibrated large scale model provides ideal first order information on the local stress state. Further details of the local stress field are a result of zones of weakness and density or stiffness contrasts as results from local processes (Roche et al., 2014; Roche and van der Baan, 2017). (2) Usually no data records for calibration are available in the area of the local

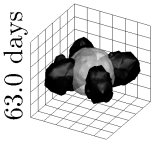

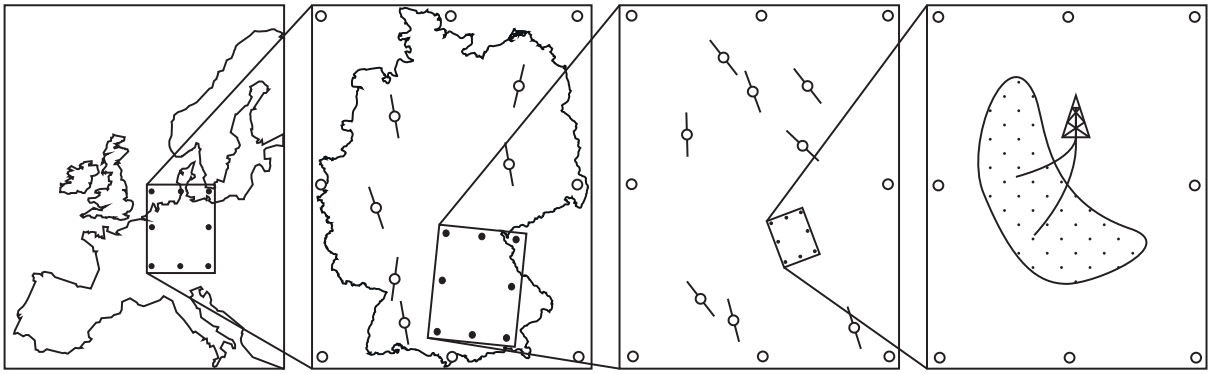

Figure 6.2: A four-stage approach in 3D geomechanical modelling. Data records used for calibration (open circle with line), calibration data derived from a larger model (open circle), and data points in models that provide calibration data for a smaller model (dot) are displayed. From left to right: (1) A continental scale model is calibrated on geodynamic and plate tectonic data. (2) It provides calibration data for a country scale model that is additionally calibrated on stress data records. (3) A regional model with a refined stratigraphy is calibrated on the country scale model and additional local stress data records. (4) Finally a reservoir scale model is entirely calibrated on data from the regional model.

model. Therefore, the calibration data needs not be provided otherwise. The multi-stage approach allows using the calibrated stress state from larger scale models for the calibration of the local model.

The larger scale in-situ stress models can be organised in a way that is comparable to freely available community models such as the geologic models Hessen 3D (Arndt et al., 2011) and GeORG (Watzel, 2013), or the temperature model GeotIS (Schulz et al., 2007). Organised in such a way, an in-situ stress model is regularly updated and re-calibrated according to the latest available stress data records and scientific advances. The easy multi-stage calibration procedure ensures that derived reservoir models can be updated accordingly with minimum cost. Furthermore, each reservoir which is accessed within the larger scale models perimeter potentially provides additional stress data records. Those can be used for validation of the previous models and an improved calibration of the larger scale models.

The speed of the multi-stage calibration approach enables the quantification of the influence of the uncertainties in the input data on the model results. The most important issues are clearly the lack of S_{Hmax} magnitude data as well as the uncertainties in the material properties. This information can be used as a first order indication which factors are most important for an improvement of model significance. Due to the fast advances in computation power a more thorough investigation of the uncertainties of the modelling approach will become feasible. This enables the quantification of the influence of uncertainties in complex input data such as the geologic model (Wellmann and Regenauer-Lieb, 2012; Wellmann, 2013; de la Varga et al., 2015). The uncertainties in geologic models, their magnitude, and mitigation methods are already indicated (Bond et al., 2015). The influence of these uncertainties on the stress field remains to be investigated. The approach to uncertainty estimation indicated in Chapter 4 can be applied to various sources of uncertainties in order to compute a wide range of scenarios. With a large number of different scenarios the expected variability and spectrum of end-members can be assessed in a statistical approach.

The regionally modelled in-situ stress state of the Bavarian Molasse Basin clearly shows the influence of the uncertainties in calibration data (Fig. 4.6 on page 52 in Chapter 4). Furthermore, a laterally and vertically variable stress state that depends on the material properties of the different geologic units is indicated (Fig. 4.8 on page 54 in Chapter 4). Close to the surface thrust faulting and strike slip regimes are prevalent. With depth first strike slip and then normal faulting becomes predominant (Fig. 4.6 on

page 52 in Chapter 4). Moreover, the regime is also dependent on the material properties and according variability is observed (Figs. 4.6 and 4.8 in Chapter 4). Due to the high uncertainties in calibration data for the S_{Hmax} magnitude the differential stress $S1 - S3$ is uncertain. However, a clear pattern of an increase of differential stresses towards the South is observed (Fig. 4.6 in Chapter 4).

The reservoir scale model indicates the generally low criticality of pre-existing faults in the prevalent orientations found in the Bavarian Molasse Basin (Fig. 4.7 on page 53 in Chapter 4). Moreover, a strong variability in criticality is observed dependent on the exact orientation of individual fault segments. This clearly indicates favourable and adverse areas for borehole trajectory intersections with faults or target areas for geothermal exploration. Even though the criticality of the faults in the Molasse Basin is generally low and the rock is mainly stable, the large uncertainties due to material properties and calibration data suggest paying attention to the results of the models. Even if faults are entirely favourably oriented and it is indicated that they are far away from failure borehole trajectories should be planned to intersect pre-existing faults in areas of the lowest criticality in order to minimise the risk of failure. This is particularly important if a fault is targeted (Megies and Wassermann, 2014; Wolfgramm et al., 2007) since reservoir engineering, exploitation, and (re)injection additionally alters the fault criticality and also the optimal orientation of faults in the stress field due to its rotation (Chapt. 5). The pore pressure is disregarded in this model since it is constant. In order to estimate the criticality including the pore pressure it can be subtracted from the models resulting stress tensor. Slip tendency is then still low and the values are identical to modelling approaches that include the pore pressure from the beginning (pers. comm. J. Reinecker). Pore pressure changes and their effects on the stress field due to fluid injection and production can be simulated in a local model with a calibrated initial in-situ stress state as well.

6.3 Process Modelling (Chapter 5)

The third manuscript investigates transient anthropogenic stress changes. The rotation of the principal stress axes due to long-term fluid injections ($\leq$6 months) into reservoirs have been modelled and a sensitivity study on the dependence on several different reservoir properties and treatments is conducted by means of a generic 3D thermo-hydro-mechanical (THM) model. The indicated key parameters that control the angle of stress rotation are the reservoir permeability, the initial differential stress, and the injection rate. The reservoir permeability is found to be the decisive factor for the occurrence of a stress rotation. Even favourable conditions in terms of a small initial differential stress ($<$1 MPa) and a high injection rate ($>150\,\ell/s$) cannot produce a stress rotation in a highly permeable reservoir ($> 10^{-11}\,m^2$). Concurrently, in a low permeable rock ($< 10^{-15}\,m^2$) even low injection rates and a high initial differential stress will lead to at least small stress rotations.

The phenomenological characteristics of the stress rotation in the generic 3D model is shown in Figure 6.3 for the reference scenario after an injection of 12 months. The temporal evolution of the stress rotation is documented in the flip-book (printed copy, starting page 1, bottom right) or in the according video file (supplementary material on page VII). The volume of a stress tensor rotation of at least $\pm 1\,^\circ$ (black) and pore pressure increase by at least 10 MPa (grey) are displayed. The gird spacing is 250 m.This indicates that a quasi steady-state of stress tensor rotation is reached shortly (10 – 20 days) after the start of injection while the pore pressure front is further advancing. The stress rotations occur in lobes around the injection point, with no rotation on the vertical planes that strike in the orientations of S_{Hmax} and S_{hmin}. The limitation of the lobes to the quadrants which are defined by the orientations of S_{Hmax} and S_{hmin} and no such segmentation by the orientation of S_v is due to the initial stress state in the generic model that favours horizontal stress rotations. These characteristic stress rotation lobes are explained

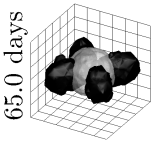

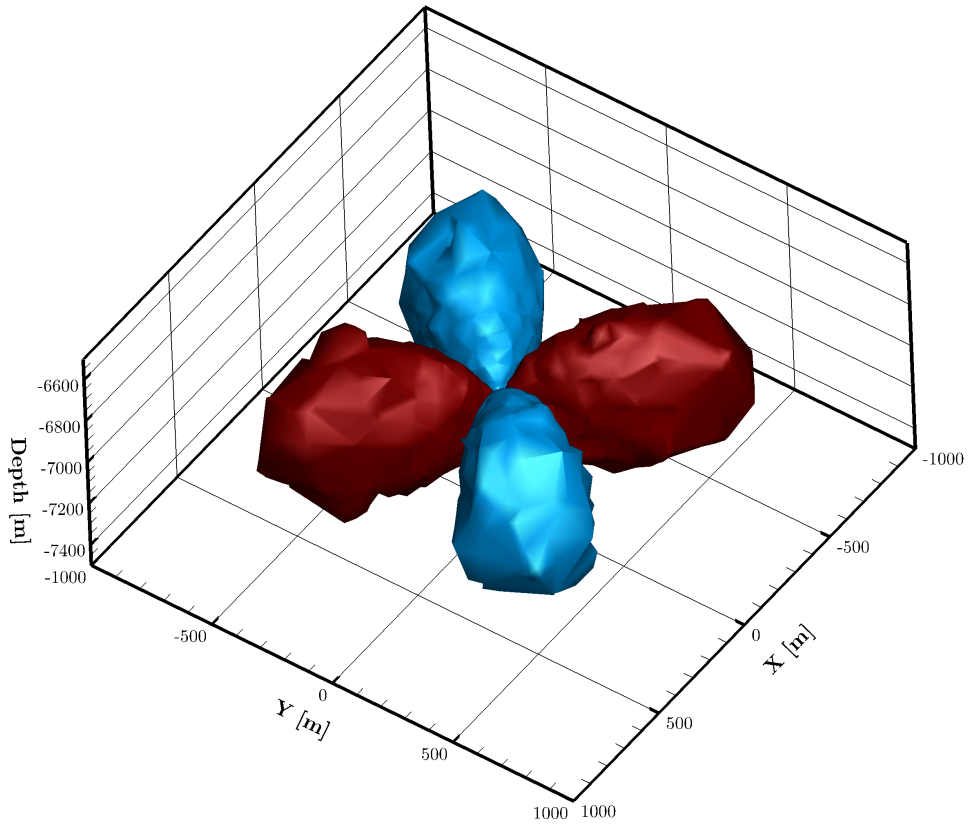

Figure 6.3: Stress rotation in the reference scenario after 12 months of injection at X = 0 m, Y = 0 m, and Z = −7000 m. The displayed volumes show the extent of a stress rotation angle that exceeds 1 ° (red) and -1 ° (blue). S_{Hmax} is oriented parallel to the x-axis.

by the theory of pore pressure stress coupling (Rudnicki, 1986; Altmann et al., 2010, 2014). In Altmann et al. (2010, 2014) the induced stress changes are described in terms of the radial and tangential stress changes relative to the injection point (Fig. 6.4a). Generally the radial stress changes are larger than the tangential stress changes (Altmann et al., 2014). In the planes that are normal to the orientations of S_{Hmax} and S_{hmin} the stresses are affected by either the tangential or the radial stress changes (Fig. 6.4a). For the exemplified location and setting in Figure 6.4b the altered stress states S'_{Hmax} and S'_{hmin} are described by

$$\begin{aligned} S'_{Hmax} &= S_{Hmax} - \Delta S_{tan} \\ S'_{hmin} &= S_{hmin} - \Delta S_{rad} \end{aligned} \tag{6.1}$$

with the tangential stress changes ΔS_{tan} and the radial stress changes ΔS_{rad}. Moreover, off the planes normal to the stress orientations the stress changes are significantly larger since S_{Hmax} and S_{hmin} are both affected by the tangential and radial stress. This situation is exemplified in Figure 6.4c and is described by

$$\begin{aligned} S'_{Hmax} &= S_{Hmax} - \Delta S_{tan} \sin(\Theta) - \Delta S_{rad} \cos(\Theta) \\ S'_{hmin} &= S_{hmin} - \Delta S_{rad} \sin(\Theta) + \Delta S_{tan} \cos(\Theta) \end{aligned} \tag{6.2}$$

with Θ as the angle between the orientation of S_{Hmax} and the line between the injection point and the location of observation. This comparison indicates the larger stress changes that occur off the planes

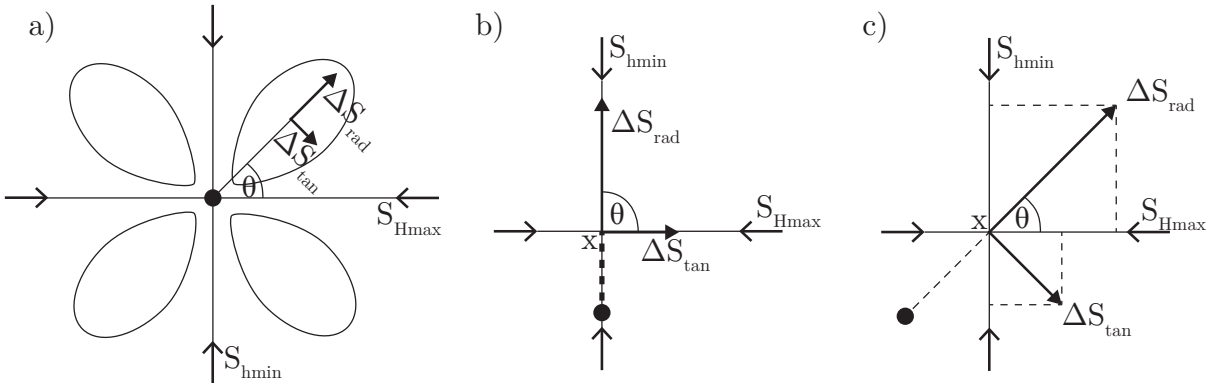

Figure 6.4: The differences in radial and tangential stress changes according to the theory of pore pressure stress coupling (Rudnicki, 1986; Altmann et al., 2010, 2014). (a) The lobes of stress rotation in a generic setting with the different changes in the radial stress ΔS_{rad} and the tangential stress ΔS_{tan} relative to the injection location (black point). The angle Θ is between the orientation of S_{Hmax} and the direction towards the observation point **x**. (b) The radial and tangential stress changes in a setting in which $\Theta = 90°$ (Eqn. 6.1). (c) The radial and tangential stress changes in a setting in which Θ is not a right angle or zero. The influence of Θ on the stress changes that affect S_{Hmax} and S_{hmin} respectively is indicated (Eqn. 6.2).

normal to the orientation axes of S_{Hmax} and S_{hmin} and hence explains the 3D pattern of stress rotation defined by the orientation of the reduced stress tensor.

The angle of stress rotation is observed within a confined volume by the stress inversion of focal mechanism solutions (Martínez-Garzón et al., 2013, 2014b). The 3D modelled stress rotation also allows the volumetric observation of stress rotations. Together with the permeability, injection rate, and initial differential stress that control the stress rotation this opens up the possibility for the estimation of inherent reservoir relationships. The injection rate is generally available as well as the permeability of reservoir rocks which are frequently available from drill-cores, circulation tests, or extensive databases (Koch, 2009; Clauser et al., 2007; Bär et al., 2017; Angenheister, 1982). Hence, observed angles of stress rotation can be used to estimate the initial differential stress as the remaining unknown. This estimation serves in order to assess the stress state and use it for borehole and reservoir stability evaluation and the estimation of fault criticality. Furthermore, the estimation of the initial differential stress in an already modelled stress state following the approach in Chapter 4 can be validated. Along with a hydraulic fracturing experiment that estimates the magnitude of S_{hmin} the initial differential stress is used to derive the magnitude of S_{Hmax} in most tectonic settings. Coincidentally, if the initial differential stress is known the reservoir permeability can be estimated in an analogous approach.

The rotation of the principal stress axes additionally have an effect on the potential for induced seismicity by the reactivation of pre-existing faults. The injection of fluids into a reservoir not only increases the pore pressure and therefore the criticality but also rotates the stress tensor. This rotation alters the optimal orientation of faults in the reservoir. Therefore, faults which were previously not optimally oriented may now become critical or even fail. The size of the fault segments that become more optimally oriented are directly linked to the rock volume that is affected by a stress rotation of a certain angle. Coincidentally, the expected magnitude of induced seismicity is as well linked to the volume of stress rotation since most likely only the part of the fault that is affected by stress rotation will fail. However, a further propagation of the fault rupture in a stress field that is not optimally oriented for this fault orientation is unlikely.

This study indicates that the reservoir types which are potentially affected by injection induced stress

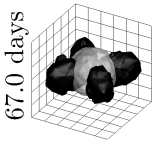

rotations are therefore mainly characterised by their permeability. Figure 6.5 shows the geothermal play type characterisation according to Moeck (2014) which includes different types of reservoir rock and their permeability-porosity relationship. The diagram indicates that stress rotations are only a minor concern in hydrothermal systems such as high enthalpy systems in Iceland, (Ragnarsson, 2015), El Salvador (Fabriol et al., 1998), or New Zealand (Kissling and Weir, 2005), as well as in low enthalpy systems in Germany (Weber et al., 2015). They are either mainly karst or fracture dominated or have a porous reservoir rock with a generally high permeability and porosity (Fig. 6.5). As soon as a reservoir requires enhancement in order to generate fluid pathways the initial permeability is low and hence the potential for stress rotations increases. This is the case for crystalline reservoir rock which has been enhanced such as in Basel (Häring et al., 2008), Soultz-sous-Forêts (Baria et al., 2006), Cooper Basin (Baisch et al., 2015), or Paralana (Albaric et al., 2014). Furthermore, carbonate reservoir rocks of low permeability such as in the Alberta Basin (Weides et al., 2013) are also potentially affected by stress rotations.

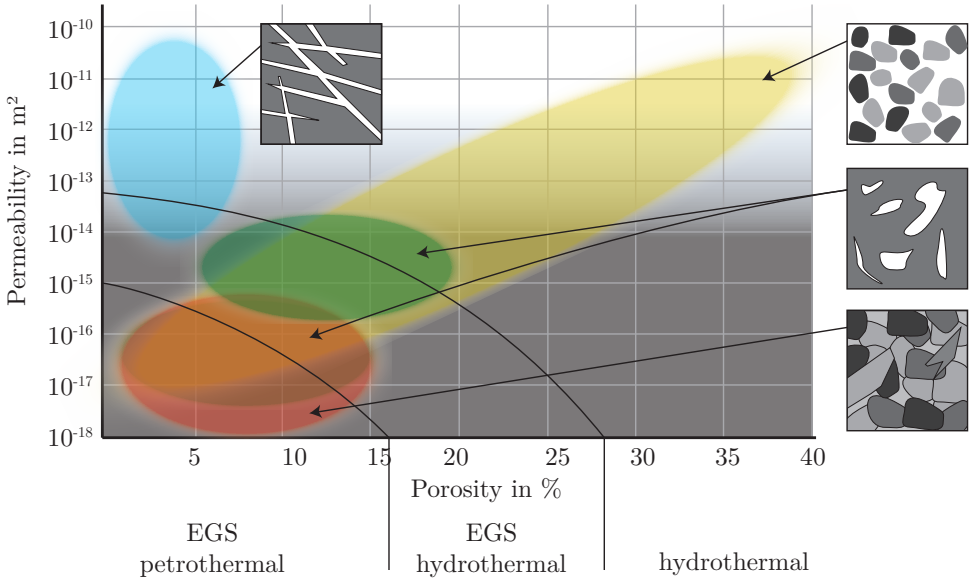

Figure 6.5: Different geothermal play types characterised by porosity (x-axis) and permeability (y-axis), the prevalent geothermal reservoir systems (Moeck, 2014), and their possibility for stress rotation (grey area is prone to stress rotation). For four different reservoir types the potential for stress rotation is indicated and the rock types are exemplified in sketches: Fracture and karst dominated (blue) with high permeability and low porosity. Porous rock with a proportionality between permeability and porosity (yellow). Dolomitic and micritic carbonate rock (green) with high porosity but low permeability. Crystalline rock (grey) with low porosity and permeability.

In order to increase the knowledge of stress rotations further sensitivity studies are required. The possibility of production induced stress rotations, which have not been observed yet, can be investigated with the presented model. Furthermore, the influence of anisotropies and inhomogeneities in the permeability, time-dependent variations in the injection rate, as well as alterations in the pore pressure such as overpressure can be investigated with a slightly altered model. Additional changes in the model geometry are required to allow the investigation of the influence of sealing and conducting faults and the injection geometry. A larger reservoir model is required in order to investigate the influence of production and (re)injection from different boreholes. Any investigation concerning the influence of the injection geometry is possible in such an enhanced model but makes most sense in an actual reservoir setting with according geometry. Finally, the influence of the reservoir geometry and several active boreholes for production and (re)injection on stress rotation is investigated by means of a highly resolved and adaptable

model. Eventually, a validation of the presented approach on a reservoir that has a simple geology is well researched and closely monitored is desirable.

6.4 Cumulative Discussion

The in-situ stress field results from various different processes such as plate tectonics, topographic features, isostasy, seismic cycles, and anthropogenic subsurface engineering (Zoback et al., 1989; Zoback, 1992; Müller et al., 1997; Heidbach et al., 2007). The stress field can be characterised by stress data compilations such as performed in Chapter 3 as a part of the WSM database (Heidbach et al., 2010, 2016a) but ultimately magnitude information such as provided by the Q-WSM is required (Zang et al., 2012). However, a continuous description of the stress field is only achieved with a calibrated geomechanical-numerical model (Chap. 4, Reiter and Heidbach 2014; Hergert et al. 2015). The anthropogenic influence on the stress field caused by processes such as reservoir engineering can be highly significant (Martínez-Garzón et al., 2013; Tingay et al., 2015; Evans et al., 2012). As one result of reservoir treatment the phenomenon of fluid injection induced stress rotation is investigated in Chapter 5.

The high versatility and close link of the presented methods is displayed in Figure 6.6. An application of the entire workflow begins with the stress data compilation that provides calibration data for a regional geomechanical in-situ stress model. The multi-stage approach is then used in order to derive the in-situ stress state within a high resolution reservoir model which in turn provides an initial stress state for a process modelling. Finally, a THM model of the planned injection into the reservoir predicts the expected angle of stress rotation. This is used for the assessment of the criticality of pre-existing faults in a changing stress field that possibly renders them optimally oriented. Alternatively, if observations of the stress rotation angle are available from initial injection experiments detailed information of the mean reservoir permeability can be derived which are useful in order to determine the expected reservoir behaviour in a THM model.

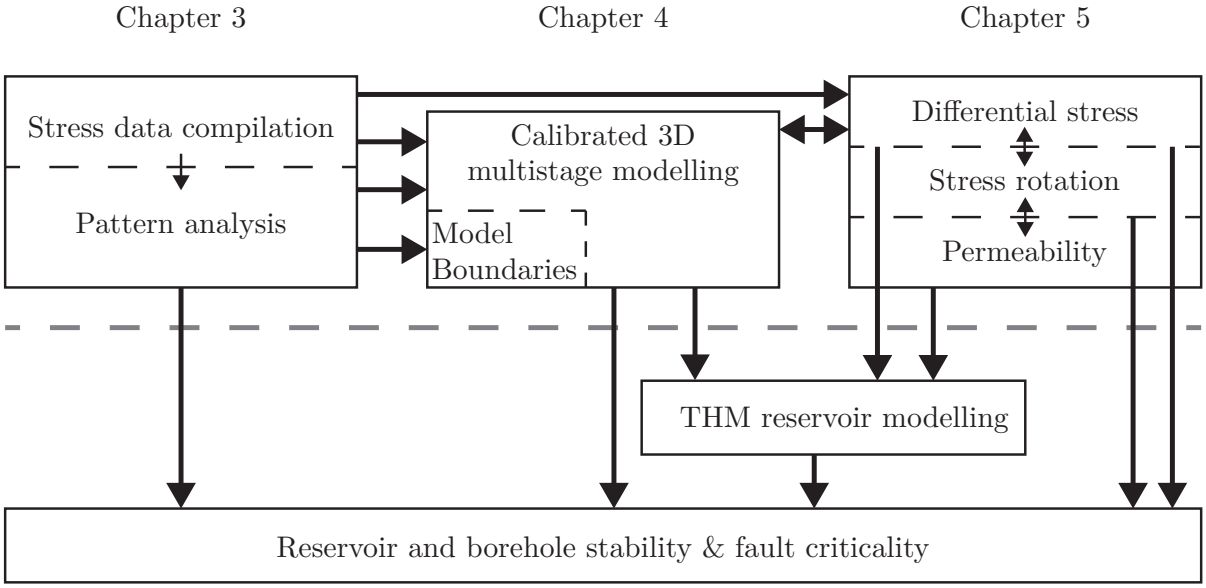

Figure 6.6: Each single component of the workflow described in this thesis provides valuable information for a safe subsurface engineering. In synthesis the strength of the individual methods is increased by many links that are used to share the available information and benefit from the cooperative performance of the methods.

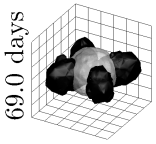

Moreover, each approach on its own provides valuable information for a safe and sustainable underground engineering. The plain compilation of stress data records and estimation of the local orientation of S_{Hmax} is useful in order to assess the criticality of faults of known orientation (Fig. 6.7). An analysis of the stress pattern and its wavelength and variance provides additionally required information. Long wavelength and a low variance derived from densely distributed data records indicate few local perturbations of the stress field. Short wavelengths and a high variance, however, imply the possibility of many local perturbations that may require additional observations of the stress field.

Even a simple geomechanical model provides information on the stress state and local perturbations e.g. due to contrasts in the material strength. In conjunction with information on the orientation and geometry of faults such a model significantly improves the knowledge of the fault criticality (Fig. 6.7). Furthermore, a detailed planning and optimisation of drill-paths with respect to the local stress field and faults is facilitated which significantly increases the prospect of success and safety and reduces the cost of subsurface engineering. Finally, even a rough estimation of the stress field is a valuable initial condition for THM reservoir models which are then able to provide information on the absolute fault criticality and rock stability during and after the reservoir treatment.

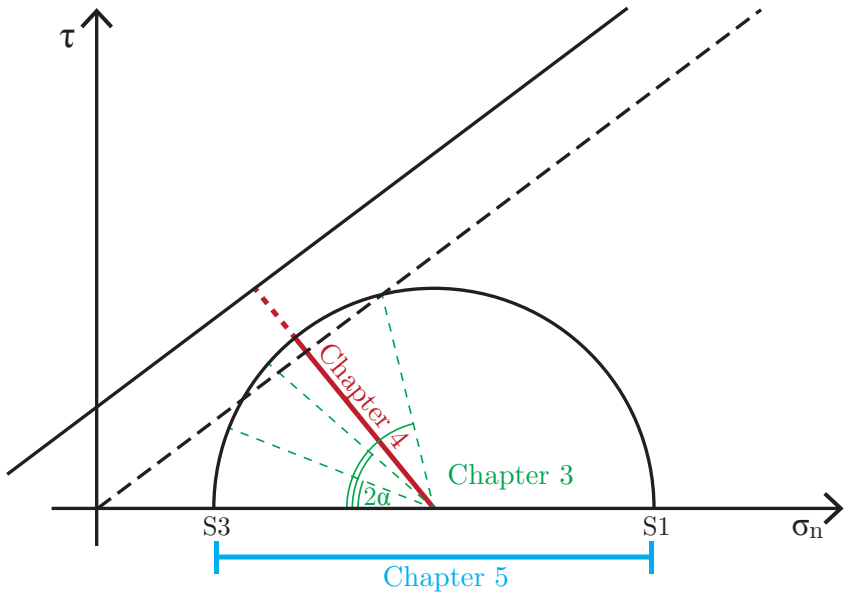

Figure 6.7: The Mohr-Coulomb diagram indicates the contributions of this thesis to the assessment of rock stability. The observation of S_{Hmax} orientation patterns in Chapter 3 helps to assess the criticality of pre-existing faults and to find the angle of α between the fault and S_{Hmax}. The modelling approach in Chapter 4 uses slip tendency and fracture potential to indicate the criticality in terms of the distance of faults and the intact rock from failure. The analysis of observed stress rotations in Chapter 5 is used in order to estimate the initial differential stress.

Observations of stress rotations can be used in order to derive the initial differential stress state in a reservoir. The differential stress is a significant value for the estimation of the criticality of faults in terms of the distance of faults from failure and necessary information to model absolute stress changes due to reservoir engineering (Fig. 6.7). In addition, estimations of the initial differential stress from stress rotations can be used as calibration data in models of the in-situ stress state or simply to verify the modelled stress state. Furthermore, if the initial differential stress is known the reservoir permeability can be derived from observed stress rotation angles. As an important reservoir parameter information on the permeability is useful for long-term reservoir behaviour, stimulation, and injectivity. As another

option, the expected stress rotation is simulated before any injection and provides a prediction of the altered fault criticality due to the rotated optimal orientation for fault reactivation.

In addition to the mutual workflow, each single publication compiled in this thesis provides a gain of knowledge in geomechanics. The stress data record compilation of Iceland (Chap. 3) in addition to the compilations in New Zealand (Rajabi et al. 2016c, Rajabi et al. in prep.) investigate the characteristics of the stress field at plate boundaries. In this context a versatile tool for the stress data and pattern analysis provided by Ziegler and Heidbach (2017a,b) was applied for the first time. The 3D geomechanical-numerical multi-stage modelling of the contemporary in-situ stress field (Chap. 4) provides a fast method for a comprehensive and detailed stress field analysis that is not limited to reservoir applications. Furthermore, the model provides the stress state for the city of Munich where a highly ambitious geothermal development is currently implemented (Stadtwerke München GmbH, 2016). Finally, the investigated key control factors for stress rotations indicate a method to derive stress magnitudes in terms of the differential stress from observed stress rotation angles (Chap. 5). Concurrently, the reservoir permeability can be estimated if the stress rotation angle is observed and the initial differential stress is known. In summary, the three manuscripts describe and provide methods to investigate the in-situ stress state and anthropogenic changes in order to estimate the rock stability and fault criticality.

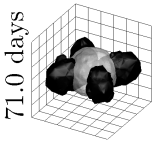

7 Conclusion

In my thesis I investigated the spatial and temporal variability of the stress field of the earth's crust by means of data compilation, 3D geomechanical-numerical modelling, and 3D thermo-hydro-mechanical (THM) modelling. I presented the first comprehensive stress survey from different kinds of stress indicators in Iceland which is a geologically very young country on an onshore spreading ridge. This compilation revealed a distinct stress field even close to the plate boundary. Then I developed the multi-stage 3D geomechanical-numerical modelling approach to derive a continuous 3D estimation of the in-situ stress field across scales from point-wise data records. Finally, I investigated the driving factors of the observed injection induced transient stress tensor rotations by means of a generic 3D THM model. The most important findings of my thesis are:

(1) I developed and presented the 3D multi-stage modelling approach for geomechanical-numerical modelling which allows calibrating a local reservoir in-situ stress model on the stress state from a larger scale model. This makes it possible to estimate a calibrated highly detailed in-situ stress state in an area in which no data records are available.

(2) I quantified the uncertainties that are related to the 3D geomechanical-numerical modelling and showed that the main contributions originate from uncertain material properties and the low number of stress magnitude data for model calibration. This enables the focused mitigation of uncertainties in the model results by the specific designation of their causes.

(3) I investigated the mechanism and key driving factors of injection induced stress tensor rotation and found that reservoir permeability, injection rate, and initial differential stress are the controlling parameters. Thus, if a stress rotation is observed and permeability and injection rate are known, the initial differential stress can be derived. More importantly, knowledge of the mechanism of stress rotation can be used to mitigate the potential for induced seismicity on pre-existing faults.

A key challenge for future research is to reduce the model uncertainties in order to enhance the reliability of the model results. To achieve this, the uncertainties of rock properties have to be lowered and the number and quality of stress magnitude data has to be increased. A major step forward will be the further development of the stress magnitude database Quantitative World Stress Map (Q-WSM). Further research should also focus on the influence of the reservoir geometry, anisotropies in the material, and engineering parameters on model results. These parameters have a large influence on the in-situ stress state and the potential for stress rotation and therefore the occurrence of induced seismicity.

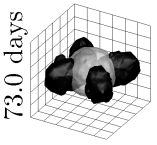

References

Aadnoy, B. and Bell, J. (1998). Classification of drilling-induced fractures and their relationship to in-situ stress directions. *The Log Analyst*, 39:27–42.

Aadnoy, B. S. (1990). Inversion technique to determine the in-situ stress field from fracturing data. *Journal of Petroleum Science and Engineering*, 4(2):127–141.

Albaric, J., Oye, V., Langet, N., Hasting, M., Lecomte, I., Iranpour, K., Messeiller, M., and Reid, P. (2014). Monitoring of induced seismicity during the first geothermal reservoir stimulation at Paralana, Australia. *Geothermics*, 52:120–131.

Allen, R. M., Nolet, G., Morgan, W. J., Vogfjörd, K., Nettles, M., Ekström, G., Bergsson, B. H., Erlendsson, P., Foulger, G., Jakobsdóttir, S., Julian, B. R., Pritchard, M., Ragnarsson, S., and Stefánsson, R. (2002). Plume-driven plumbing and crustal formation in Iceland. *Journal of Geophysical Research*, 107(B8):2163–2182.

Altmann, J., Müller, B., Müller, T., Heidbach, O., Tingay, M., and Weißhardt, A. (2014). Pore pressure stress coupling in 3D and consequences for reservoir stress states and fault reactivation. *Geothermics*, 52:195–204.

Altmann, J. B., Müller, T. M., Müller, B. I., Tingay, M. R., and Heidbach, O. (2010). Poroelastic contribution to the reservoir stress path. *International Journal of Rock Mechanics and Mining Sciences*, 47(7):1104–1113.

Amadei, B. and Stephansson, O. (1997). *Rock Stress and Its Measurement*. Springer Netherlands, Dordrecht.

Amante, C. and Eakins, B. (2009). ETOPO1 – 1 Arc-Minute Global Relief Model: Procedures, Data Sources and Analysis. *NOAA Technical Memorandum NESDIS NGDC-24. National Geophysical Data Center, NOAA*.

Anderson, E. (1905). The dynamics of faulting. *Transactions of the Edinburgh Geological Society*, 8:387–402.

Anderson, E. (1951). *The dynamics of faulting*. Oliver and Boyd, Edinburgh, 2nd edition.

Andrew, R. E. and Gudmundsson, A. (2008). Volcanoes as elastic inclusions: Their effects on the propagation of dykes, volcanic fissures, and volcanic zones in Iceland. *Journal of Volcanology and Geothermal Research*, 177(4):1045–1054.

Angelier, J. (1979). Determination of the mean principal directions of stresses for a given fault population. *Tectonophysics*, 56(3-4):T17–T26.

Angelier, J. (1984). Tectonic analysis of fault slip data sets. *Journal of Geophysical Research*, 89(B7):5835–5848.

Angelier, J., Bergerat, F., Stefánsson, R., and Bellou, M. (2008). Seismotectonics of a newly formed transform zone near a hotspot: Earthquake mechanisms and regional stress in the South Iceland Seismic Zone. *Tectonophysics*, 447(1-4):95–116.

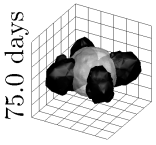

Angelier, J., Slunga, R., Bergerat, F., Stefánsson, R., and Homberg, C. (2004). Perturbation of stress and oceanic rift extension across transform faults shown by earthquake focal mechanisms in Iceland. *Earth and Planetary Science Letters*, 219(3-4):271–284.

Angenheister, G. (1982). Physical properties of rocks. In Angenheister, G., editor, *Landolt-Börnstein – Group V Geophysics – Subvolume A*. Springer-Verlag.

Árnadóttir, T., Jónsson, S., Pedersen, R., and Gudmundsson, G. B. (2003). Coulomb stress changes in the South Iceland Seismic Zone due to two large earthquakes in June 2000. *Geophysical Research Letters*, 30(5):1205.

Árnadóttir, T., Lund, B., Jiang, W., Geirsson, H., Björnsson, H., Einarsson, P., and Sigurdsson, T. (2009). Glacial rebound and plate spreading: results from the first countrywide GPS observations in Iceland. *Geophysical Journal International*, 177(2):691–716.

Arndt, D., Bär, K., Fritsche, J.-G., Kracht, M., Sass, I., and Hoppe, A. (2011). 3D structural model of the Federal State of Hesse (Germany) for geopotential evaluation [Geologisches 3D-Modell von Hessen zur Bestimmung von Geo-Potenzialen]. *Zeitschrift der Deutschen Gesellschaft für Geowissenschaften*, 162(4):353–369.

Ásmundsson, R., Pezard, P., Sanjuan, B., Henninges, J., Deltombe, J.-L., Halladay, N., Lebert, F., Gadalia, A., Millot, R., Gibert, B., Violay, M., Reinsch, T., Naisse, J.-M., Massiot, C., Azaïs, P., Mainprice, D., Karytsas, C., and Johnston, C. (2014). High temperature instruments and methods developed for supercritical geothermal reservoir characterisation and exploitation - The HiTI project. *Geothermics*, 49:90–98.

Bachmann, G., Müller, M., and Weggen, K. (1987). Evolution of the Molasse Basin (Germany, Switzerland). *Tectonophysics*, 137:77–92.

Bachmann, G. H., Dohr, G., and Mueller, M. (1982). Exploration in a classic thrust belt and its foreland: Bavarian Alps, Germany. *AAPG Bulletin*, 66(12):2529–2542.

Bada, G., Horváth, F., Dövényi, P., Szafián, P., Windhoffer, G., and Cloetingh, S. (2007). Present-day stress field and tectonic inversion in the Pannonian basin. *Global and Planetary Change*, 58(1-4):165–180.

Baisch, S., Rothert, E., Stang, H., Vörös, R., Koch, C., and McMahon, A. (2015). Continued geothermal reservoir stimulation experiments in the Cooper Basin (Australia). *Bulletin of the Seismological Society of America*.

Bär, K., Reinsch, T., Sippel, J., Freymark, J., Mielke, P., Strom, A., and Wiesner, P. (2015). Internationale Datenbank petrophysikalischer Kennwerte - Grundlage zur Reservoircharakterisierung. In *Der Geothermiekongress 2015*.

Bär, K., Reinsch, T., Sippel, J., Strom, A., Mielke, P., and Sass, I. (2017). P^3-international petrophysical property database. In *42nd Workshop on Geothermal Reservoir Engineering*, pages 1–6. Stanford University, Stanford, California.

Baria, R., Jung, R., Tischner, T., Nicholls, J., Michelet, S., Sanjuan, B., Soma, N., Asanuma, H., Dyer, B., and Garnish, J. (2006). Creation of an HDR reservoir at 5000 m depth at the European HDR project. In *31st Workshop on Geothermal Reservoir Engineering*, pages 1–8, Stanford, United States. Stanford University, Stanford, California.

Barth, A., Reinecker, J., and Heidbach, O. (2008). Stress derivation from earthquake focal mechanisms. Technical report, World Stress Map Project.

Barton, C. A., Zoback, M. D., and Moos, D. (1995). Fluid flow along potentially active faults in crystalline rock. *Geology*, 23(8):683–686.

Batir, J. (2011). Stress field characterization of the Hellisheiði geothermal field and possibilities to improve injection capabilities. Master thesis, RES - The School for Renewable Energy Science.

Bear, J. (1972). *Dynamics of Fluids in Porous Media*. Dover Publishing inc.

Bell, J. (1996). In situ stresses in sedimentary rocks (Part 1): Measurement Techniques. *Geoscience Canada*, 23(2):85–100.

Bell, J. and Gough, D. (1979). Northeast-southwest compressive stress in Alberta - evidence from oil wells. *Earth and Planetary Science Letters*, 45(2):475–482.

Bell, J. S. (1990). Investigating stress regimes in sedimentary basins using information from oil industry wireline logs and drilling records. *Geological Society, London, Special Publications*, 48(1):305–325.

Bergerat, F. and Angelier, J. (1998). Fault systems and paleostresses in the Vestfirdir Peninsula. Relationships with the Tertiary paleo-rifts of Skagi and Snaefells (Northwest Iceland). *Geodinamica Acta*, 11(2-3):105–118.

Bergerat, F. and Angelier, J. (2001). Mechanisms of the faults of 17 and 21 June 2000 earthquakes in the South Iceland Seismic Zone from the surface traces of the Árnes and Hestfjall faults. *Comptes Rendus de l'Académie des Sciences - Series IIA - Earth and Planetary Science*, 333(1):35–44.

Bergerat, F., Angelier, J., and Villemin, T. (1990). Fault systems and stress patterns on emerged oceanic ridges: a case study in Iceland. *Tectonophysics*, 179(3-4):183–197.

Bergerat, F., Gudmundsson, A., Angelier, J., and Rögnvaldsson, S. (1998). Seismotectonics of the central part of the South Iceland Seismic Zone. *Tectonophysics*, 298(4):319–335.

Bergerat, F. and Plateaux, R. (2012). Architecture and development of (Pliocene to Holocene) faults and fissures in the East Volcanic Zone of Iceland. *Comptes Rendus Geoscience*, 344(3-4):191–204.

Bird, P. (2003). An updated digital model of plate boundaries. *Geochemistry, Geophysics, Geosystems*, 4(3):1–52.

Bjarnason, I. T. and Einarsson, P. (1991). Source mechanism of the 1987 Vatnafjöll earthquake in South Iceland. *Journal of Geophysical Research*, 96(B3):4313–4324.

Björnsson, H. and Einarsson, P. (1990). Volcanoes beneath Vatnajökull, Iceland: Evidence from radio echo-sounding, earthquakes and jökulhlaups. *Jökull*, 40:147–168.

Blöcher, M., Zimmermann, G., Moeck, I., Brandt, W., Hassanzadegan, A., and Magri, F. (2010). 3D numerical modeling of hydrothermal processes during the lifetime of a deep geothermal reservoir. *Geofluids*, 10(3):406–421.

Bohnhoff, M., Baisch, S., and Harjes, H.-P. (2004). Fault mechanisms of induced seismicity at the superdeep German Continental Deep Drilling Program (KTB) borehole and their relation to fault structure and stress field. *Journal of Geophysical Research: Solid Earth*, 109(B2):B02309.

Bohnhoff, M., Grosser, H., and Dresen, G. (2006). Strain partitioning and stress rotation at the North Anatolian fault zone from aftershock focal mechanisms of the 1999 Izmit M w = 7.4 earthquake. *Geophysical Journal International*, 166(1):373–385.

Bond, C., Johnson, G., and Ellis, J. (2015). Structural model creation: the impact of data type and creative space on geological reasoning and interpretation. *Geological Society, London, Special Publications*, 421(1):83–97.

Bott, M. H. P. (1959). The Mechanics of Oblique Slip Faulting. *Geological Magazine*, 96(02):109–117.

Brady, B. and Brown, E. (2004). *Rock Mechanics for Underground Mining*. Kluwer Academic Publishers, Dodrecht Boston London, 3rd edition.

Brown, D. (2009). Hot dry rock geothermal energy: important lessons from Fenton Hill. In *34th Workshop on Geothermal Reservoir Engineering*, pages 1–4, Stanford, California. Stanford University, Stanford, California.

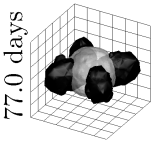

Brown, E. E. and Hoek, E. (1978). Trends in relationships between measured in-situ stresses and depth. *International Journal of Rock Mechanics and Mining Sciences & Geomechanics Abstracts*, 15(4):211–215.

Brudy, M., Zoback, M. D., Fuchs, K., Rummel, F., and Baumgärtner, J. (1997). Estimation of the complete stress tensor to 8 km depth in the KTB scientific drill holes: Implications for crustal strength. *Journal of Geophysical Research*, 102(B8):18453–18475.

Bruel, D. (2002). Impact of Induced Thermal Stresses During Circulation Tests in an Engineered Fractured Geothermal Reservoir: Example of the Soultz-Sous-Forêts European Hot Fractured Rock Geothermal Project, Rhine Graben, France. *Oil & Gas Science and Technology*, 57(5):459–470.

Buchmann, T. and Connolly, P. (2007). Contemporary kinematics of the Upper Rhine Graben: A 3D finite element approach. *Global and Planetary Change*, 58(1-4):287–309.

Bundesverband Geothermie (2015). Stadtwerke München: Seismologische Untersuchungen im Großraum München. `http://www.geothermie.de/news-anzeigen/2015/08/27/stadtwerke-munchen-seismologische-untersuchungen-im-grossraum-munchen.html`. Accessed: 10.06.2016.

Bundesverband Geothermie (2016). Tiefe Geothermie in Deutschland. `http://www.geothermie.de/fileadmin/useruploads/wissenswelt/Projekte/Projektliste_Tiefe_Geothermie_2016.pdf`. Accessed: 10.06.2016.

Byerlee, J. (1978). Friction of rocks. *Pure and Applied Geophysics PAGEOPH*, 116(4-5):615–626.

Cacace, M., Blöcher, G., Watanabe, N., Moeck, I., Börsing, N., Scheck-Wenderoth, M., Kolditz, O., and Huenges, E. (2013). Modelling of fractured carbonate reservoirs: outline of a novel technique via a case study from the Molasse Basin, southern Bavaria, Germany. *Environmental Earth Sciences*, 70(8):3585–3602.

Cacas, M., Daniel, J., and Letouzey, J. (2001). Nested geological modelling of naturally fractured reservoirs. *Petroleum Geoscience*, 7(S):43–52.

Cai, M. (2008). Influence of stress path on tunnel excavation response - numerical tool selection and modelling strategy. *Tunnelling and Underground Space Technology*, 23(6):618–628.

Cauchy, A. L. (1827). De la pression ou tension dans un corps solide. In *Exercices de Mathématiques, Volume 2*, page 42. De Bure frères, Gent.

Célérier, B. (2010). Remarks on the relationship between the tectonic regime, the rake of the slip vectors, the dip of the nodal planes, and the plunges of the P, B, and T axes of earthquake focal mechanisms. *Tectonophysics*, 482(1-4):42–49.

Chang, K. W. and Segall, P. (2016). Injection-induced seismicity on basement faults including poroelastic stressing. *Journal of Geophysical Research: Solid Earth*, 121(4):2708–2726.

Clauser, C., Koch, A., Hartmann, A., Rath, V., Mottaghy, D., and Pechnig, R. (2007). Erstellung statistisch abgesicherter thermischer und hydraulischer Gesteinseigenschaften für den flachen und tiefen Untergrund in Deutschland Phase 1 – Westliche Molasse und nördlich angrenzendes Süddeutsches Schichtstufenland. Technical report, Final Report for BMU-Project FKZ 0329985, Aachen.

Clifton, A. E. and Kattenhorn, S. A. (2006). Structural architecture of a highly oblique divergent plate boundary segment. *Tectonophysics*, 419(1):27–40.

Coblentz, D. D. and Richardson, R. M. (1995). Statistical trends in the intraplate stress field. *Journal of Geophysical Research: Solid Earth*, 100(B10):20245–20255.

Coblentz, D. D., Zhou, S., Hillis, R. R., Richardson, R. M., and Sandiford, M. (1998). Topography, boundary forces, and the Indo-Australian intraplate stress field. *Journal of Geophysical Research*, 103(B1):919–931.

Connolly, P. and Cosgrove, J. (1999). Prediction of static and dynamic fluid pathways within and around dilational jogs. *Geological Society, London, Special Publications*, 155(1):105–121.

Cornet, F., Helm, J., Poitrenaud, H., and Etchecopar, A. (1997). Seismic and aseismic slips induced by large-scale fluid injections. In *Seismicity Associated with Mines, Reservoirs and Fluid Injections*, pages 563–583. Springer.

Cornet, F. and Magnenet, V. (2016). A non-tectonic origin for the present day stress field in the sedimentary Paris Basin. In *EGU General Assembly Conference Abstracts*, volume 18, page 1939.

Cornet, F. H. (2015). *Elements of Crustal Geomechanics*. Cambridge University Press.

Cornet, F. H. and Röckel, T. (2012). Vertical stress profiles and the significance of "stress decoupling". *Tectonophysics*, 581:193–205.

Corthésy, R., He, G., Gill, D. D., and Leite, M. M. (1999). A stress calculation model for the 3D borehole slotter. *International Journal of Rock Mechanics and Mining Sciences*, 36(4):493–508.

Crampin, S. and Peacock, S. (2005). A review of shear-wave splitting in the compliant crack-critical anisotropic earth. *Wave motion*, 41(1):59–77.

Dahm, T., Becker, D., Bischoff, M., Cesca, S., Dost, B., Fritschen, R., Hainzl, S., Klose, C. D., Kühn, D., Lasocki, S., Meier, T., Ohrnberger, M., Rivalta, E., Wegler, U., and Husen, S. (2012). Recommendation for the discrimination of human-related and natural seismicity. *Journal of Seismology*, 17(1):197–202.

Dahm, T., Hainzl, S., and Becker, D. (2010). How to discriminate induced, triggered and natural seismicity. In *Proceedings of the Workshop Induced Seismicity*, pages 69–76, Luxembourg. Centre Européen de Géodynamique et de Séismologie.

de la Varga, M., Wellmann, F., and Murdie, R. (2015). Adding geological knowledge to improve uncertain geological models: a Bayesian perspective. *Geotectonic Research*, 97(1):18–20.

Deichmann, N. and Ernst, J. (2009). Earthquake focal mechanisms of the induced seismicity in 2006 and 2007 below Basel (Switzerland). *Swiss Journal of Geosciences*, 102(3):457–466.

Dieterich, J., Cayol, V., and Okubo, P. (2000). The use of earthquake rate changes as a stress meter at Kilauea volcano. *Nature*, 408(6811):457–460.

Dorbath, L., Cuenot, N., Genter, A., and Frogneux, M. (2009). Seismic response of the fractured and faulted granite of Soultz-sous-Forêts (France) to 5 km deep massive water injections. *Geophysical Journal International*, 177(2):653–675.

Dreger, D. S., Boyd, O. S., and Gritto, R. (2017). Automatic moment tensor analyses, in-situ stress estimation and temporal stress changes at The Geysers EGS demonstration project. In *42nd Workshop on Geothermal Reservoir Engineering*, pages 1–10, Stanford. Stanford University, Stanford, California.

Dziewonski, A. M. M., Chou, T.-A., and Woodhouse, J. H. (1981). Determination of earthquake source parameters from waveform data for studies of global and regional seismicity. *Journal of Geophysical Research*, 86(B4):2825–2852.

Einarsson, P. (1979). Seismicity and earthquake focal mechanisms along the Mid-Atlantic plate boundary between Iceland and the Azores. *Tectonophysics*, 55(1-2):127–153.

Einarsson, P. (1987). Compilation of earthquake fault plane solutions in the North Atlantic and Arctic Oceans. In *Recent plate movements and deformation*, pages 47–62. Wiley-Blackwell.

Einarsson, P. (1991). Earthquakes and present-day tectonism in Iceland. *Tectonophysics*, 189(1-4):261–279.

Einarsson, P. (2008). Plate boundaries, rifts and transforms in Iceland. *Jökull*, 58:35–58.

Einarsson, P. (2010). Mapping of Holocene surface ruptures in the South Iceland Seismic Zone. *Jökull*, 60:121–138.

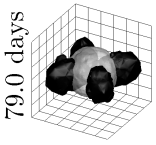

Einarsson, P., Klein, F., and Björnsson, S. (1977). The Borgarfjördur earthquakes of 1974 in West Iceland. *Bulletin of the Seismological Society of America*, 67(1):187–208.

Ekström, G. (1994). Anomalous earthquakes on volcano ring-fault structures. *Earth and Planetary Science Letters*, 128(3-4):707–712.

Ekström, G., Nettles, M., and Dziewonski, A. (2012). The Global CMT Project 2004 - 2010: Centroid-moment tensors for 13,017 earthquakes. *Physics of the Earth and Planetary Interiors*, 200-201:1–9.

Ellis, D. V. and Singer, J. M. (2010). *Well Logging for Earth Scientists*. Springer.

Ellsworth, W. L. (2013). Injection-induced earthquakes. *Science*, 341(6142):1225942–1225942.

Evans, K. F., Zappone, A., Kraft, T., Deichmann, N., and Moia, F. (2012). A survey of the induced seismic responses to fluid injection in geothermal and CO2 reservoirs in Europe. *Geothermics*, 41:30–54.

Fabriol, H., Rivas, J., Handal, S., and Correia, H. (1998). Microseismicity and geothermal exploitation of berlin (el salvador). *Geothermal Resources Council Transactions*, 22:159–163.

Farr, T. G., Rosen, P. A., Caro, E., Crippen, R., Duren, R., Hensley, S., Kobrick, M., Paller, M., Rodriguez, E., Roth, L., Seal, D., Shaffer, S., Shimada, J., Umland, J., Werner, M., Oskin, M., Burbank, D., and Alsdorf, D. (2007). The shuttle radar topography mission. *Reviews of geophysics*, 45(45).

Fischer, K. and Henk, A. (2013). A workflow for building and calibrating 3-D geomechanical models - a case study for a gas reservoir in the North German Basin. *Solid Earth*, 4(2):347–355.

Flóvenz, Ó. G., Ágústsson, K., Guðnason, E. Á., and Kristjánsdóttir, S. (2015). Reinjection and Induced Seismicity in Geothermal Fields in Iceland. In *Proceedings World Geothermal Congress 2015*, pages 1–15, Melbourne, Australia. International Geothermal Association.

Forslund, T. and Gudmundsson, A. (1991). Crustal spreading due to dikes and faults in southwest Iceland. *Journal of Structural Geology*, 13(4):443–457.

Freymark, J., Sippel, J., Scheck-Wenderoth, M., Bär, K., Stiller, M., Fritsche, J.-G., and Kracht, M. (2017). The deep thermal field of the Upper Rhine Graben. *Tectonophysics*, 694:114–129.

Fritzer, T., Settles, E., and Dorsch, K. (2012). Bayerischer Geothermieatlas. Technical report, Bayerisches Staatsministerium für Wirtschaft, Infrastruktur, Verkehr und Technologie, München.

Fuchs, K. and Müller, B. (2001). World stress map of the Earth: A key to tectonic processes and technological applications. *Naturwissenschaften*, 88(9):357–371.

Funato, A., Ito, T., and Shono, T. (2012). Laboratory verification of the diametrical core deformation analysis (dcda) developed for in-situ stress measurements. In *46th US Rock Mechanics/Geomechanics Symposium*. American Rock Mechanics Association.

Garcia, S. (2003). *Implications d'un saut de rift et du fonctionnement d'une zone transformante sur les deformations du nord de l'Islande*. Phd thesis, Université Pierre et Marie Curie.

Garcia, S., Angelier, J., Bergerat, F., and Homberg, C. (2002). Tectonic analysis of an oceanic transform fault zone based on fault-slip data and earthquake focal mechanisms: the Húsavík-Flatey Fault zone, Iceland. *Tectonophysics*, 344(3-4):157–174.

Garcia, S. and Dhont, D. (2005). Structural analysis of the Húsavík-Flatey transform fault and its relationships with the rift system in Northern Iceland. *Geodinamica Acta*, 18(1):31–41.

Gaucher, E., Schoenball, M., Heidbach, O., Zang, A., Fokker, P. A., van Wees, J.-D., and Kohl, T. (2015). Induced seismicity in geothermal reservoirs: A review of forecasting approaches. *Renewable and Sustainable Energy Reviews*, 52:1473–1490.

Geirsson, H., Árnadóttir, T., Völksen, C., Jiang, W., Sturkell, E., Villemin, T., Einarsson, P., Sigmundsson, F., and Stefánsson, R. (2006). Current plate movements across the Mid-Atlantic Ridge determined from 5 years of continuous GPS measurements in Iceland. *Journal of Geophysical Research*, 111(B9):B09407.

GEOFON Data Centre (1993). GEOFON Seismic Network. Other/Seismic Network, `http://geofon.gfz-potsdam.de/`.

Gephart, J. W. and Forsyth, D. W. (1984). An improved method for determining the regional stress tensor using earthquake focal mechanism data: Application to the San Fernando Earthquake Sequence. *Journal of Geophysical Research*, 89(B11):9305–9320.

Giorgi, F., Mearns, L. O., Shields, C., and McDaniel, L. (1998). Regional nested model simulations of present day and 2×CO2 climate over the central plains of the US. *Climatic Change*, 40(3-4):457–493.

Gölke, M. and Coblentz, D. (1996). Origins of the European regional stress field. *Tectonophysics*, 266(1-4):11–24.

Green, R. G., White, R. S., and Greenfield, T. (2014). Motion in the north Iceland volcanic rift zone accommodated by bookshelf faulting. *Nature Geoscience*, 7(1):29–33.

Gritto, R. and Jarpe, S. P. (2014). Temporal variations of Vp/Vs-ratio at The Geysers geothermal field, USA. *Geothermics*, 52:112–119.

Grünthal, G. (2011). *Earthquakes, intensity*, chapter 5: E, pages 237–242. Springer-Verlag GmbH, 1st edition.

Grünthal, G. (2014). Induced seismicity related to geothermal projects versus natural tectonic earthquakes and other types of induced seismic events in Central Europe. *Geothermics*, 52:22–35.

Grünthal, G. and Stromeyer, D. (1992). The recent crustal stress field in central Europe: trajectories and finite element modeling. *Journal of Geophysical Research*, 97(B8):11805–11820.

Grünthal, G. and Wahlström, R. (2012). The European-Mediterranean earthquake catalogue (EMEC) for the last millennium. *Journal of Seismology*, 16(3):535–570.

Gudmundsson, A. (1987). Tectonics of the Thingvellir fissure swarm, SW Iceland. *Journal of Structural Geology*, 9(1):61–69.

Gudmundsson, A. (1995). Infrastructure and mechanics of volcanic systems in Iceland. *Journal of Volcanology and Geothermal Research*, 64(1-2):1–22.

Gudmundsson, A. (2002). Emplacement and arrest of sheets and dykes in central volcanoes. *Journal of Volcanology and Geothermal Research*, 116(3):279–298.

Gudmundsson, A. (2003). Surface stresses associated with arrested dykes in rift zones. *Bulletin of Volcanology*, 65(8):606–619.

Gudmundsson, A. (2006). How local stresses control magma-chamber ruptures, dyke injections, and eruptions in composite volcanoes. *Earth-Science Reviews*, 79(1-2):1–31.

Gudmundsson, A., Bergerat, F., and Angelier, J. (1996). Off-rift and rift-zone palaeostresses in Northwest Iceland. *Tectonophysics*, 255(3-4):211–228.

Gudmundsson, A., Bergerat, F., Angelier, J., and Villemin, T. (1992). Extensional tectonics of southwest Iceland. *Bulletin de la Societe Geologique de France*, 163(5):561–570.

Gunzburger, Y. and Cornet, F. H. (2007). Rheological characterization of a sedimentary formation from a stress profile inversion. *Geophysical Journal International*, 168(1):402–418.

Gunzburger, Y. and Magnenet, V. (2014). Stress inversion and basement-cover stress transmission across weak layers in the Paris Basin, France. *Tectonophysics*, 617:44–57.

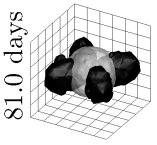

Haflidason, H., Eiriksson, J., and Kreveld, S. V. (2000). The tephrochronology of Iceland and the North Atlantic region during the Middle and Late Quaternary: a review. *Journal of Quaternary Science*, 15(1):3–22.

Hagos, L., Shomali, H., Lund, B., Böðvarsson, R., and Roberts, R. (2008). An Application of Relative Moment Tensor Inversion to Aftershocks of the June 1998 Hengill Earthquake in Southwest Iceland. *Bulletin of the Seismological Society of America*, 98(2):636–650.

Haimson, B. and Fairhurst, C. (1969). In-situ stress determination at great depth by means of hydraulic fracturing. In *The 11th US Symposium on Rock Mechanics (USRMS)*. American Rock Mechanics Association.

Haimson, B. and Rummel, F. (1982). Hydrofracturing stress measurements in the Iceland research drilling project drill hole at Reyðarfjörður, Iceland. *Journal of Geophysical Research*, 87(B8):6631–6649.

Haimson, B. and Voight, B. (1977). Crustal stress in Iceland. *Pure and Applied Geophysics*, 115:153–190.

Hardebeck, J. (2010). Aftershocks are well aligned with the background stress field, contradicting the hypothesis of highly heterogeneous crustal stress. *Journal of Geophysical Research*, 115(B12):B12308.

Hardebeck, J. L. (2012). Coseismic and postseismic stress rotations due to great subduction zone earthquakes. *Geophysical Research Letters*, 39(21).

Hardebeck, J. L. (2014). The impact of static stress change, dynamic stress change, and the background stress on aftershock focal mechanisms. *Journal of Geophysical Research: Solid Earth*, 119:1–28.

Hardebeck, J. L. and Hauksson, E. (2001). Crustal stress field in southern California and its implications for fault mechanics. *Journal of Geophysical Research: Solid Earth*, 106(B10):21859–21882.

Hardebeck, J. L. and Michael, A. J. (2006). Damped regional-scale stress inversions: Methodology and examples for southern California and the Coalinga aftershock sequence. *Journal of Geophysical Research: Solid Earth*, 111(B11):B11310.

Hardebeck, J. L., Nazareth, J. J., and Hauksson, E. (1998). The static stress change triggering model: Constraints from two southern California aftershock sequences. *Journal of Geophysical Research*, 103(B10):24427–24437.

Häring, M. O., Schanz, U., Ladner, F., and Dyer, B. C. (2008). Characterisation of the Basel 1 enhanced geothermal system. *Geothermics*, 37(5):469–495.

Harris, R. A. (1998). Introduction to Special Section: Stress Triggers, Stress Shadows, and Implications for Seismic Hazard. *Journal of Geophysical Research*, 103(B10):24347–24358.

Hast, N. (1969). The state of stress in the upper part of the earth's crust. *Tectonophysics*, 8(3):169–211.

Hast, N. (1973). Global Measurements of Absolute Stress. *Philosophical Transactions of the Royal Society A: Mathematical, Physical and Engineering Sciences*, 274(1239):409–419.

Heidbach, O. (2016). Scientific Technical Report 16-01 – WSM quality ranking scheme, database description and analysis guidelines for stress indicator. `http://www.world-stress-map.org/fileadmin/wsm/pdfs/WSM_STR_16_01.pdf`. Accessed: 07.04.2017.

Heidbach, O. and Ben-Avraham, Z. (2007). Stress evolution and seismic hazard of the Dead Sea Fault System. *Earth and Planetary Science Letters*, 257(1-2):299–312.

Heidbach, O. and Höhne, J. (2008). CASMI – A visualization tool for the World Stress Map database. *Computers & Geosciences*, 34(7):783–791.

Heidbach, O., Rajabi, M., Reiter, K., Ziegler, M., and the WSM Team (2016a). *World Stress Map Database Release 2016*. GFZ Data Services.

Heidbach, O., Rajabi, M., Ziegler, M., Reiter, K., and Team, W. (2016b). The World Stress Map Database Release 2016 - Global Crustal Stress Pattern vs. Absolute Plate Motion. *Geophysical Research Abstracts*, 18:4861.

Heidbach, O. and Reinecker, J. (2013). Analyse des rezenten Spannungsfeldes der Nordschweiz. Nagra Arb. Ber. NAB 12-05, Nagra, Wettingen.

Heidbach, O., Reinecker, J., Tingay, M., Müller, B., Sperner, B., Fuchs, K., and Wenzel, F. (2007). Plate boundary forces are not enough: Second- and third-order stress patterns highlighted in the World Stress Map database. *Tectonics*, 26(6):1–19.

Heidbach, O., Tingay, M., Barth, A., Reinecker, J., Kurfeß, D., and Müller, B. (2008). The 2008 release of the World Stress Map.

Heidbach, O., Tingay, M., Barth, A., Reinecker, J., Kurfeß, D., and Müller, B. (2010). Global crustal stress pattern based on the World Stress Map database release 2008. *Tectonophysics*, 482(1-4):3–15.

Hensch, M., Lund, B., Árnadóttir, T., and Brandsdóttir, B. (2015). Temporal stress changes associated with the 2008 May 29 MW 6 earthquake doublet in the western South Iceland Seismic Zone. *Geophysical Journal International*, 204(1):544–554.

Hergert, T. and Heidbach, O. (2011). Geomechanical model of the Marmara Sea region – II. 3-D contemporary background stress field. *Geophysical Journal International*, 185(3):1090–1102.

Hergert, T., Heidbach, O., Bécel, A., and Laigle, M. (2011). Geomechanical model of the Marmara Sea region – I. 3-D contemporary kinematics. *Geophysical Journal International*, 185(3):1073–1089.

Hergert, T., Heidbach, O., Reiter, K., Giger, S. B., and Marschall, P. (2015). Stress field sensitivity analysis in a sedimentary sequence of the Alpine foreland, northern Switzerland. *Solid Earth*, 6(2):533–552.

Hjartardóttir, A. R., Einarsson, P., Magnusdóttir, S., Björnsdóttir, T., and Brandsdóttir, B. (2015). Fracture systems of the Northern Volcanic Rift Zone, Iceland: an onshore part of the Mid-Atlantic plate boundary. *Geological Society, London, Special Publications*, 420(1):297–314.

Hjartardóttir, Á. R., Einarsson, P., and Sigurdsson, H. (2009). The fissure swarm of the Askja volcanic system along the divergent plate boundary of N Iceland. *Bulletin of Volcanology*, 71(9):961–975.

Hjartarson, Á. (2003). Postglacial lava production in Iceland. In *The Skagafjörður Unconformity, North Iceland, and its Geological History. PhD thesis*, pages 95–108. Geological Museum, University of Copenhagen, Copenhagen.

Hjartarson, Á. and Sæmundsson, K. (2014). Geologic Map of Iceland. Bedrock. 1 : 600 000. Technical report, Iceland GeoSurvey.

Hodgkinson, D. and Bourke, P. (1980). Initial assessment of the thermal stresses around a radioactive waste depository in hard rock. *Annals of Nuclear Energy*, 7(10):541–552.

Hoek, E. and Brown, E. (1980). *Underground excavations in rock*. Institution of Mining and Metallurgy, London.

Hornbach, M. J., DeShon, H. R., Ellsworth, W. L., Stump, B. W., Hayward, C., Frohlich, C., Oldham, H. R., Olson, J. E., Magnani, M. B., Brokaw, C., and Luetgert, J. H. (2015). Causal factors for seismicity near Azle, Texas. *Nature Communications*, 6:6728.

Hubbert, M. K. and Willis, D. G. (1972). *M 18: Underground Waste Management and Environmental Implications*, chapter Mechanics of Hydraulic Fracturing, pages 239–257. AAPG Special Volumes.

IAPWS (1997). *Revised Release on the IAPWS Industrial Formulation 1997 for the Thermodynamic Properties of Water and Steam*. International Association for the Properties of Water and Steam, Lucerne, Switzerland.

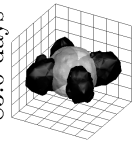

Ickrath, M., Bohnhoff, M., Dresen, G., Martínez-Garzón, P., Bulut, F., Kwiatek, G., and Germer, O. (2015). Detailed analysis of spatiotemporal variations of the stress field orientation along the Izmit-Düzce rupture in NW Turkey from inversion of first-motion polarity data. *Geophysical Journal International*, 202(3):2120–2132.

Illies, J. H. and Greiner, G. (1978). Rhinegraben and the Alpine system. *Geological Society of America Bulletin*, 89(5):770–782.

Ito, G., Lin, J., and Graham, D. (2003). Observational and theoretical studies of the dynamics of mantle plume-mid-ocean ridge interaction. *Reviews of Geophysics*, 41(4):1017.

Jacquey, A. B., Cacace, M., Blöcher, G., and Scheck-Wenderoth, M. (2015). Numerical investigation of thermoelastic effects on fault slip tendency during injection and production of geothermal fluids. *Energy Procedia*, 76:311–320.

Jaeger, J., Cook, N., and Zimmerman, R. (2007). *Fundamentals of Rock Mechanics*. Blackwell Publishing Ltd., Malden Oxford Carlton, 4th edition.

Jakobsdóttir, S. (2008). Seismicity in Iceland: 1994 – 2007. *Jökull*, 58:75–100.

Jakobsdóttir, S., Gudmundsson, G., and Stefánsson, R. (2002). Seismicity in Iceland 1991 – 2000 monitored by the SIL seismic system. *Jökull*, 51:87–94.

Jakobsson, S. (1979). Petrology of recent basalts of the Eastern Volcanic Zone, Iceland. *Acta Naturalia Islandica*, 26.

Jeanne, P., Rutqvist, J., Dobson, P. F., Garcia, J., Walters, M., Hartline, C., and Borgia, A. (2015). Geomechanical simulation of the stress tensor rotation caused by injection of cold water in a deep geothermal reservoir. *Journal of Geophysical Research: Solid Earth*, 120(12):8422–8438.

Jeanne, P., Rutqvist, J., Dobson, P. F., Walters, M., Hartline, C., and Garcia, J. (2014). The impacts of mechanical stress transfers caused by hydromechanical and thermal processes on fault stability during hydraulic stimulation in a deep geothermal reservoir. *International Journal of Rock Mechanics and Mining Sciences*, 72:149–163.

Jefferis, R. and Voight, B. (1981). Fracture analysis near the mid-ocean plate boundary, Reykjavík-Hvalfjörður area, Iceland. *Tectonophysics*, 76:171–236.

Jing, L. and Stephansson, O. (2007). *Fundamentals of Discrete Element Methods for Rock Engineering: Theory and Applications*, volume 85. Elsevier, 1st edition.

Jóhannesson, H. and Sæmundsson, K. (1998). Geological Map of Iceland, 1:500,000. Bedrock Geology. Technical report, Icelandic Institute of Natural History and Icelandic Geodetic Survey, Reykjavík.

Keiding, M., Lund, B., and Árnadóttir, T. (2009). Earthquakes, stress, and strain along an obliquely divergent plate boundary: Reykjanes Peninsula, southwest Iceland. *Journal of Geophysical Research*, 114(B9):B09306.

Kempka, T., Nielsen, C. M., Frykman, P., Shi, J.-Q., Bacci, G., and Dalhoff, F. (2014). Coupled Hydro-Mechanical Simulations of CO2 Storage Supported by Pressure Management Demonstrate Synergy Benefits from Simultaneous Formation Fluid Extraction. *Oil & Gas Science and Technology – Revue d'IFP Energies nouvelles*, 70(4):599–613.

Khodayar, M. and Franzson, H. (2007). Fracture pattern of Thjórsárdalur central volcano with respect to rift-jump and a migrating transform zone in South Iceland. *Journal of Structural Geology*, 29(5):898–912.

King, G., Stein, R., and Lin, J. (1994). Static stress changes and the triggering of earthquakes. *Bulletin of the Seismological Society of America*, 84(3):935–953.

Kirsch, E. G. (1898). Die Theorie der Elastizität und die Bedürfnisse der Festigkeitslehre. *Zeitschrift des Vereines Deutscher Ingenieure*, 42:797–807.

Kissling, W. and Weir, G. (2005). The spatial distribution of the geothermal fields in the Taupo Volcanic Zone, New Zealand. *Journal of Volcanology and Geothermal Research*, 145(1):136–150.

Koch, A. (2009). Erstellung statistisch abgesicherter thermischer und hydraulischer Gesteinseigenschaften für den flachen und tiefen Untergrund in Deutschland Phase 2 – Westliches Nordrhein-Westfalen und bayerisches Molassebecken. Technical report, RWTH Aaachen.

Koch, A. and Clauser, C. (2006). Erstellung statistisch abgesicherter thermischer und hydraulischer Gesteinseigenschaften für den flachen und tiefen Untergrund in Deutschland Phase 1 – Westliche Molasse und nördlich angrenzendes Süddeutsches Schichtstufenland. Technical report, RWTH Aachen, Aachen.

Kohl, T. and Mégel, T. (2007). Predictive modeling of reservoir response to hydraulic stimulations at the European EGS site Soultz-sous-Forêts. *International Journal of Rock Mechanics and Mining Sciences*, 44(8):1118–1131.

Kozłowska, M., Orlecka-Sikora, B., Kwiatek, G., Boettcher, M. S., and Dresen, G. (2015). Nanoseismicity and picoseismicity rate changes from static stress triggering caused by a M w 2.2 earthquake in Mponeng gold mine, South Africa. *Journal of Geophysical Research: Solid Earth*, 120(1):290–307.

Kristjánsdóttir, S. (2013). Microseismicity in the Krýsuvík Geothermal Field, SW Iceland, from May to October 2009. Master thesis, University of Iceland.

Kwiatek, G., Martínez-Garzón, P., Dresen, G., Bohnhoff, M., Sone, H., and Hartline, C. (2015). Effects of long-term fluid injection on induced seismicity parameters and maximum magnitude in northwestern part of The Geysers geothermal field. *Journal of Geophysical Research: Solid Earth*, 120(10):7085–7101.

Kwiatek, G., Plenkers, K., Nakatani, M., Yabe, Y., and Dresen, G. (2010). Frequency-Magnitude Characteristics Down to Magnitude -4.4 for Induced Seismicity Recorded at Mponeng Gold Mine, South Africa. *Bulletin of the Seismological Society of America*, 100(3):1165–1173.

Lama, R. D. and Vutukuri, V. S. (1978). *Handbook on mechanical properties of rocks - Testing Techniques and Results - Volume II*. Trans Tech Publications, Clausthal, 1st edition.

Lawver, L. and Müller, R. (1994). Iceland hotspot track. *Geology*, 22(4):311–314.

Leeman, E. R. (1964). The measurement of stress in rock - Part 2 - Borehole rock stress measuring instruments. *Journal of the South African Institut of Mining and Metallurgy*, 65(2):82–114.

Lemcke, K. (1988). *Geologie von Bayern I. - Das bayerische Alpenvorland vor der Eiszeit - Erdgeschichte - Bau - Bodenschätze*. E. Schweizerbart'sche Verlagsbuchhandlung (Nägele u. Obermiller), Stuttgart, 1st edition.

Ljunggren, C., Chang, Y., Janson, T., and Christiansson, R. (2003). An overview of rock stress measurement methods. *International Journal of Rock Mechanics and Mining Sciences*, 40(7-8):975–989.

Lund, B. and Bödvarsson, R. (2002). Correlation of Microearthquake Body-Wave Spectral Amplitudes. *Bulletin of the Seismological Society of America*, 92(6):2419–2433.

Lund, B. and Slunga, R. (1999). Stress tensor inversion using detailed microearthquake information and stability constraints: Application to Ölfus in southwest Iceland. *Journal of Geophysical Research*, 104(B7):14947–14964.

Lund, B. and Zoback, M. (1999). Orientation and magnitude of in situ stress to 6.5 km depth in the Baltic Shield. *International Journal of Rock Mechanics and Mining Sciences*, 36(2):169–190.

Magri, F., Tillner, E., Wang, W., Watanabe, N., Zimmermann, G., and Kempka, T. (2013). 3D hydromechanical scenario analysis to evaluate changes of the recent stress field as a result of geological CO2 storage. *Energy Procedia*, 40:375–383.

Majer, E. L., Baria, R., Stark, M., Oates, S., Bommer, J., Smith, B., and Asanuma, H. (2007). Induced seismicity associated with Enhanced Geothermal Systems. *Geothermics*, 36(3):185–222.

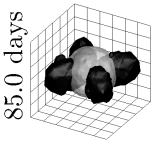

Mardia, K. (1972). *Statistics of Directional Data: Probability and Mathematical Statistics*. Academic Press, London.

Martin, C. D. (2007). Quantifying in situ stress magnitudes and orientations for Forsmark – Forsmark stage 2.2. techreport R-07-26, Svensk Kärnbränslehantering AB – Swedish Nuclear Fuel and Waste Management Co.

Martínez-Garzón, P., Ben-Zion, Y., Abolfathian, N., Kwiatek, G., and Bohnhoff, M. (2016). A refined methodology for stress inversions of earthquake focal mechanisms. *Journal of Geophysical Research: Solid Earth*, 121(12):8666–8687.

Martínez-Garzón, P., Bohnhoff, M., Kwiatek, G., and Dresen, G. (2013). Stress tensor changes related to fluid injection at The Geysers geothermal field, California. *Geophysical Research Letters*, 40(11):2596–2601.

Martínez-Garzón, P., Kwiatek, G., Ickrath, M., and Bohnhoff, M. (2014a). MSATSI: A MATLAB package for stress inversion combining solid classic methodology, a new simplified user-handling, and a visualization tool. *Seismological Research Letters*, 85(4):896–904.

Martínez-Garzón, P., Kwiatek, G., Sone, H., Bohnhoff, M., Dresen, G., and Hartline, C. (2014b). Spatiotemporal changes, faulting regimes, and source parameters of induced seismicity: A case study from The Geysers geothermal field. *Journal of Geophysical Research: Solid Earth*, 119(11):8378–8396.

Mastin, L. (1988). Effect of borehole deviation on breakout orientations. *Journal of Geophysical Research*, 93(B8):9187–9195.

Maury, J., Cornet, F. H., and Cara, M. (2014). Influence of the lithosphere-asthenosphere boundary on the stress field northwest of the Alps. *Geophysical Journal International*, 199(2):1006–1017.

Mavko, G., Mukerji, T., and Dvorkin, J. (2009). *The Rock Physics Handbook*. Cambridge University Press, New York, 2nd edition.

McClure, M. W. and Horne, R. N. (2014a). An investigation of stimulation mechanisms in Enhanced Geothermal Systems. *International Journal of Rock Mechanics and Mining Sciences*, 72:242–260.

McClure, M. W. and Horne, R. N. (2014b). Correlations between formation properties and induced seismicity during high pressure injection into granitic rock. *Engineering Geology*, 175:74–80.

McDougall, I., Kristjánsson, L., and Sæmundsson, K. (1984). Magnetostratigraphy and geochronology of northwest Iceland. *Journal of Geophysical Research*, 89(B8):7029–7060.

McGarr, A. (2014). Maximum magnitude earthquakes induced by fluid injection. *Journal of Geophysical Research: Solid Earth*, 119(2):1008–1019.

McGarr, A., Spottiswoode, S., and Gay, N. (1975). Relationship of mine tremors to induced stresses and to rock properties in the focal region. *Bulletin of the Seismological Society of America*, 65(4):981–993.

McKenzie, D. (1969). The relation between fault plane solutions for earthquakes and the directions of the principal stresses. *Bulletin of the Seismological Society of America*, 59(2):591–601.

McTigue, D. (1986). Thermoelastic response of fluid-saturated porous rock. *Journal of Geophysical Research: Solid Earth*, 91(B9):9533–9542.

Megies, T. and Wassermann, J. (2014). Microseismicity observed at a non-pressure-stimulated geothermal power plant. *Geothermics*, 52:36–49.

Michael, A. J. (1984). Determination of stress from slip data: Faults and folds. *Journal of Geophysical Research: Solid Earth*, 89(B13):11517–11526.

Michael, A. J. (1987). Use of focal mechanisms to determine stress: A control study. *Journal of Geophysical Research*, 92(B1):357–368.

Moeck, I. and Backers, T. (2011). Fault reactivation potential as a critical factor during reservoir stimulation. *First Break*, 29:73–80.

Moeck, I. S. (2014). Catalog of geothermal play types based on geologic controls. *Renewable and Sustainable Energy Reviews*, 37:867–882.

Moorbath, S., Sigurdsson, H., and Goodwin, R. (1968). K-Ar ages of the oldest exposed rocks in Iceland. *Earth and Planetary Science Letters*, 4(3):197–205.

Morris, A., Ferrill, D. A., and Henderson, D. B. (1996). Slip-tendency analysis and fault reactivation. *Geology*, 24(3):275.

Müller, B., Wehrle, V., Hettel, S., Sperner, B., and Fuchs, K. (2003). A new method for smoothing orientated data and its application to stress data. *Geological Society, London, Special Publications*, 209(1):107–126.

Müller, B., Wehrle, V., Zeyen, H., and Fuchs, K. (1997). Short-scale variations of tectonic regimes in the western European stress province north of the Alps and Pyrenees. *Tectonophysics*, 275(1-3):199–219.

Müller, B., Zoback, M., and Fuchs, K. (1992). Regional patterns of tectonic stress in Europe. *Journal of Geophysical Research : Solid Earth*, 97(B8):11783–11803.

Nakamura, K. (1977). Volcanoes as possible indicators of tectonic stress orientation - principle and proposal. *Journal of Volcanology and Geothermal Research*, 2:1–16.

Nakamura, K., Jacob, K. H., and Davies, J. N. (1977). Volcanoes as possible indicators of tectonic stress orientation - Aleutians and Alaska. *Pure and Applied Geophysics PAGEOPH*, 115(1-2):87–112.

Nettles, M. and Ekström, G. (1998). Faulting mechanism of anomalous earthquakes near Bárðarbunga Volcano, Iceland. *Journal of Geophysical Research*, 103(B8):17973–17983.

Oey, L.-Y. and Chen, P. (1992). A nested-grid ocean model: With application to the simulation of meanders and eddies in the Norwegian Coastal Current. *Journal of Geophysical Research: Oceans*, 97(C12):20063–20086.

Ogasawara, H., Sato, S., and Nishii, S. (2002). Semi-controlled seismogenic experiments in South African deep gold mines. *The Journal of the South African Institute of Mining and Metallurgy*, 102(4):243–250.

Orlecka-Sikora, B. (2010). The role of static stress transfer in mining induced seismic events occurrence, a case study of the Rudna mine in the Legnica-Glogow Copper District in Poland. *Geophysical Journal International*, 182(2):1087–1095.

Peška, P. and Zoback, M. D. (1995). Compressive and tensile failure of inclined well bores and determination of in situ stress and rock strength. *Journal of Geophysical Research*, 100(B7):12791–12811.

Pierdominici, S. and Heidbach, O. (2012). Stress field of Italy - Mean stress orientation at different depths and wave-length of the stress pattern. *Tectonophysics*, 532–535:301–311.

Plateaux, R., Bergerat, F., Béthoux, N., Villemin, T., and Gerbault, M. (2012). Implications of fracturing mechanisms and fluid pressure on earthquakes and fault slip data in the east Iceland rift zone. *Tectonophysics*, 581:19–34.

Plateaux, R., Béthoux, N., Bergerat, F., and Mercier de Lépinay, B. (2014). Volcano-tectonic interactions revealed by inversion of focal mechanisms: stress field insight around and beneath the Vatnajökull ice cap in Iceland. *Frontiers in Earth Science*, 2(May):1–21.

Plumb, R. A. and Cox, J. W. (1987). Stress directions in eastern North America determined to 4.5 km from borehole elongation measurements. *Journal of Geophysical Research: Solid Earth*, 92(B6):4805–4816.

Plumb, R. A. and Hickman, S. H. (1985). Stress-induced borehole elongation: A comparison between the four-arm dipmeter and the borehole televiewer in the Auburn Geothermal Well. *Journal of Geophysical Research*, 90(B7):5513–5521.

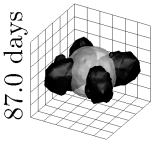

Przybycin, A. M. (2015). *Lithospheric-scale 3D structural and thermal modelling and the assessment of the origin of thermal anomalies in the European North Alpine Foreland Basin.* PhD thesis, Freie Universität Berlin.

Przybycin, A. M., Scheck-Wenderoth, M., and Schneider, M. (2015). The 3D conductive thermal field of the North Alpine Foreland Basin: influence of the deep structure and the adjacent European Alps. *Geothermal Energy*, 3(1):17.

Ragnarsson, Á. (2015). Geothermal Development in Iceland 2010-2014. In *Proceedings World Geothermal Congress 2015*, pages 1–15, Melbourne, Australia. International Geothermal Association.

Rajabi, M., Tingay, M., and Heidbach, O. (2016a). The present-day state of tectonic stress in the Darling Basin, Australia: implications for exploration and production. *Marine and Petroleum Geology*, 77:776–790.

Rajabi, M., Tingay, M., Heidbach, O., Hillis, R., and Reynolds, S. (2017). The present-day stress field of Australia. *Earth-Science Reviews*.

Rajabi, M., Tingay, M., King, R., and Heidbach, O. (2016b). Present-day stress orientation in the Clarence-Moreton Basin of New South Wales, Australia: A new high density dataset reveals local stress rotations. *Basin Research*, 29:622–640.

Rajabi, M., Ziegler, M., Tingay, M., Heidbach, O., and Reynolds, S. (2016c). Contemporary tectonic stress pattern of the Taranaki Basin, New Zealand. *Journal of Geophysical Research: Solid Earth*, 121:6053–6070.

Reasenberg, P. A. and Simpson, R. W. (1992). Response of regional seismicity to the static stress change produced by the Ioma Prieta earthquake. *Science*, 255(5052):1687–1690.

Reinecker, J., Tingay, M., Müller, B., and Heidbach, O. (2010). Present-day stress orientation in the Molasse Basin. *Tectonophysics*, 482(1-4):129–138.

Reiter, K. (2014). *Crustal stress variability across spatial scales - examples from Canada , Northern Switzerland and a South African gold mine.* phd thesis, Universität Potsdam.

Reiter, K. and Heidbach, O. (2014). 3-D geomechanical-numerical model of the contemporary crustal stress state in the Alberta Basin (Canada). *Solid Earth*, 5(2):1123–1149.

Reiter, K., Heidbach, O., Müller, B., Reinecker, J., and Röckl, T. (2016). Spannungskarte Deutschland 2016. `http://doi.org/10.5880/WSM.Germany2016`.

Reiter, K., Heidbach, O., Reinecker, J., Müller, B., and Röckel, T. (2015). Spannungskarte Deutschland 2015. *Erdöl Erdgas Kohle*, 131(11):437–442.

Reiter, K., Heidbach, O., Schmitt, D., Haug, K., Ziegler, M., and Moeck, I. (2014). A revised crustal stress orientation database for Canada. *Tectonophysics*, 636:111–124.

Richardson, R. M. (1992). Ridge forces, absolute plate motions, and the intraplate stress field. *Journal of Geophysical Research*, 97(B8):11739–11748.

Rider, M. and Kennedy, M. (2011). *The geological interpretation of well logs.* Rider-French Consulting Ltd., 3rd edition.

Rivera, L. and Cisternas, A. (1991). Stress tensor and fault plane solutions for a population of Earthquakes. *Bulletin of the Seismological Society of America*, 80(3):609–614.

Robertson, E. C. (1988). Thermal properties of rocks. Open File Report 88-441, United States Department of the Interior - Geological Survey, Reston, Virginia.

Roche, V., Homberg, C., David, C., and Rocher, M. (2014). Normal faults, layering and elastic properties of rocks. *Tectonophysics*, 622:96–109.

Roche, V. and van der Baan, M. (2017). Modeling of the in situ state of stress in elastic layered rock subject to stress and strain-driven tectonic forces. *Solid Earth*, 8(2):479–498.

Röckel, T. and Lempp, C. (2003). Der Spannungszustand im Norddeutschen Becken. *Erdöl Erdgas Kohle*, 119(2):73–80.

Rögnvaldsson, S. and Slunga, R. (1994). Single and joint fault plane solutions for microearthquakes in South Iceland. *Tectonophysics*, 237:73–80.

Roman, D. C., Moran, S., Power, J., and Cashman, K. (2004). Temporal and Spatial Variation of Local Stress Fields before and after the 1992 Eruptions of Crater Peak Vent, Mount Spurr Volcano, Alaska. *Bulletin of the Seismological Society of America*, 94(6):2366–2379.

Roth, F. and Fleckenstein, P. (2001). Stress orientations found in North-East Germany differ from the West European trend. *Terra Nova*, 13(4):289–296.

Roth, F., Henneberg, K., Fleckenstein, P., Palmer, J., Stefanssson, V., and Gudlaugsson, S. (2000). Ergebnisse von Bohrloch-Spannungsmessungen in der Südisländischen Seismizitätszone. *Mitteilungen Deutsche Geophysikalische Gesellschaft*, 3:49–50.

Rudnicki, J. (1986). Fluid mass sources and point forces in linear elastic diffusive solids. *Mechanics of Materials*, 5(1986):383–393.

Rutqvist, J. (2011). Status of the tough-flac simulator and recent applications related to coupled fluid flow and crustal deformations. *Computers & Geosciences*, 37(6):739–750.

Rutqvist, J., Dobson, P. F., Garcia, J., Hartline, C., Jeanne, P., Oldenburg, C. M., Vasco, D. W., and Walters, M. (2013). The Northwest Geysers EGS Demonstration Project, California: Pre-stimulation Modeling and Interpretation of the Stimulation. *Mathematical Geosciences*, 47(1):3–29.

Rutqvist, J., Freifeld, B., Min, K.-B., Elsworth, D., and Tsang, Y. (2008). Analysis of thermally induced changes in fractured rock permeability during 8 years of heating and cooling at the Yucca Mountain Drift Scale Test. *International Journal of Rock Mechanics and Mining Sciences*, 45(8):1373–1389.

Rutqvist, J. and Oldenburg, C. (2008). Analysis of injection-induced micro-earthquakes in a geothermal steam reservoir, The Geysers geothermal field, California. *Lawrence Berkeley National Laboratory*.

Sachsenhofer, R., Gratzer, R., Tschelaut, W., and Bechtel, A. (2006). Characterisation of non-producible oil in Eocene reservoir sandstones (Bad Hall Nord field, Alpine foreland basin, Austria). *Marine and Petroleum Geology*, 23(1):1–15.

Sæmundsson, K. (1974). Evolution of the axial rifting zone in northern Iceland and the Tjörnes fracture zone. *Geological Society of America Bulletin*, 85(4):495–504.

Sæmundsson, K. (1978). Fissure swarms and central volcanoes of the neovolcanic zones of Iceland. *Geol. J. Spec*, 10:415–432.

Sæmundsson, K. (1979). Outline of the geology of Iceland. *Jökull*, 29:7–28.

Sæmundsson, K. (1986). Subaerial volcanism in the western North Atlantic. *The Geology of North America*, 1000:69–86.

Sánchez, J. J., Wyss, M., and McNutt, S. R. (2004). Temporal-spatial variations of stress at Redoubt volcano, Alaska, inferred from inversion of fault plane solutions. *Journal of Volcanology and Geothermal Research*, 130(1-2):1–30.

Santarelli, F., Tronvoll, J., Svennekjaier, M., Skeie, H., Henriksen, R., and Bratli, R. (1998). Reservoir stress path: the depletion and the rebound. In *SPE/ISRM Rock Mechanics in Petroleum Engineering*. Society of Petroleum Engineers.

Sbar, M. L. and Sykes, L. R. (1973). Contemporary compressive stress and seismicity in eastern North America: an example of intra-plate tectonics. *Geological Society of America Bulletin*, 84(6):1861–1882.

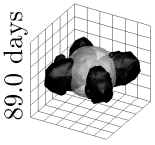

Schäfer, K. and Keil, S. (1979). In situ Gesteinsspannungsermittlungen in Island. *Messtechnische Briefe*, 15(2):35–46.

Scheidegger, A. (1962). Stresses in the earth's crust as determined from hydraulic fracturing data. *Geologie und Bauwesen*, 27(2):1.

Schmid, S. M., Bernoulli, D., Fügenschuh, B., Matenco, L., Schefer, S., Schuster, R., Tischler, M., and Ustaszewski, K. (2008). The Alpine-Carpathian-Dinaridic orogenic system: correlation and evolution of tectonic units. *Swiss Journal of Geosciences*, 101(1):139–183.

Schmitt, D. R., Currie, C. A., and Zhang, L. (2012). Crustal stress determination from boreholes and rock cores: Fundamental principles. *Tectonophysics*, 580:1–26.

Schoenball, M., Dorbath, L., Gaucher, E., Wellmann, J. F., and Kohl, T. (2014). Change of stress regime during geothermal reservoir stimulation. *Geophysical Research Letters*, 41(4):1163–1170.

Schoenball, M., Müller, T. M., Müller, B. I. R., and Heidbach, O. (2010). Fluid-induced microseismicity in pre-stressed rock masses. *Geophysical Journal International*, 180(2):813–819.

Scholz, C. H. (2002). *The mechanics of earthquakes and faulting*. Cambridge University Press.

Schulz, R., Agemar, T., Alten, J., and Kühne, K. (2007). Aufbau eines geothermischen Informationssystems für Deutschland. *Erdöl Erdgas Kohle*, 123(2):76–81.

Sedlacek, R. (2009). Untertage-Gasspeicherung in Deutschland - Underground Gas Storage in Germany. *Erdöl Erdgas Kohle*, 125(11):412–426.

Segall, P. and Fitzgerald, S. D. (1998). A note on induced stress changes in hydrocarbon and geothermal reservoirs. *Tectonophysics*, 289(1-3):117–128.

Seithel, R., Steiner, U., Müller, B., Hecht, C., and Kohl, T. (2015). Local stress anomaly in the Bavarian Molasse Basin. *Geothermal Energy*, 3(1):4.

Sibson, R. H. (1996). Structural permeability of fluid-driven fault-fracture meshes. *Journal of Structural Geology*, 18(8):1031–1042.

Sigmundsson, F., Einarsson, P., Halldorson, P., Jakobsdottir, S., Vogfjörd, K., Sigbjörnsson, R., and Snaebjörnsson, J. T. (2005). Earthquakes and faults in the Kárahnjúkar area. Technical Report March, Jardvisindastofnun Haskolans.

Sigmundsson, F., Hooper, A., Hreinsdóttir, S., Vogfjörd, K. S., Ófeigsson, B. G., Heimisson, E. R., Dumont, S., Parks, M., Spaans, K., Gudmundsson, G. B., Drouin, V., Árnadóttir, T., Jónsdóttir, K., Gudmundsson, M. T., Högnadóttir, T., Fridriksdóttir, H. M., Hensch, M., Einarsson, P., Magnússon, E., Samsonov, S., Brandsdóttir, B., White, R. S., Ágústsdóttir, T., Greenfield, T., Green, R. G., Hjartardóttir, Á. R., Pedersen, R., Bennett, R. A., Geirsson, H., La Femina, P. C., Björnsson, H., Pálsson, F., Sturkell, E., Bean, C. J., Möllhoff, M., Braiden, A. K., and Eibl, E. P. S. (2015). Segmented lateral dyke growth in a rifting event at Bardarbunga volcanic system, Iceland. *Nature*, 517(7533):191–5.

Sigurdsson, H. (1970). Structural origin and plate tectonics of the Snaefellsnes volcanic zone, Western Iceland. *Earth and Planetary Science Letters*, 10(1):129–135.

Sigurdsson, H. and Sparks, R. S. J. (1978). Rifting episode in North Iceland in 1874 - 1875 and the eruptions of Askja and Sveinagja. *Bulletin Volcanologique*, 41(3):149–167.

Simpson, R. W. (1997). Quantifying Anderson's fault types. *Journal of Geophysical Research: Solid Earth (1978–2012)*, 102(B8):17909–17919.

Sinton, J., Grönvold, K., and Sæmundsson, K. (2005). Postglacial eruptive history of the Western Volcanic Zone, Iceland. *Geochemistry, Geophysics, Geosystems*, 6(12):Q12009.

Sjöberg, J., Christiansson, R., and Hudson, J. (2003). ISRM suggested methods for rock stress estimation - Part 2: overcoring methods. *International Journal of Rock Mechanics and Mining Sciences*, 40(7):999–1010.

Snee, J.-E. L. and Zoback, M. D. (2016). State of stress in Texas: Implications for induced seismicity. *Geophysical Research Letters*, 43(19):10,208–10,214.

Sobolev, S. V. and Babeyko, A. Y. (2005). What drives orogeny in the Andes? *Geology*, 33(8):617–620.

Sonder, L. (1990). Effects of density contrasts on the orientation of stresses in the lithosphere: Relation to principal stress directions in the Transverse Ranges, California. *Tectonics*, 9(4):761–771.

Soosalu, H. and Einarsson, P. (1997). Seismicity around the Hekla and Torfajökull volcanoes, Iceland, during a volcanically quiet period, 1991-1995. *Bulletin of Volcanology*, 59(1):36–48.

Sperner, B., Müller, B., Heidbach, O., Delvaux, D., Reinecker, J., and Fuchs, K. (2003). Tectonic stress in the Earth's crust: advances in the World Stress Map project. *Geological Society, London, Special Publications*, 212(1):101–116.

Stadtwerke München GmbH (2012). SWM Vision: Fernwärmeversorgung bis 2040 zu 100 % aus erneuerbaren Energien. `http://www.geothermie.de/fileadmin/useruploads/aktuelles/Aktuelles/Dateien_zu_News/Pressemitteilung_20vom_2012.03.2012.pdf`. Accessed: 27.01.2016.

Stadtwerke München GmbH (2016). Ausbauoffensive Erneuerbare Energien: Ökostrom & Ökowärme. `https://www.swm.de/dam/swm/pressemitteilungen/2016/11/allgemein20161122-swm-fernwareme-version-der-richtige-weg.pdf`. Accessed: 02.03.2017.

Stefánsson, R. (1966). Methods of focal mechanism studies with application to two Atlantic earthquakes. *Tectonophysics*, 3(3):209–243.

Stefánsson, R., Gudmundsson, G. B., and Halldórsson, P. (2000). The two large earthquakes in the South Iceland Seismic Zone on June 17 and 21, 2000. Technical Report July, Icelandic Meterological Organisation, Reykjavík.

Stefánsson, R., Gudmundsson, G. B., and Halldorsson, P. (2008). Tjörnes fracture zone. New and old seismic evidences for the link between the North Iceland rift zone and the Mid-Atlantic ridge. *Tectonophysics*, 447(1):117–126.

Stephens, G. and Voight, B. (1982). Hydraulic fracturing theory for conditions of thermal stress. *International Journal of Rock Mechanics and Mining Sciences & Geomechanics Abstracts*, 19(6):279–284.

Stephenson, R., Egholm, D. L., Nielsen, S. B., and Stovba, S. M. (2009). Role of thermal refraction in localizing intraplate deformation in southeastern Ukraine. *Nature Geoscience*, 2(4):290–293.

Sulem, J. (2007). Stress orientation evaluated from strain localisation analysis in Aigion fault. *Tectonophysics*, 442(1-4):3–13.

Sykes, L. and Sbar, M. (1974). Focal mechanism solutions of intraplate earthquakes and stresses in the lithosphere. In Kristjansson, L., editor, *Geodynamics of Iceland and the North Atlantic Area*, pages 207–224. D. Reidel Publishing Company, Dordrecht-Holland.

Sykes, L. R. (1967). Mechanism of earthquakes and nature of faulting on the mid-oceanic ridges. *Journal of Geophysical Research*, 72(8):2131–2153.

Teatini, P., Castelletto, N., Ferronato, M., Gambolati, G., Janna, C., Cairo, E., Marzorati, D., Colombo, D., Ferretti, A., Bagliani, A., and Bottazzi, F. (2011). Geomechanical response to seasonal gas storage in depleted reservoirs: A case study in the Po River basin, Italy. *Journal of Geophysical Research*, 116(F2):F02002.

Terzaghi, K. (1943). *Theoretical Soil Mechanics*. Wiley-Blackwell.

Teufel, L. (1983). Determination of in-situ stress from anelastic strain recovery measurements of oriented core. In *SPE/DOE Low Permeability Gas Reservoirs Symposium*. Society of Petroleum Engineers.

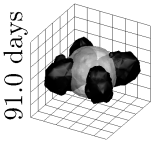

Thordarson, T. and Larsen, G. (2007). Volcanism in Iceland in historical time: Volcano types, eruption styles and eruptive history. *Journal of Geodynamics*, 43(1):118–152.

Tibaldi, A., Bonali, F. L., Pasquaré, F. A., Rust, D., Cavallo, A., and D'Urso, A. (2013). Structure of regional dykes and local cone sheets in the Midhyrna-Lysuskard area, Snaefellsnes Peninsula (NW Iceland). *Bulletin of Volcanology*, 75(11):764.

Tingay, M., Heidbach, O., Davies, R., and Swarbrick, R. (2008). Triggering of the Lusi mud eruption: Earthquake versus drilling initiation. *Geology*, 36(8):639–642.

Tingay, M., Morley, C., King, R., Hillis, R., Coblentz, D., and Hall, R. (2010). Present-day stress field of Southeast Asia. *Tectonophysics*, 482(1):92–104.

Tingay, M., Müller, B., Reinecker, J., Heidbach, O., Wenzel, F., and Fleckenstein, P. (2005). Understanding tectonic stress in the oil patch: The World Stress Map Project. *The Leading Edge*, 24(12):1276–1282.

Tingay, M., Rudolph, M. L., Manga, M., Davies, R., and Wang, C.-Y. (2015). Initiation of the Lusi mudflow disaster. *Nature Geoscience*, 8(7):493–494.

Tischner, T., Evers, H., Hauswirth, H., Jatho, R., Kosinowski, M., and Sulzbacher, H. (2010). New Concepts for Extracting Geothermal Energy from One Well: The GeneSys-Project. In *Proceedings World Geothermal Congress 2010*, pages 1–5, Bali, Indonesia. International Geothermal Association.

Townend, J. and Zoback, M. (2004). Regional tectonic stress near the San Andreas fault in central and southern California. *Geophysical Research Letters*, 31(15).

Townend, J. and Zoback, M. D. (2000). How faulting keeps the crust strong. *Geology*, 28(5):399–402.

Van Wees, J., Buijze, L., Van Thienen-Visser, K., Nepveu, M., Wassing, B., Orlic, B., and Fokker, P. (2014). Geomechanics response and induced seismicity during gas field depletion in the Netherlands. *Geothermics*, 52:206–219.

Van Wees, J., Orlic, B., Van Eijs, R., Zijl, W., Jongerius, P., Schreppers, G., Hendriks, M., and Cornu, T. (2003). Integrated 3D geomechanical modelling for deep subsurface deformation: a case study of tectonic and human-induced deformation in the eastern Netherlands. *Geological Society, London, Special Publications*, 212(1):313–328.

Villemin, T., Bergerat, F., Angelier, J., and Lacasse, C. (1994). Brittle deformation and fracture patterns on oceanic rift shoulders: the Esja peninsula, SW Iceland. *Journal of Structural Geology*, 16(12):1641–1654.

Walsh, J. B. (1965). The effect of cracks on the compressibility of rock. *Journal of Geophysical Research*, 70(2):381–389.

Ward, P. (1971). New interpretation of the geology of Iceland. *Geological Society of America Bulletin*, 82(11):2991–3012.

Warner, T. T. and Hsu, H.-M. (2000). Nested-model simulation of moist convection: The impact of coarse-grid parameterized convection on fine-grid resolved convection. *Monthly weather review*, 128(7):2211–2231.

Warpinski, N. (1989). Determining the minimum in situ stress from hydraulic fracturing through perforations. *International Journal of Rock Mechanics and Mining Sciences & Geomechanics Abstracts*, 26(6):523–531.

Wassing, B., Van Wees, J., and Fokker, P. (2014). Coupled continuum modeling of fracture reactivation and induced seismicity during enhanced geothermal operations. *Geothermics*, 52:153–164.

Watzel, R. (2013). www.geopotenziale.eu. `http://www.geopotenziale.eu`. Accessed: 15.02.2017.

Weber, J., Ganz, B., Schellschmidt, R., Sanner, B., and Schulz, R. (2015). Geothermal Energy Use in Germany. In *Proceedings World Geothermal Congress*, pages 1–15, Melbourne, Australia. International Geothermal Association.

Weides, S., Moeck, I., Majorowicz, J., Palombi, D., Grobe, M., and Mareschal, J.-C. (2013). Geothermal exploration of Paleozoic formations in Central Alberta. *Canadian Journal of Earth Sciences*, 50(5):519–534.

Wellmann, J. F. (2013). Information Theory for Correlation Analysis and Estimation of Uncertainty Reduction in Maps and Models. *Entropy*, 15(4):1464–1485.

Wellmann, J. F. and Regenauer-Lieb, K. (2012). Uncertainties have a meaning: Information entropy as a quality measure for 3-D geological models. *Tectonophysics*, 526:207–216.

Wessel, P., Smith, W. H. F., Scharroo, R., Luis, J., and Wobbe, F. (2013). Generic Mapping Tools: Improved Version Released. *Eos, Transactions American Geophysical Union*, 94(45):409–410.

Westerhaus, M., Altmann, J., and Heidbach, O. (2008). Using topographic signatures to classify internally and externally driven tilt anomalies at Merapi Volcano, Java, Indonesia. *Geophysical Research Letters*, 35(5).

White, R. S., Drew, J., Martens, H. R., Key, J., Soosalu, H., and Jakobsdóttir, S. S. (2011). Dynamics of dyke intrusion in the mid-crust of Iceland. *Earth and Planetary Science Letters*, 304(3):300–312.

Wiens, D. A. and Stein, S. (1984). Intraplate seismicity and stresses in young oceanic lithosphere. *Journal of Geophysical Research*, 89(B13):11442–11464.

Wiprut, D., Zoback, M., Hanssen, T., and Peška, P. (1997). Constraining the full stress tensor from observations of drilling-induced tensile fractures and leak-off tests: application to borehole stability and sand production on the Norwegian margin. *International Journal of Rock Mechanics and Mining Sciences*, 34(365):3–4.

Wolfe, C. J., Bjarnason, I. T., VanDecar, J. C., and Solomon, S. C. (1997). Seismic structure of the Iceland mantle plume. *Nature*, 385(6613):245–247.

Wolfgramm, M., Bartels, J., Hoffmann, F., Kittl, G., Lenz, G., Seibt, P., Schulz, R., Thomas, R., and Unger, H. (2007). Unterhaching geothermal well doublet: structural and hydrodynamic reservoir characteristic; Bavaria (Germany). In *Proceedings European Geothermal Congress 2007*, pages 1–6, Unterhaching, Germany.

Yoon, J. S., Zang, A., and Stephansson, O. (2014a). Numerical investigation on optimized stimulation of intact and naturally fractured deep geothermal reservoirs using hydro-mechanical coupled discrete particles joints model. *Geothermics*, 52:165–184.

Yoon, J.-S., Zang, A., Zimmermann, G., and Stephansson, O. (2014b). Use of discrete fracture network in discrete element modeling in applications to simulation of hydraulic stimulation of geothermal reservoir and thermo-quake induced seismicity in a nuclear waste repository. In *International Discrete Fracture Network Engineering Conference (DFNE)*.

Yoon, J. S., Zimmermann, G., and Zang, A. (2015a). Discrete element modeling of cyclic rate fluid injection at multiple locations in naturally fractured reservoirs. *International Journal of Rock Mechanics and Mining Sciences*, 74:15–23.

Yoon, J. S., Zimmermann, G., and Zang, A. (2015b). Numerical Investigation on Stress Shadowing in Fluid Injection-Induced Fracture Propagation in Naturally Fractured Geothermal Reservoirs. *Rock Mechanics and Rock Engineering*, 48(4):1439–1454.

Zang, A., Oye, V., Jousset, P., Deichmann, N., Gritto, R., McGarr, A., Majer, E., and Bruhn, D. (2014). Analysis of induced seismicity in geothermal reservoirs - An overview. *Geothermics*, 52:6–21.

Zang, A. and Stephansson, O. (2010). *Stress Field of the Earth's Crust*. Springer Netherlands, Dordrecht.

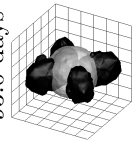

Zang, A., Stephansson, O., Heidbach, O., and Janouschkowetz, S. (2012). World Stress Map Database as a Resource for Rock Mechanics and Rock Engineering. *Geotechnical and Geological Engineering*, 30(3):625–646.

Zang, A., Stephansson, O., Stenberg, L., Plenkers, K., Specht, S., Milkereit, C., Schill, E., Kwiatek, G., Dresen, G., Zimmermann, G., Dahm, T., and Weber, M. (2017). Hydraulic fracture monitoring in hard rock at 410 m depth with an advanced fluid-injection protocol and extensive sensor array. *Geophysical Journal International*, 208(2):790–813.

Zang, A., Yoon, J. S., Stephansson, O., and Heidbach, O. (2013). Fatigue hydraulic fracturing by cyclic reservoir treatment enhances permeability and reduces induced seismicity. *Geophysical Journal International*, 195(2):1282–1287.

Ziegler, M., Rajabi, M., Heidbach, O., Hersir, G. P., Ágústsson, K., Árnadóttir, S., and Zang, A. (2016a). The Stress Pattern of Iceland. *Tectonophysics*, 674:101–113.

Ziegler, M., Rajabi, M., Hersir, G., Ágústsson, K., Árnadóttir, S., Zang, A., Bruhn, D., and Heidbach, O. (2016b). Stress map Iceland 2016. `http://doi.org/10.5880/WSM.Iceland2016`.

Ziegler, M., Reiter, K., Heidbach, O., Zang, A., Kwiatek, G., Stromeyer, D., Dahm, T., Dresen, G., and Hofmann, G. (2015). Mining-Induced Stress Transfer and Its Relation to a M_w 1.9 Seismic Event in an Ultra-deep South African Gold Mine. *Pure and Applied Geophysics*, 172(10):2557–2570.

Ziegler, M. O. and Heidbach, O. (2017a). Manual of the Matlab Script Stress2Grid. WSM Technical Report 17-02, Potsdam: GFZ German Research Centre for Geosciences.

Ziegler, M. O. and Heidbach, O. (2017b). Matlab script stress2grid. `http://doi.org/10.5880/wsm.2017.002`.

Ziegler, M. O., Heidbach, O., Reinecker, J., Przybycin, A. M., and Scheck-Wenderoth, M. (2016c). A multi-stage 3-D stress field modelling approach exemplified in the Bavarian Molasse Basin. *Solid Earth*, 7(5):1365–1382.

Ziegler, M. O., Heidbach, O., Reinecker, J., Przybycin, A. M., and Scheck-Wenderoth, M. (2016d). Corrigendum to "A multi-stage 3-D stress field modelling approach exemplified in the Bavarian Molasse Basin" published in Solid Earth, 7, 1365–1382, 2016. *Solid Earth*, 7(5):1365–1382.

Ziegler, M. O., Heidbach, O., Zang, A., Martínez-Garzón, P., and Bohnhoff, M. (2017). Estimation of the differential stress from the stress rotation angle in low permeable rock. *Geophysical Research Letters*, pages 6761–6770.

Zienkiewicz, O. C. (1987). *Methode der finiten Elemente*. VEB Fachbuchverlag Leipzig, Leipzig, 2nd edition.

Zimmerman, R. (2000). Coupling in poroelasticity and thermoelasticity. *International Journal of Rock Mechanics and Mining Sciences*, 37(1):79–87.

Zimmermann, G., Moeck, I., and Blöcher, G. (2010). Cyclic waterfrac stimulation to develop an enhanced geothermal system (EGS) – conceptual design and experimental results. *Geothermics*, 39(1):59–69.

Zoback, M. (2010). *Reservoir Geomechanics*. Cambridge University Press, Cambridge.

Zoback, M., Barton, C., Brudy, M., Castillo, D., Finkbeiner, T., Grollimund, B., Moos, D., Peška, P., Ward, C., and Wiprut, D. (2003). Determination of stress orientation and magnitude in deep wells. *International Journal of Rock Mechanics and Mining Sciences*, 40(7-8):1049–1076.

Zoback, M. and Zoback, M. (1991). Tectonic stress field of North America and relative plate motions. In Slemmons, D. and Engdahl, E., editors, *Neotectonics of North America*, pages 339–366. Geological Society of America, Boulder, Colorado.

Zoback, M. D., Moos, D., Mastin, L., and Anderson, R. N. (1985). Well bore breakouts and in situ stress. *Journal of Geophysical Research: Solid Earth*, 90(B7):5523–5530.

Zoback, M. L. (1992). First- and second-order patterns of stress in the lithosphere: The World Stress Map Project. *Journal of Geophysical Research*, 97(B8):11703–11728.

Zoback, M. L., Zoback, M. D., Adams, J., Assumpção, M., Bell, S., Bergman, E. A., Blümling, P., Brereton, N. R., Denham, D., Ding, J., Fuchs, K., Gay, N., Gregersen, S., Gupta, H. K., Gvishiani, A., Jacob, K., Klein, R., Knoll, P., Magee, M., Mercier, J. L., Müller, B. C., Paquin, C., Rajendran, K., Stephansson, O., Suarez, G., Suter, M., Udias, A., Xu, Z. H., and Zhizhin, M. (1989). Global patterns of tectonic stress. *Nature*, 341(6240):291–298.

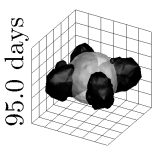

List of Figures

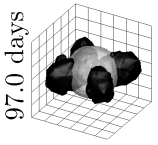

List of Tables

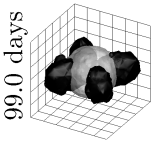

Supplementary data

The supplementary data can be accessed in the online version of this thesis with a double-click on the filename. In the printed version the files can be accessed on the attached compact disc.

Supplement to Chapter 3

The Iceland stress database compiled as a part of this thesis is supplemented in the manuscript (Chapter 3 and Ziegler et al. 2016a). The supplemented spreadsheet file is in the WSM file format (Heidbach, 2016).

Iceland_Stress_Database.xlsx

Supplement to Chapter 6

A video that corresponds to the flip-book on the bottom right side of uneven pages in the printed version of this thesis. Displayed is the volume of a stress tensor rotation of at least $\pm 1\,^{\circ}$ (black) and a pore pressure increase by at least 10 MPa (grey). The grid spacing is 250 m.

Stress_Rotation.mp4

Acknowledgement

First of all I have to thank my supervisors Arno Zang and Oliver Heidbach who gave me the opportunity to work as a PhD student on these fascinating topics. I want to express my deep gratitude to my technical supervisor Oliver Heidbach who provided guidance and support throughout my time as a PhD student. I want to thank my supervisor Arno Zang for his thoughtful comments, his support, and his questions that always helped in looking at my work from various points of view.

This work would not have been possible without the financial support from the European Union (European Community's Seventh Framework Programme under grant agreement No. 608553 – Project IMAGE). With respect to this I have to thank David Bruhn for his support and commitment. Furthermore, I have to thank my colleagues from the IMAGE project for the familiar atmosphere and the great time we had at the meetings.

I want to thank Karsten Reiter, Dietrich Stromeyer, Konrad Schellbach, Sebastian Specht, Carlos Peña, Fabrice Cotton, and all the other (former) colleagues from section 2.6 for the enjoyable atmosphere. Furthermore, I want to thank Mojtaba Rajabi, Jessica Freymark, Judith Sippel, Anna Przybycin, John Reinecker, Patricia Martínez-Garzón, and Marco Bohnhoff who contributed to and helped with one or another part of my thesis.

I want to thank my parents for their support, advice, and existence in general. Finally I want to thank Karo and Leander. Karo for her endless love, support, and stubbornness. Leander for his smiles when coming home and for dragging me away from work on my hair (even though it was usually at night, I wasn't working, and he was supposed to be asleep).

Declaration (Selbstständigkeitserklärung)

Hiermit versichere ich, dass ich diese Arbeit selbständig verfasst und keine anderen als die angegebenen Quellen, Internet-Quellen und Hilfsmittel benutzt habe. Die Stellen der Arbeit, die anderen Werken dem Wortlaut oder dem Sinn nach entnommen sind, habe ich in jedem einzelnen Fall unter Angabe der Quelle als Entlehnung kenntlich gemacht. Diese Versicherung bezieht sich auch auf bildliche und tabellarische Darstellungen.

Potsdam, den 11. Mai 2017: _____

Curriculum Vitae

Pages XIII–XV (Curriculum Vitae) contain private data. They are not included in the online publication.

Pages XIII–XV (Curriculum Vitae) contain private data. They are not included in the online publication.

Pages XIII–XV (Curriculum Vitae) contain private data. They are not included in the online publication.